Multi-Parton Interactions at the LHC

(Article begins on next page)

22 September 2024

Multi-Parton Interactions at the LHC

P. Bartalini[1], E. L. Berger[2], B. Blok[3], G. Calucci[4], R. Corke[5], M. Diehl[6], Yu. Dokshitzer[7], L. Fanò[8], L. Frankfurt[9], J. R. Gaunt[10], S. Gieseke[11], G. Gustafson[5], D. Kar[12], C.-H. Kom[10], A. Kulesza[13], E. Maina[14], Z. Nagy[6], Ch. Röhr[11], A. Siódmok[11], M. Schmelling[15], W. J. Stirling[10], M. Strikman[16], and D. Treleani[4]

edited by A. Kulesza and Z. Nagy

[1] National Taiwan University, Taipei,Taiwan
[2] High Energy Physics Division, Argonne National Laboratory, Argonne, IL 60439, USA
[3] Department of Physics, Technion—Israel Institute of Technology, 32000 Haifa, Israel
[4] Dipartimento di Fisica dell'Università di Trieste and INFN, Sezione di Trieste, Strada Costiera 11, Miramare-Grignano, I-34151 Trieste, Italy
[5] Theoretical High Energy Physics, Department of Astronomy and Theoretical Physics,Lund University, Sölvegatan 14A, S-223 62 Lund, Sweden
[6] Deutsches Elektronen-Synchroton DESY, 22603 Hamburg, Germany
[7] Laboratory of Theoretical High Energy Physics (LPTHE), University Paris 6, Paris, France; on leave of absence: PNPI, St. Petersburg, Russia
[8] INFN and Università degli Studi di Perugia, Italy
[9] School of Physics and Astronomy, Raymond and Beverly Sackler Faculty of Exact Sciences, Tel Aviv University, 69978 Tel Aviv, Israel
[10] Cavendish Laboratory, J.J. Thomson Avenue, University of Cambridge, Cambridge CB3 0HE, UK
[11] Karlsruhe Institute of Technology, 76128 Karlsruhe, Germany
[12] IKTP, TU Dresden, Germany
[13] Institute for Theoretical Particle Physics and Cosmology, RWTH Aachen University D-52056 Aachen, Germany
[14] INFN, Sezione di Torino, and Dipartimento di Fisica Teorica, Università di Torino, Italy
[15] MPI for Nuclear Physics, Saupfercheckweg 1, D-69117 Heidelberg, Germany
[16] Physics Department, Penn State University, University Park, PA, USA

Abstract. We review the recent progress in the theoretical description and experimental observation of multiple parton interactions. Subjects covered include experimental measurements of minimum bias interactions and of the underlying event, models of soft physics implemented in Monte Carlo generators, developments in the theoretical description of multiple parton interactions and phenomenological studies of double parton scattering. This article stems from contributions presented at the Helmholtz Alliance workshop on "Multi-Parton Interactions at the LHC", DESY Hamburg, 13-15 September 2010.

1 Introduction

The Large Hadron Collider (LHC) began operation in 2008, opening a new chapter in particle physics. The basis for understanding hadronic collisions at high energy is provided by the QCD improved parton model. In this framework each hadron is described as a collection of essentially free elementary constituents. The interactions between constituents belonging to different colliding hadrons are the seeds of the complicated process which eventually leads to the particles observed in the detector. Due to the composite nature of hadrons, it is possible to have multiple parton hard-scatterings, i.e. events in which two or more distinct hard parton interactions occur simultaneously in a single hadron-hadron collision. At fixed final state invariant masses, such cross sections tend to increase with collision energy because partons with successively lower momentum fraction x, hence rapidly increasing fluxes, are being probed. As a result, events with relatively low invariant masses could receive enhanced contributions from multiple hard scatterings. This class of events is known as Multiple Parton Interactions (MPI), while those in which only a single pair of partons produce a hard scattering are referred as Single Parton Scattering (SPS).

The MPI can manifest themselves in various ways in high energy hadronic collisions. It is natural to expect a relation between the multiplicity of simultaneous partonic scatterings and their typical scale. In particular, large hadronic activity is observed in the soft regime, characterized by small transverse momenta (p_T) of the produced particles. For relatively large p_T values, the observation of MPI will mostly focus on two simultaneous scatterings, i.e. on Double Parton Scattering (DPS). Unfortunately, also depending on the scale of the partonic subprocess our ability to describe MPI in the pQCD framework is challenging. Whereas it is most legitimate to use pQCD methods for the description of MPI at large p_T, it is necessary to supplement the pQCD picture in the soft regime with models of soft physics .

The evidence for MPI comes from high p_T events observed in hadron collisions at the ISR at CERN [1] and later at the Fermilab Tevatron collider[2,3,4]. At lower p_T, underlying event (UE) observables have been measured in $p\bar{p}$ collisions in dijet and Drell-Yan events at CDF in Run I [5] and Run II [6] at center-of-mass energies of $\sqrt{s} = 1.8$ TeV and 1.96 TeV respectively, and in pp collisions at $\sqrt{s} = 900$ GeV in a detector-specific study by CMS [7].

At small transverse momentum MPI have been shown to be necessary for the successful description of the UE in Monte Carlo generators such as Pythia [8,9,10] or Herwig [11,12]. Additionally, MPI are currently invoked to account for observations at hadron colliders that would not be explained otherwise: the cross sections of multi-jet production, the survival probability of large rapidity gaps in hard diffraction, etc. [13]. The wide range of phenomena in which MPI are involved highlights the urgency of a more thorough understanding of these reactions both experimentally and from a theoretical point of view.

The last few years have proven to be a renaissance for research work on MPI. The renewed interest in the field follows from the expected abundance of MPI phenomena at the LHC and thus their importance for the full picture of hadronic collisions, as well as opportunities provided by the LHC to measure multiple parton hard-scatterings. In particular, given the inability to describe the very soft regime with perturbative methods, the relevance of experimental measurements by the LHC collaborations of observables containing information on MPI, sensitive to the underlying event or minimum bias events, cannot be overstated.

Ultimately, one would strive for a uniform and coherent description of MPI in both soft and hard regimes. At present we are still far away from this goal, as so far essentially separate research efforts focus on specific aspects of MPI. In the present article we attempt to bridge this gap by reviewing the current status of the field. The article is a result of the Helmholtz Alliance workshop "Multi-Parton Interactions at the LHC" which took place at DESY in September 2010. Its main goal was to bring the experimental and theoretical MPI community together, providing a forum for a discussion and scientific exchange.

This article is organized as follows. We begin with a review of the experimental measurements (available at the time of the workshop) in Chapter 2. Progress in the implementation of MPI in the Monte Carlo event generators is described in Chapter 3. We then focus on the theoretical aspects of MPI in Chapter 4 and discuss the phenomenology of selected DPS processes at the LHC in Chapter 5.

2 Experimental situation

A complete description of hadronic activity in high energy collisions requires understanding of the UE, as it constitutes the unavoidable background to most observables. From an experimental point of view, the UE gathers all the activity accompanying the actual hard scattering one is interested in measuring. In this sense the UE consists of MPI and the interactions between consituents of beam remnants, left behind after the scattering partons have been pulled out.

Even more inclusive measurements probe the so-called Minimum Bias (MB) events. These are events which are collected with a relatively non-restrictive trigger which accepts large fraction of events, of both the elastic and inelastic nature, inelastic involving the diffractive as well as soft and hard "hard-core" events.

Since it is impossible to uniquely separate the UE from the hard scattering process on an event-by-event basis, the topological structure of the outcome of hadronic collisions is focused on instead. Typically, studies of UE rely
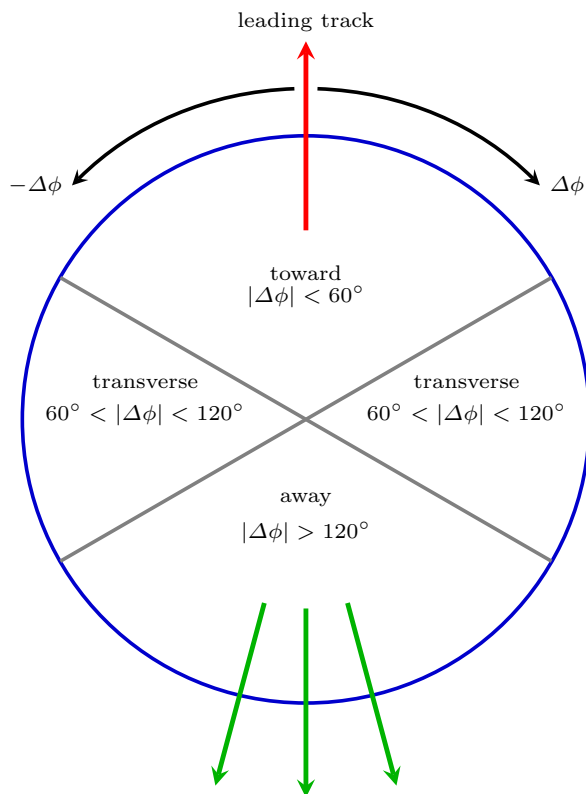
Fig. 1. Definition of regions in the azimuthal angle with respect to the leading track.

on measurements of the properties of charged particle production, while the charged multiplicity and p_T spectrum are basic MB observables. Observing charged particles allows one to investigate the region of very low p_T, crucial for exploring soft and semi-hard physics. At higher values of p_T, it is possible to directly observe hard MPI in the form of double parton scattering (DPS). In this chapter, we review the experimental studies of UE, MB, forward measurements, as well as discuss the prospects for observing hard DPS at the LHC.

2.1 Underlying Event Measurements at ATLAS
Contributing author: D. Kar (on behalf of the ATLAS Collaboration)

This section reports on the measurement of UE observables, performed with the ATLAS detectorat the LHC using proton–proton collisions at center-of-mass energies of 900 GeV and 7 TeV [14].

At the detector level, charged particles are observed as tracks in the inner tracking system. The direction of the track with the largest p_{T} in the event – referred to as the "leading" track – is used to define regions of the η–ϕ plane which have different sensitivities to the UE. The axis given by the leading track is well-defined for all events, and is highly correlated with the axis of the hard scattering in high-p_{T} events. A single track is used as opposed to a jet or the decay products of a massive gauge boson, as it allows significant results to be derived with limited luminosity and avoids the systematic measurement complexities of alignment with more complex objects.

As illustrated in Fig. 1, the azimuthal angular difference between charged tracks and the leading track, $|\Delta\phi| = |\phi - \phi_{\text{leading track}}|$, is used to define the following three azimuthal regions [5]:

– $|\Delta\phi| < 60°$, the "toward region";
– $60° < |\Delta\phi| < 120°$, the "transverse region"; and
– $|\Delta\phi| > 120°$, the "away region".

The transverse regions are most sensitive to the underlying event, since they are generally perpendicular to the axis of hardest scattering.

2.1.1 Analysis Details

All data used in this paper were taken during the LHC running periods with stable beams and defined beam-spot values, between 6th–15th December 2009 for the analysis at $\sqrt{s} = 900$ GeV, and from 30th March to 27th April 2010 for the 7 TeV analysis. Only events with leading track $p_T > 1$ GeV within the inner detector, $|\eta| < 2.5$, were considered, in order to reject events where the leading track selection can potentially introduce large systematic effects, and also to reduce the contribution from diffractive hard scattering processes. All the other tracks were required to have $p_T > 500$ MeV and the same η range.

The 900 GeV and 7 TeV data respectively correspond to integrated luminosities of 7 μb^{-1} and 168 μb^{-1}, respectively, and the effects of pileup was negligible. For the MC models considered here, the contribution of diffractive events to the underlying event observables was less than 1%.

The data were corrected back to charged primary particle spectra satisfying the event-level requirement of at least one primary charged particle within $p_T > 1$ GeV and $|\eta| < 2.5$. A two step correction process was used, where first the event and track efficiency corrections were applied, then an additional bin-by-bin unfolding was performed to account for possible bin migrations and any remaining detector effects.

2.1.2 Results

In this section, corrected distributions of underlying event observables are compared to model predictions tuned to a wide range of measurements. The transverse, toward and away regions each have an area of $\Delta\phi\,\Delta\eta = 10\,\pi/3$ in η–ϕ space, so the density of particles $\langle d^2 N_{ch}/d\eta\, d\phi \rangle$ and transverse momentum sum $\langle d^2 \sum p_T/d\eta\, d\phi \rangle$ are constructed by dividing the mean values by the corresponding area. The leading charged particle is included in the toward region distributions, unless otherwise stated.

The data, corrected back to particle level in the transverse, toward and away regions are compared with predictions by PYTHIA [15] with the ATLAS MC09 [16], DW [17], and Perugia0 [18] tunes, by HERWIG+JIMMY [19,11] with the ATLAS MC09 tune, and by PHOJET [20]. The ratios of the MC predictions to the data are shown at the bottom of these plots. The error bars show the statistical uncertainty while the shaded area shows the combined statistical and systematic uncertainties.

The charged particle multiplicity density, is shown in Fig. 2.

The average number of charged particles in the transverse region increases with leading p_T, until it reaches an approximately constant "plateau". All the pre-LHC MC tunes considered show at least 10–15% lower activity than the data in the transverse region plateau. The PYTHIA DW tune is seen to be the closest model to data for the transverse region. The toward and away regions are dominated by jet-like activity, yielding gradually rising number densities. The 900 GeV and 7 TeV ATLAS data show the same trend. The underlying event activity is seen to increase by a factor of approximately two between the 900 GeV and 7 TeV data. This is roughly consistent with the rate of increase predicted by MC models tuned to Tevatron data.

The charged particle scalar p_T sum, $\sum p_T$ density, is shown in Fig. 3. The summed charged particle p_T in the plateau characterizes the mean contribution of the underlying event to jet energies. Again, we can see that pre-LHC tunes model CDF data better than ATLAS data. The higher number density implies a higher p_T density as well. In the toward and away regions, jet-like rising profiles are observed, in contrast to the plateau in the transverse region. The toward region includes the leading charged particle, and has a higher $\sum p_T$ than the away region as there is higher probability of high-p_T particles being produced in association with the leading p_T charged particle. In the toward region the highest fraction of energy has been allocated to a single charged particle. This implicitly reduces the number of additional charged particles in that region, since there is less remaining energy to be partitioned. As a result the multiplicity of charged particles is slightly lower in the toward region by comparison to the away region for high p_T^{lead}. The increase of the p_T densities in the toward and away regions indicates the extent of the variation in the charged fraction of the total energy in each region.

In Fig. 4, the standard deviation of the charged particle multiplicity and charged particle scalar $\sum p_T$ densities, are shown. The mean and standard deviation of the p_T density in the transverse region characterize a range of additional energy that jets might acquire if the underlying event were uniformly distributed. The confirmation that the magnitude of the standard deviations of the distributions are comparable to the magnitudes of the mean values indicates that a subtraction of the underlying event from jets should be done on an event by event basis, rather than by the subtraction of an invariant average value.

The correlation between the mean p_T of charged particles and the charged particle multiplicity in that region is sensitive to the amount of hard (perturbative QCD) versus soft (non-perturbative QCD) processes contributing to the underlying event.

In Fig. 5, the ATLAS profiles in the transverse and away regions are very similar, showing a monotonic increase of $\langle p_T \rangle$ with N_{ch}. The profile of the toward region is different, as it is essentially determined by the requirement of a track with $p_T > 1$ GeV. For $N_{ch} = 1$, it contains only the leading charged particle and as the N_{ch} is increased by
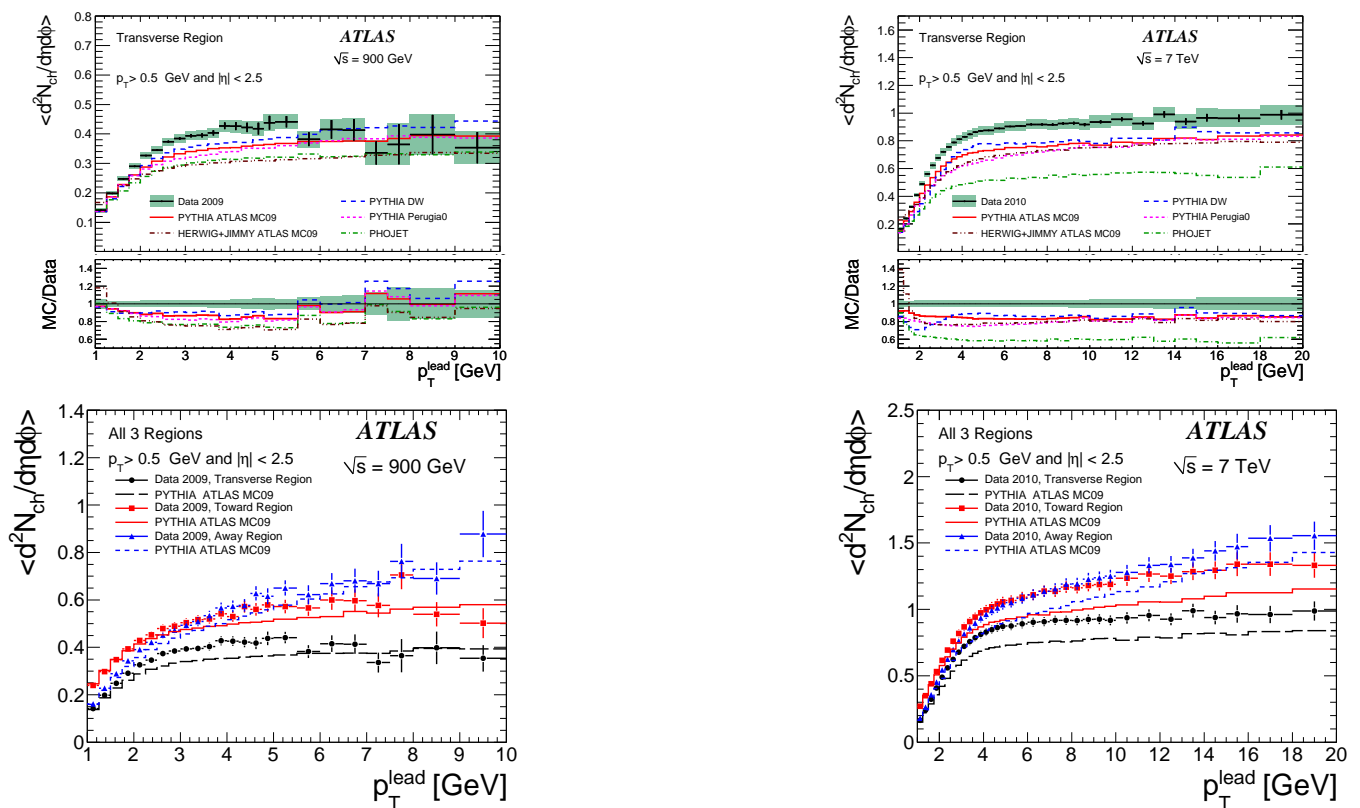
Fig. 2. ATLAS data at $\sqrt{s} = 900$ GeV (left) and 7 TeV (right), showing the density of the charged particles in the transverse region (top row), and in all three regions (bottom row)

inclusion of soft charged particles the average is reduced. However, for $N_{ch} > 5$ jet-like structure begins to form, and the weak rise of the mean p_T is observed. Comparing the 900 GeV and 7 TeV data, it is seen that the mean charged particle p_T vs. N_{ch} profiles are largely independent of the energy scale of the collisions.

The angular distributions with respect to the leading charged particle of the charged particle number and $\sum p_T$ densities at the center-of-mass energy of 7 TeV at ATLAS, are plotted in Fig 6. The leading charged particle taken to be at $\Delta\phi = 0$ has been excluded from the distributions. The data are shown for four different lower cut values in leading charged particle p_T. These distributions are constructed by reflecting $|\Delta\phi|$ about zero, i.e. the region $-\pi \leq \Delta\phi < 0$ is an exact mirror image of the measured $|\Delta\phi|$ region shown in $0 \leq \Delta\phi \leq \pi$.

These distributions show a significant difference in shape between data and MC predictions. With the increase of the leading charged particle p_T, the development of jet-like structure can be observed, and the corresponding sharper rise in transverse regions compared to the MC. MC models essentially predict a stronger correlation than is seen in the data, and this discrepancy in toward region associated particle density was also observed at CDF [21].

A complementary way [22] to look at the angular correlation is by either subtracting the minimum of the distribution (determined by a second-order polynomial fit), or by subtracting the opposite side distribution (defined according to if pseudorapidity has the same or the opposite sign as the leading track) from the same side distribution and normalizing to unity. In Fig. 7, it is seen that the models are better at lower η than at higher.

2.1.3 Summary and Conclusions

One of the goals of these analyses is to provide data that can be used to test and improve MC models for current and future physics studies at the LHC. The underlying event observables presented here are particularly important for constraining the energy evolution of multiple partonic interaction models, since the plateau heights of the underlying event profiles are highly correlated to multiple parton interaction activity. The data at 7 TeV are crucial for MC tuning, since measurements are needed with at least two energies to constrain the energy evolution of MPI activity.

There is no current standard MC tune which adequately describes all the early ATLAS data. However, using diffraction-limited minimum bias distributions and the plateau of the underlying event distributions presented here,
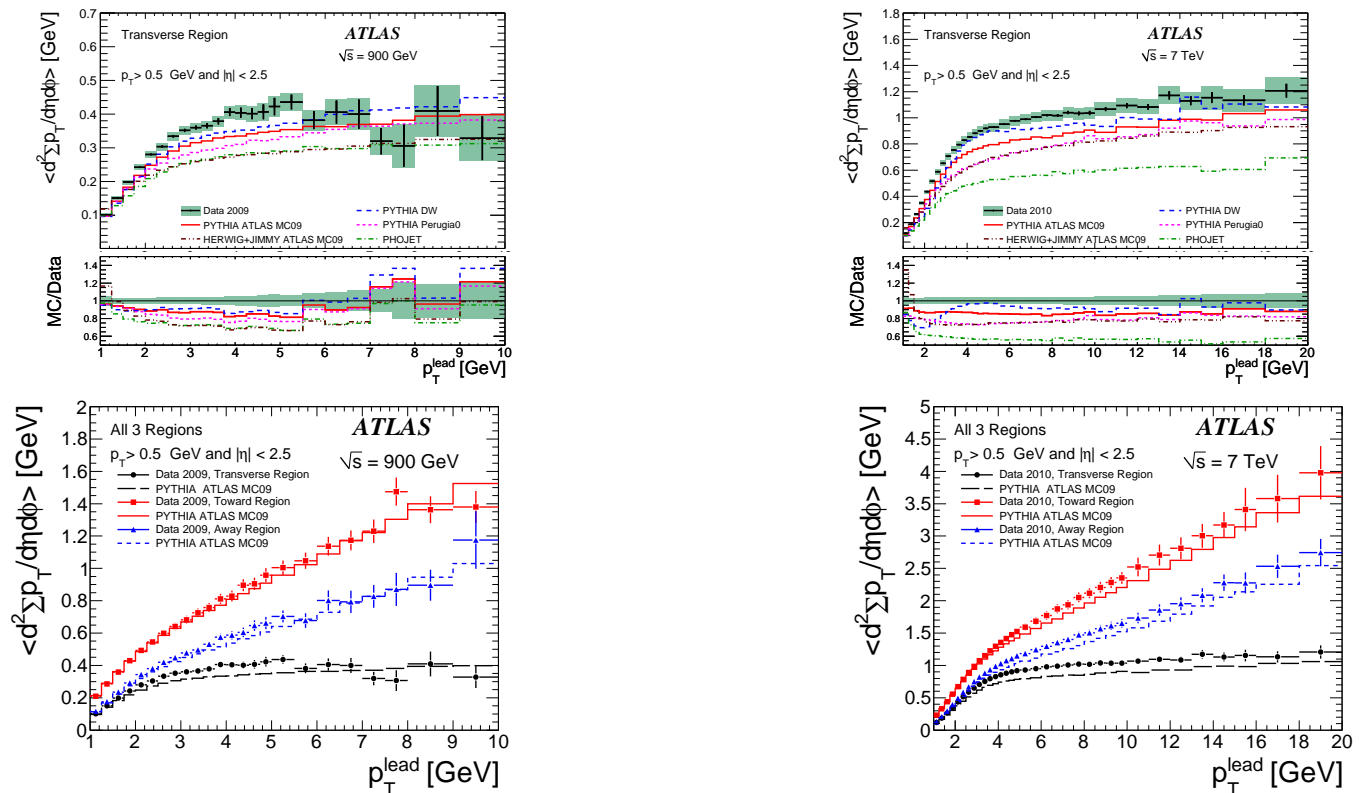
Fig. 3. ATLAS data at $\sqrt{s} = 900$ GeV (left) and 7 TeV (right), showing the scalar $\sum p_{\mathrm{T}}$ density of the charged particles in the transverse region (top row), and in all three regions (bottom row)

ATLAS has developed a new PYTHIA tune AMBT1 (ATLAS Minimum Bias Tune 1) and a new HERWIG+JIMMY tune AUET1 (ATLAS Underlying Event Tune 1) which model the p_{T} and charged multiplicity spectra significantly better than the pre-LHC tunes of those generators [23,24]. It is critical to have sensible underlying event models containing our best physical knowledge and intuition, tuned to all relevant available data.

2.2 Multiple Parton Interactions Studies at CMS
Contributing authors: P. Bartalini and Livio Fanò (on behalf of the CMS Collaboration)

This section summarizes the early Underlying Event and forward measurements of the CMS collaboration using pp collision data up to highest energies of $\sqrt{s} = 7$ TeV. It also reports along the feasibility study for the direct measurement of double parton scattering phenomena focusing on the $3jet + \gamma$ channel.

A detailed description of the CMS detector is available in Ref. [25]. Generator level Monte Carlo (MC) predictions are compared to the data corrected with a bayesian unfolding technique taking into account the detector effects [26].

The predictions for inelastic events are provided here by several tunes of the PYTHIA program, versions 6.420 [27, 15] and 8.135[1] [28,29]. PHOJET [30] is also used in the forward measurements:

The pre-LHC tune D6T [31,13] of PYTHIA 6, which describes the lower energy UA5 and Tevatron data, is a widely used reference that will also be used for most of the presented analyses. The tunes DW [13] and CW [7], which were found to describe best the UE CMS data at 0.9 TeV whereas D6T predictions were too low [7], will also be discussed for the 7 TeV data. The pre-LHC tune Perugia-0 [32] and the new tune, Z1 [33], adopt p_T ordering of parton showers and the new PYTHIA MPI model [34]. It includes the results of the Professor tunes [35] considering LEP fragmentation and the color reconnection parameters of the AMBT1 tune [36], while with the first CMS UE results [7,37] have been used to tune the parameters governing the value and the $\sqrt{s}$ dependence of the cut-off transverse momentum that in PYTHIA regularizes the divergence of the leading order scattering amplitude as the final state parton transverse momentum $\hat{p}_T$ approaches 0. The tune Z2 is similar to Z1, except for the transverse momentum cut-off at the nominal energy of $\sqrt{s_0} = 1.8$ TeV which is decreased from 1.932 GeV/c to 1.832 GeV/c. PYTHIA 8 also uses the new PYTHIA

---

[1] PYTHIA version 8.108 is used in the feasibility studies reported in section 2.2.3.
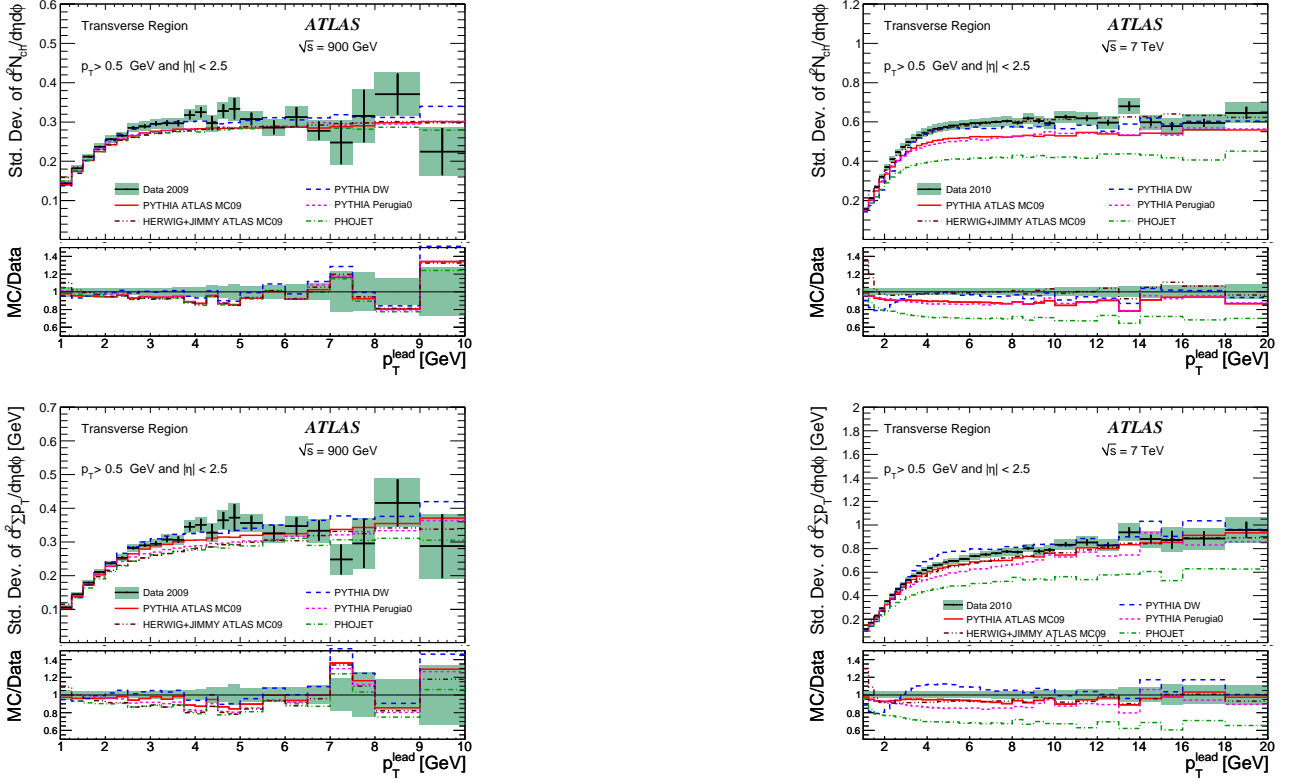
Fig. 4. TLAS data at $\sqrt{s} = 900$ GeV (left) and 7 TeV (right), showing the standard deviation of the density of the charged particles (top row) and the standard deviation of the scalar $\sum p_T$ density of charged particles (bottom row) in the transverse region.
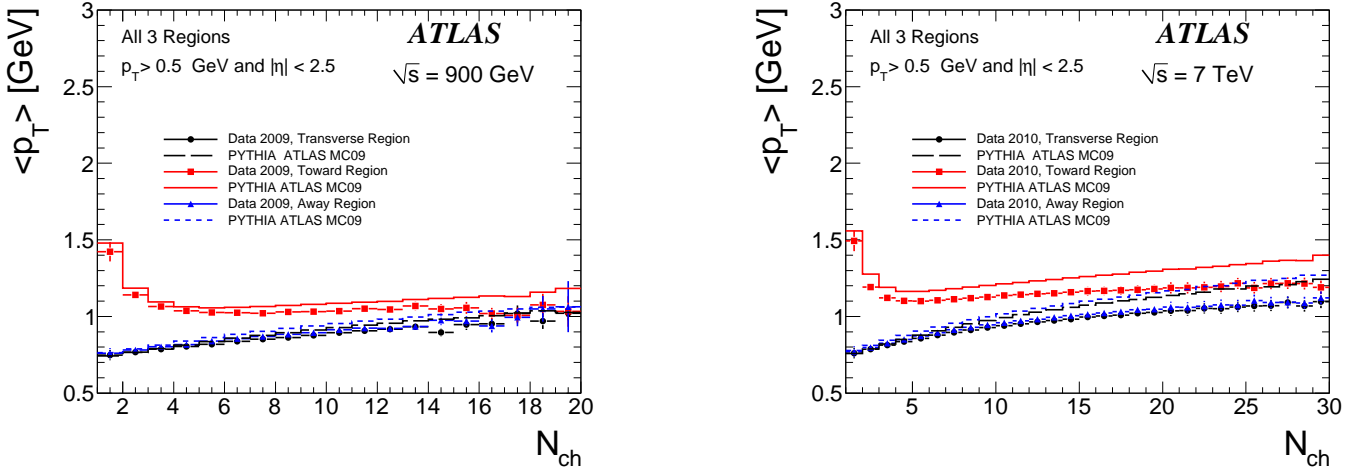

Fig. 5. ATLAS data at $\sqrt{s} = 900$ GeV (left) and 7 TeV (right), showing the mean p_T of the charged particles against the charged multiplicity in all three regions.
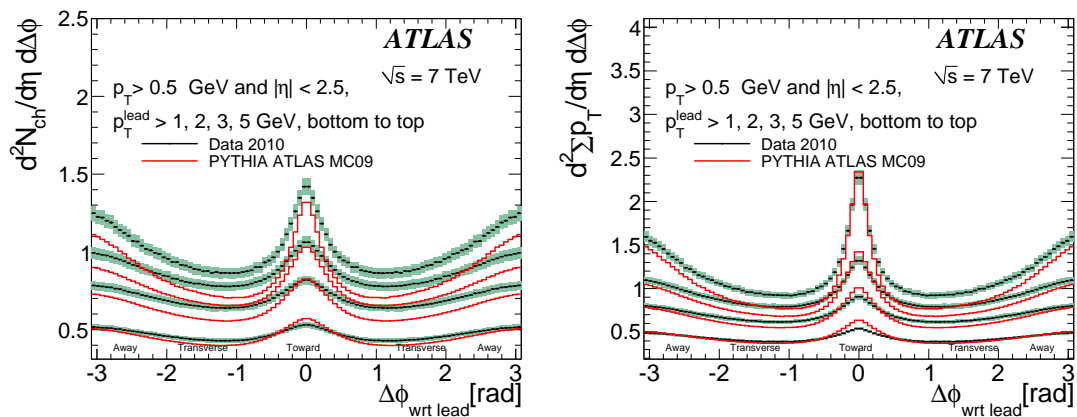
Fig. 6. ATLAS data showing the ϕ distribution of charged particle multiplicity (left) and scalar $\sum p_T$ density (right), with respect to the leading charged particle rotated to $\phi_{\text{leading}} = 0$, excluding the leading charged particle and compared to different MC model predictions. The distributions obtained by restricting the minimum leading charged particle p_T to different values are shown separately. The plots were symmetrized by reflecting them about $\Delta\phi = 0$
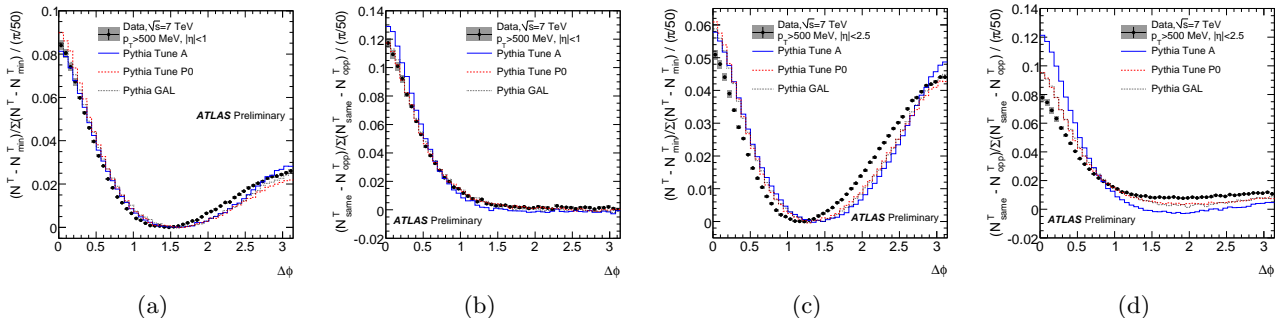

Fig. 7. The $\Delta\phi$ crest shape obtained by subtracting the minimum are shown in (a) and (c), while those obtained by the subtracting the 'opposite from same' are shown in (b) and (d). The left two plots are for $|\eta| < 1.0$ and the right two plots are for $|\eta| < 2.5$.

MPI model, which is interleaved with parton showering. The default Tune 1 is adopted here. PYTHIA 8 includes soft and hard diffraction [38], whereas only soft diffraction is included in PYTHIA 6; the diffractive contributions are, however, heavily suppressed by the trigger and event selection requirements, especially for large p_T values of the leading track-jet. The parton distribution functions used to describe the interacting protons are the CTEQ6LL set for D6T and Z2 and the CTEQ5L set for the other simulations [39,40].

2.2.1 The Early Underlying Event Measurements

In the presence of a hard process, characterized by particles or clusters of particles with a large transverse momentum p_T with respect to the beam direction, the final state of hadron-hadron interactions can be described as the superposition of several contributions: products of the partonic hard scattering with the highest p_T, including initial and final state radiation; hadrons produced in additional MPI; "beam-beam remnants" (BBR) resulting from the hadronization of the partonic constituents that did not participate in other scatterings. Products of MPI and BBR form the UE, which cannot be separated from initial and final state radiation.

The early CMS UE measurements focus on the understanding of the UE dynamics studying charged particle production with two different approaches. The first (traditional) approach [7,37] concentrates on the study of the transverse region, which is defined considering the azimuthal distance of the reconstructed tracks with respect to the leading track or leading track-jet of the event: $60° < |\Delta\phi| < 120°$. The jet reconstruction algorithm used in these studies is SisCone [41]. On top of the traditional approach, a new methodology using anti-k_T jets [42] and relying on the measurement of their area [43] is adopted for the first time by CMS using charged particles in pp collision data collected at $\sqrt{s} = 0.9$ TeV [44]. The new set of UE observables consider the whole pseudorapidity-azimuth plane instead of the transverse region and inherently take into account the leading jets of an event.
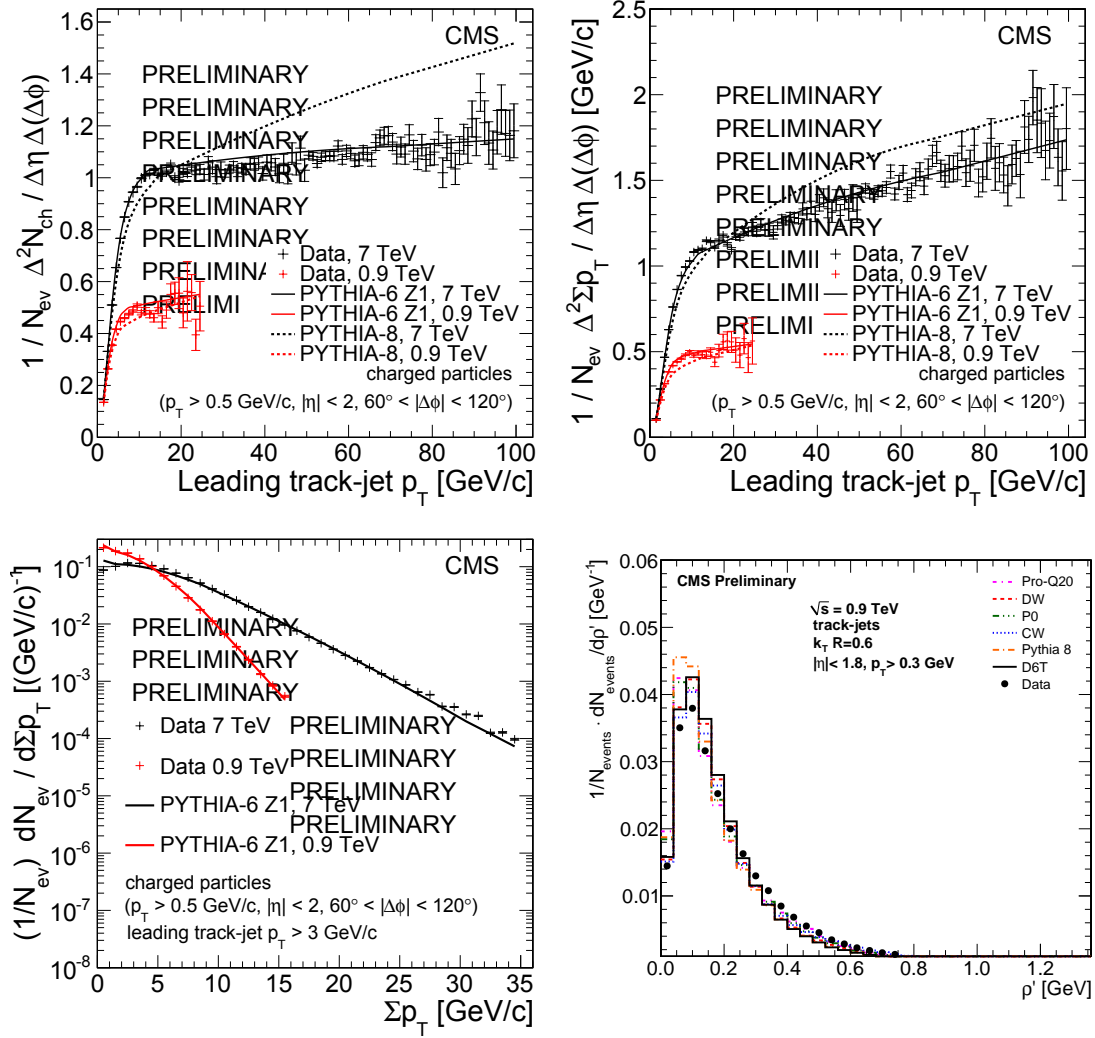
Fig. 8. (Upper plots) average multiplicity and average scalar $\sum p_T$ in the transverse region as a function of the leading track-jet p_T, for data at $\sqrt{s} = 0.9$ TeV and $\sqrt{s} = 7$ TeV. (Bottom left plot) normalized scalar $\sum p_T$ distribution in the transverse region for data at $\sqrt{s} = 0.9$ TeV and $\sqrt{s} = 7$ TeV; the leading track-jet is required to have $p_T > 3$ GeV/c. Predictions from PYTHIA 6 tune Z1 and PYTHIA 8.135 Tune 1 are compared to the corrected data. The inner error bars indicate the statistical uncertainties affecting the measurements, the outer error bars thus represent the statistical uncertainties on the measurements and the systematic uncertainties affecting the MC predictions added in quadrature. (Bottom right plot) normalized median of p_T over jet area for track-jets reconstructed from collision data at $\sqrt{s} = 0.9$ TeV (black circles). Predictions from several PYTHIA 6 tunes and PYTHIA 8 Tune 1 are compared to data.

The centre-of-mass energy dependence of the hadronic activity in the transverse region is presented on the two top Figures 8 as a function of the p_T of the leading track-jet. The data points represent the average multiplicity and average scalar track-p_T sum dependence, for $\sqrt{s} = 0.9$ TeV and $\sqrt{s} = 7$ TeV using tracks with a pseudorapidity $|\eta| < 2.0$ and $p_T > 0.5$ GeV/c. A significant growth of the average multiplicity and of the average scalar p_T sum of charged particles transverse to that of the leading track-jet is observed with increasing scale provided by the leading track-jet p_T, followed by saturation at large values of the scale (more evident for multiplicity profile than average scalar p_T sum). A significant growth of the activity in the transverse region is also observed, for the same value of the leading track-jet p_T, from $\sqrt{s} = 0.9$ TeV to $\sqrt{s} = 7$ TeV. These observations are consistent with the ones obtained at Tevatron [45]. The evolution with the hard scale of the ratio of the UE activity at 7 TeV and 0.9 TeV is remarkably well described by the Z1 MC. The trend is also reproduced by PYTHIA 8. The Z2 predictions at $\sqrt{s} = 0.9$ TeV (not shown here) agree with Z1 in shape, but the normalization is 5-10% higher for both the observables; this trend is opposite with respect to the one observed at 7 TeV and indicates that a less pronounced $\sqrt{s}$ dependence of the transverse momentum cut-off should be adopted for tunes using the CTEQ6LL PDF set than for the tunes optimized for the CTEQ5L set.

The strong growth of UE activity with charged particles is also striking in the comparison of the normalized distributions of charged particle multiplicity (not shown here) and of scalar p_T sum which is presented in bottom-left plot of Figure 8 for events at $\sqrt{s} = 0.9$ TeV and $\sqrt{s} = 7$ TeV with leading track-jet $p_T > 3$ GeV/c. The particle p_T spectrum (not shown) extends up to $p_T > 10$ GeV/c, indicating the presence of a hard component in particle production in the transverse region. The distributions for track-jet $p_T > 3$ GeV/c, which extend up to quite large values of the selected observables in the transverse region are quite well described by the various MC models, over several orders of magnitude. This observation gives support to the implementation of MPI in PYTHIA.

The novel technique to quote the UE activity relies on the introduction of "ghosts", virtual deposits of very low energy filling the overall phase space which are taken into account by the jet clustering algorithm. The estimator of the overall soft background activity in an event can be derived as the median of the ratio between the transverse momentum and the area of the jets. One of the advantages of using the median compared to the mean is that it turns out to be less sensitive to the influence of outliers, i.e. in particular the leading jets in an event. In order to cope with the low occupancy observed at $\sqrt{s} = 0.9$ TeV, CMS redefines such observable restricting the median only to those jets which have physical deposits on top of ghosts:

$$\rho' = \text{median}\left[\left\{\frac{p_{\text{T}j}}{A_j}\right\}\right] \cdot C \tag{1}$$

where C is the occupancy of the event, which is the summed area $\sum_j A_j$ covered these jets divided by the considered detector region A_{tot}. In the CMS analysis at $\sqrt{s} = 0.9$ TeV, jets are reconstructed with the anti-K_T algorithm [42] using tracks with $|\eta| < 2.0$ and $p_T > 0.3$ GeV/c. In the right bottom plot of Figure 8 the ρ' observable is presented for minimum bias events. The general pattern of deviations from data with respect to the considered PYTHIA tunes looks rather similar to the one observed with the traditional UE measurement.

2.2.2 Study of the Activity in the Forward Region

CMS reports a measurement of the energy flow in the forward region ($3.15 < |\eta| < 4.9$, where η denotes the pseudorapidity) [46] for minimum bias and dijet events in pp interactions with centre-of-mass energies $\sqrt{s}$ of 0.9 TeV, 2.36 TeV and 7 TeV. This measurement is connected to the ones reported in the previous sections as the basic philosophy is the same: it concentrates on the complementary activity of a pp interaction for different energy scales of the reconstructed leading objects.

The energy flow in the region of the Hadron Forward detector is measured in two different event classes: in minimum bias events and in events with a hard scale provided by a dijet system at central pseudorapidities ($|\eta| < 2.5$) and with transverse energy $E_{T,jet} > 8$ GeV for $\sqrt{s} = 0.9$ TeV and 2.36 TeV; the dijet threshold is increased to 20 GeV for $\sqrt{s} = 7$ TeV. The results are qualitatively similar at all the investigated centre of mass energies. Fig. 9 shows the results of the forward energy flow at $\sqrt{s} = 7$ TeV for the two event classes compared to predictions from Monte Carlo event generators. The measured forward energy flow is found to be significantly different between the two event classes, with a sensitive increase and a more central activity seen in dijet events.

2.2.3 Multiple Parton Interactions in High-p_T Phenomenology

Quantifying the MPI cross sections basically deals with the measurement of σ_{eff}, the scale factor which characterizes the inclusive rate of the interactions [47,48], cf. Chapters 4 and 5. From a phenomenological point of view σ_{eff} is a non perturbative quantity related to the transverse size of the hadrons and has the dimensions of a cross section. The measurements performed by the AFS, CDF and D0 collaborations [1,3,49,50] favor smaller values of σ_{eff} with respect to the naive expectations. The consequently increased rates of multiple parton interactions can be interpreted as an effect of the hadron structure in transverse plane [51]. Extending such measurements at the LHC and studying the possible scale dependency of σ_{eff} is definitely of great interest and may have a deep impact on the data driven estimations of the MPI backgrounds to new physics.

The production of four high-p_T jets is the most prominent process to search for multiple high p_T scatterings: two independent scatters (i.e. DPS) in the same pp or $p\bar{p}$ collision, each producing two jets. Such a signature has been searched for by the AFS experiment at the CERN ISR, by the UA2 experiment at the CERN S$\bar{p}p$S and by the CDF and D0 experiment at the Fermilab Tevatron.

However, searches for double-parton scattering in four-jet events at hadron colliders may face significant backgrounds from other sources of jet production, in particular from QCD bremsstrahlung (Fig. 10-left). Typical thresholds employed in jet triggers bias the event sample towards hard scatterings. However, a high-p_T jet parton is more likely to radiate additional partons, thus producing further jets. Thus, the relative fraction of jets from final-state showers
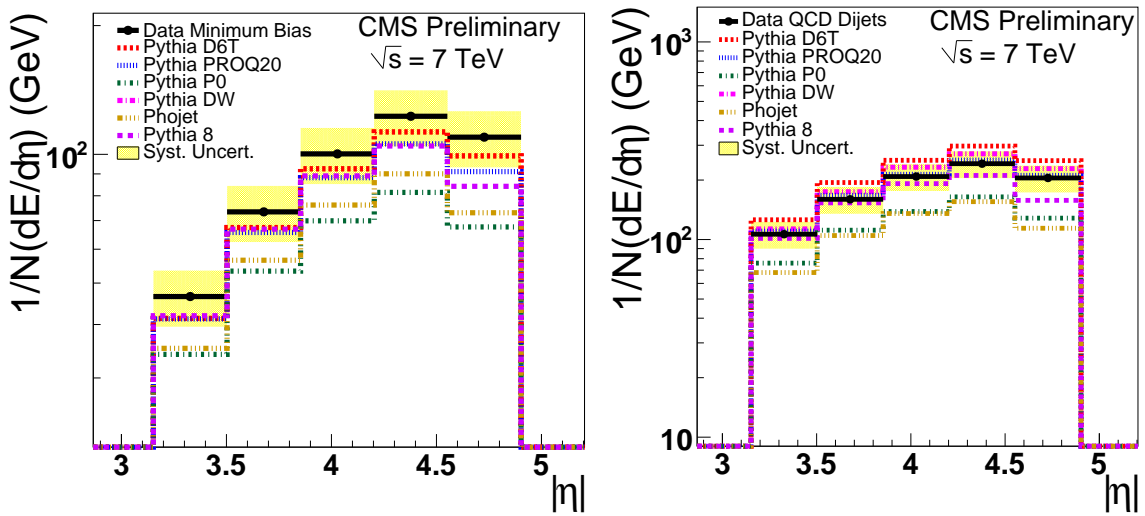
Fig. 9. Energy flow in the minimum bias (left) and di-jet (right) samples as a function of η_{obs} at $\sqrt{s} = 7$ TeV. Uncorrected data are shown as points, the histograms correspond to the MC predictions. Error bars corresponds to statistical errors. The shaded bands in these plots represent the systematic uncertainties of the measurements, which are largely correlated point-to-point.
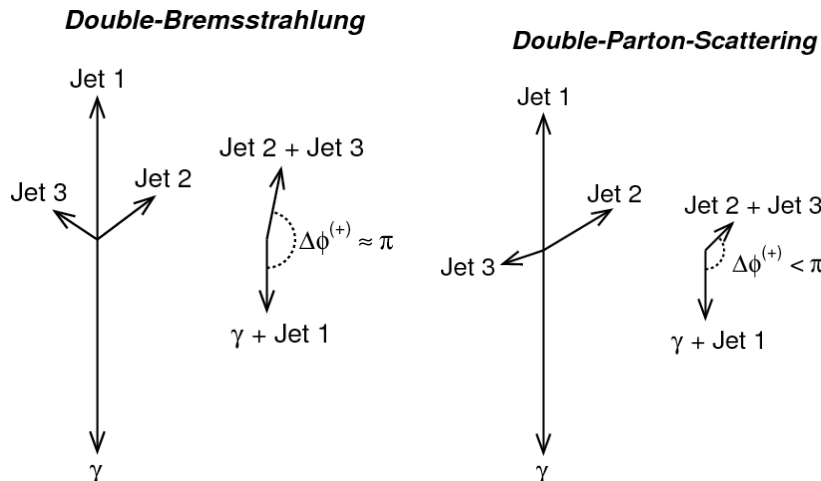

Fig. 10. Definition of azimuthal angle between pairs, together with typical configurations of double-bremsstrahlung (left) and double-parton scattering events (right).

above a given threshold is enlarged in jet trigger streams which is an unwanted bias. On the other hand, looking for four jets in a minimum-bias stream will yield little statistics.

Therefore the strategy to directly measure the MPI rate in high-p_T regime at hadron colliders also includes the study of multi-jets or jets+photon final states. Indeed the CDF and D0 collaborations studied final states with one photon and three jets looking for pairwise balanced photon-jet and dijet combinations. The data sample was selected with the experiment's inclusive photon trigger, thereby avoiding a bias on the jet energy. The better energy resolution of photons compared to jets purifies the identification of E_T balanced pairs. Tevatron found an excess in pairs that are uncorrelated in azimuth with respect to the predictions from models without additional hard parton scatters per proton-proton scatter. CDF interpreted this result as an observation of double-parton-scatters.

Analyses trying to identify two hard scatters in multi-jet events typically rely on methodologies which overcome combinatorics. There are three possible ways to group four objects into two pairs: combinations are commonly selected pairing objects which are balanced in azimuth and energy. The flavor or other specific features of the jets may be used to decrease the combinatorics and to make looser the constraints on the balancing. One example of such a final state is constituted by events with two b jets and two additional light jets.

In order to discriminate double-parton scatters against double-bremsstrahlung events, CMS studies the observables $\Delta\phi^{(-)}$, employed by AFS, and $\Delta\phi^{(+)}$, employed by CDF, probing the azimuthal angle between pairs (Fig. 10).
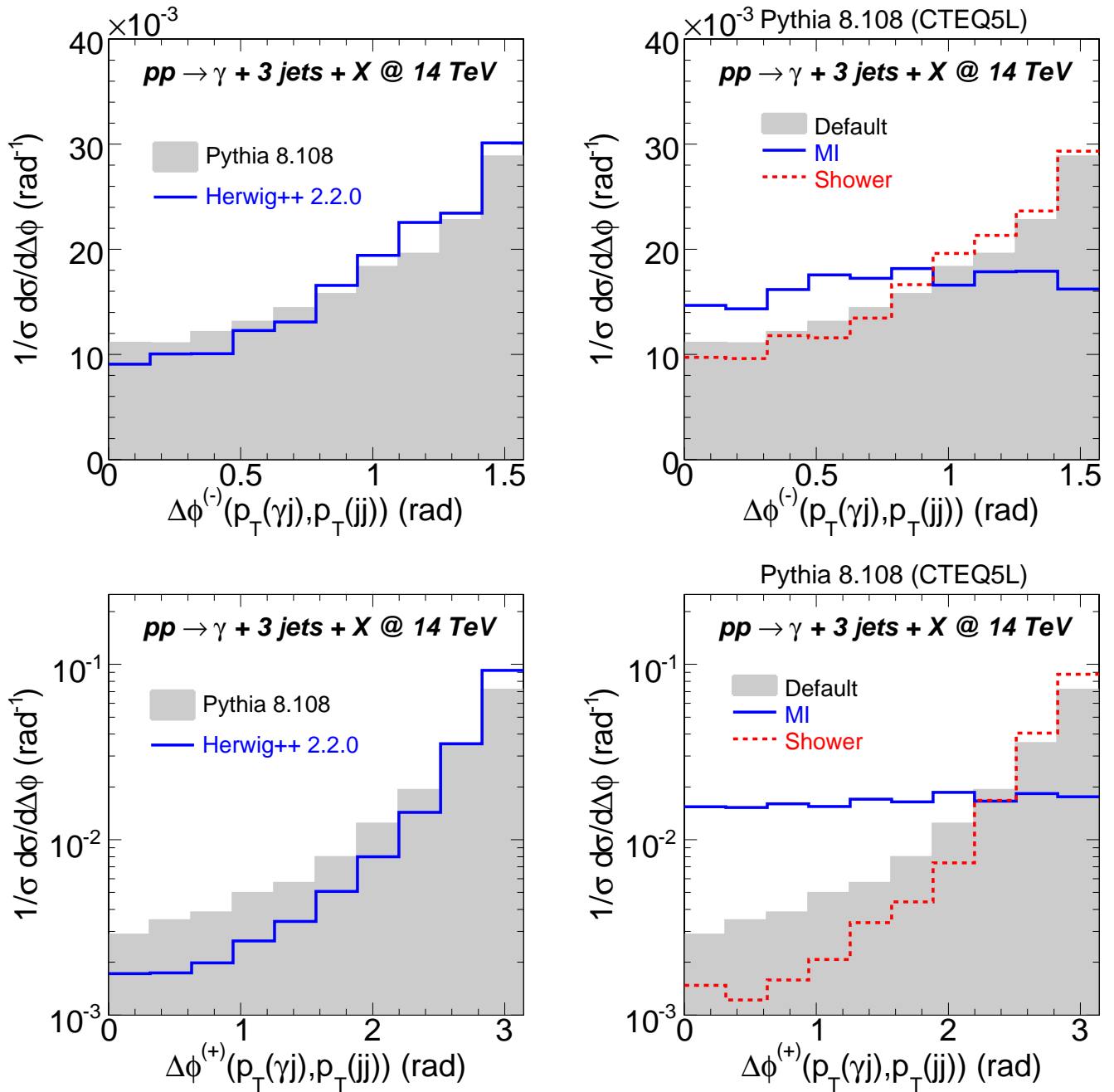
Fig. 11. Differential cross section shape as a function of $\Delta\phi^{(-)}$ (upper plots) and $\Delta\phi^{(+)}$ (bottom plots) variables. Predictions from PYTHIA 8.108 (*Default* scenario) and HERWIG 2.2.0 (left panel) and from three different PYTHIA settings (right panel) shown.

Expectations for the above described variables are therefore $\Delta\phi^{(-)} \approx \pi/2$ and $\Delta\phi^{(+)} \approx \pi$ if additional jets come from double-bremsstrahlung. Otherwise, i. e. if additional jets come from multiple interactions, both variables should be distributed uniformly.

Differential cross section shape predictions for the $\Delta\phi$ observables in pp interactions at 14 TeV are shown in Fig. 11. HERWIG 2.2.0 [19,52] and PYTHIA 8.108 with default settings which include multiple interactions and showering predict similar shapes (Fig. 11-left). The discrimination power of the selected observables to Multiple Parton Interaction patterns is clearly shown in Fig. 11-right, where events with MPI switched off (*Shower* scenario) are compared to events with parton shower switched off (*MI* scenario). The differences are particularly pronounced when selecting the $\Delta\phi^{(+)}$ observable.

2.2.4 Conclusions

A strong growth of the UE activity is observed with increasing leading track-jet p_T for both $\sqrt{s} = 7$ TeV and $\sqrt{s} = 0.9$ TeV. At 7 TeV this fast rise is followed above ~8 GeV/c by a saturation region with nearly constant multiplicity and small p_T increase. The same pattern is observed at 0.9 TeV, with the saturation region starting at ~4 GeV/c. A strong growth of the activity is also observed with increasing centre-of-mass energy. The large increase of activity in the transverse region is also observed in the $\sum p_T$ distribution, indicating the presence of a hard component in the transverse region. Very good post-LHC MC tunes are available for the description of the UE in the central region.

A measurement of the underlying event using the jet-area/median approach is also reported, demonstrating its sensitivity to different underlying event scenarios.

Complementary underlying event measurements in the forward region are also presented. The energy flow in the forward direction is measured for minimum bias and central di-jets events. A more global UE description including both the central and the forward regions is certainly one of the next MC tuning challenges, with deep impact on the understanding of the MPI dynamics.

The Multiple Parton Interactions measurement strategy in the high-p_T regime is also briefly discussed focusing on the $3jet + \gamma$ topology. The very good performances of the LHC machine should allow to have soon the integrated luminosity conditions adequate to perform these measurements over a wide range of energy scales, with deep impact on the data driven estimation of the MPI backgrounds to searches.

2.3 Minimum Bias Physics at LHCb
Contributing author: M. Schmelling (on behalf of the LHCb Collaboration)

At the startup in 2009 the LHC provided proton-proton collisions at a center-of-mass energy of $\sqrt{s} = 0.9$ TeV. Although higher collision energies have previously been reached at proton-antiproton colliders, it was for the first time that the TeV-scale was studied in proton-proton collisions. Using a data sample with an integrated luminosity of only $6.8 \pm 1.0 \, \mu b^{-1}$ recorded by the LHCb detector, a first measurement of the production cross-section of neutral K-mesons was performed in a kinematic range not accessible to the other LHC experiments. In 2010 the collision energy was moved up to 7 TeV and the performance of the machine improved exponentially. Until September LHCb collected an integrated luminosity of over $3 \, pb^{-1}$ with a data acquisition efficiency larger than 90%. At the same time the detector calibration approached its design values. In the following, after a brief description of the detector the first measurements on strangeness production and studies of baryon number transport and baryon suppression in the fragmentation will be presented, before finally discussing prospects for doing diffractive physics with LHCb.

2.3.1 The LHCb Experiment

The LHCb detector [53] is a forward spectrometer, covering the angular range of $15 < \theta < 300 \, \mathrm{mrad}$ with respect to the beam axis. A schematic view of the experiment is shown in Fig. 12. The detector offers tracking, calorimetry and particle identification over most of its forward acceptance. Momenta of charged particles are determined from the deflection by a dipole magnet with a field integral of 4 Tm. The interaction region is surrounded by the Vertex Locator (VeLo). Going downstream, a first RICH detector and the so-called TT tracking station are still located in front of the magnet. Immediately behind the magnet follows the second part of the tracking system, consisting of a high granularity Inner Tracker (IT) in the region of large particle densities close to the beam pipe and the Outer Tracker system at larger transverse distances. VeLo, TT and IT are silicon strip detectors, the OT consists of straw tubes. Following the tracking system is a second RICH detector, a pre-shower and scintillating pad detector (SPD/PS), electromagnetic calorimeter (ECAL), hadron calorimeter (HCAL) and muon system for the identification of electrons and photons, neutral hadrons and muons, respectively. The RICH detectors allow pion, kaon, proton separation in the momentum range between $2 < p < 100 \, \mathrm{GeV}/c$.

The VeLo has 21 double-layer sensor planes for measuring space points and two single-layer planes providing only radial track coordinates. Its layout is shown in Fig. 13. The angular acceptance is larger than for the rest of the tracking system and covers also part of the backward hemisphere. However, being located outside of the magnetic field, VeLo track segments do not have momentum information. Furthermore, since at least three planes are required to reconstruct a track segment, the VeLo is blind in the central region. Charged particle tracks are reconstructed in the rapidity ranges $-4 < \eta < -1.5$ and $1.5 < \eta < 5$.

With the data recorded until summer 2010 a first precise calibration of the various subdetector systems was performed. With the tracking system, for example, impact parameter resolutions for high-p_T particles around $16 \, \mu m$ were reached. Tracking efficiencies above 95% for charged particles with transverse momenta above $p_T = 200 \, \mathrm{MeV}/c$ were determined by a tag and probe approach using daughter particles from K_S^0 and J/ψ decays. The measurements were found to be in good agreement with Monte Carlo simulations, allowing to set a limit on the systematic uncertainty of the tracking efficiency to 3% for high momentum tracks and 4% for soft particles.
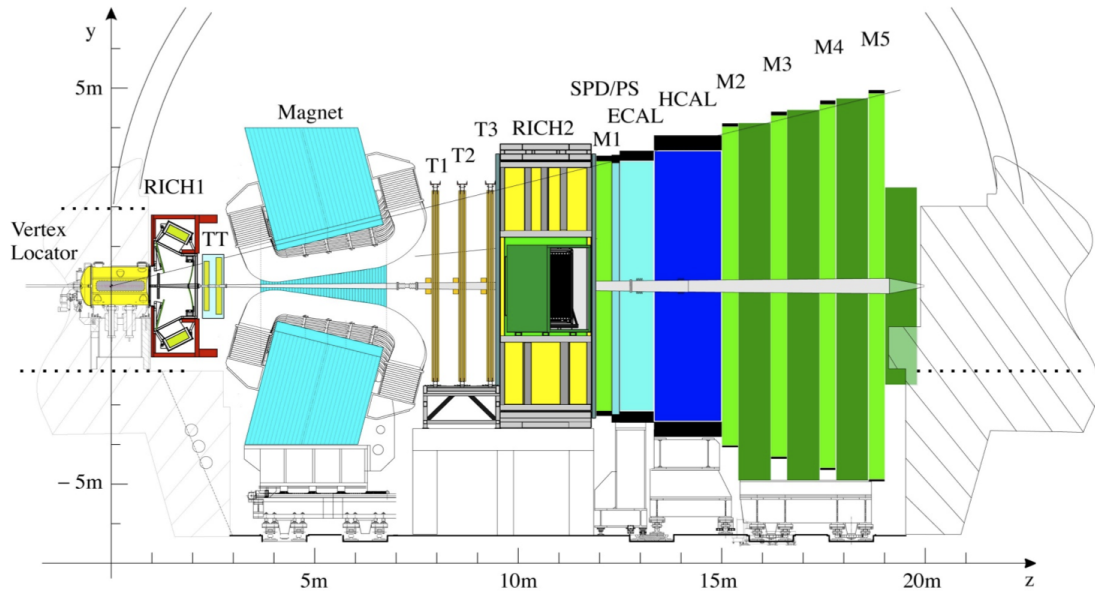
Fig. 12. Schematic view of the LHCb single arm forward spectrometer. The interaction region is located on the left inside the Vertex Locator. The tracking system and the RICH detectors for particle identification are installed both before and after the dipole magnet, calorimetry and the muon system are located downstream of the magnet.
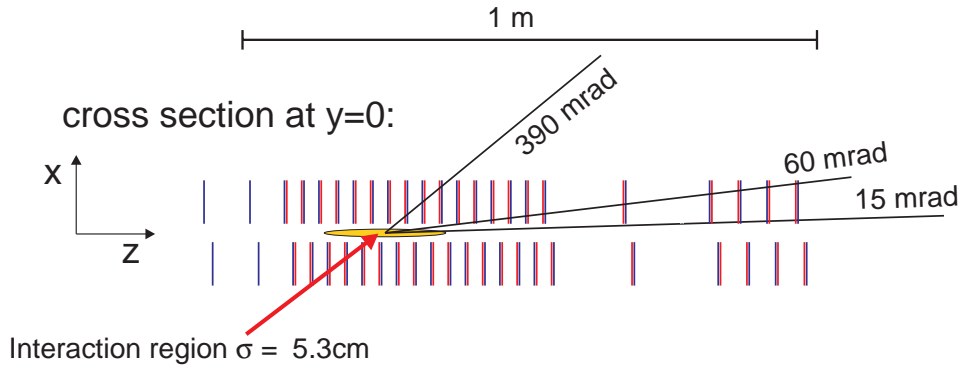

Fig. 13. Layout of the LHCb Vertex Locator (VeLo) in the horizontal (x, z)-plane, with the z-axis along the direction of the proton beams. 21 sensor planes measure space points, the two most backward $(-z)$ layers provide only radial coordinates of charged particle tracks.

2.3.2 Measurements of Strangeness Production

The study of strangeness production is of particular interest for early measurements since, compared to heavy flavours, the cross section is large, and V^0-decays $(K_s^0, \Lambda, \bar{\Lambda})$ have a very clean experimental signature which allows to identify them unambiguously using only kinematical information even when only a coarse calibration of the detector exists. Furthermore, since strange quarks are not present as valence quarks in the initial state and have a mass in an intermediate range where QCD predictions have large uncertainties, they directly probe the mechanism of multi-particle production in high energy collisions where the theory is least well understood.

Results from the first cross-section measurements of prompt K_s^0-production in proton-proton collisions at a center-of-mass energy $\sqrt{s} = 0.9$ TeV [54] are shown in Fig. 14. Uncorrelated errors, mainly due to finite statistics and the modeling of the shape of the differential cross section in the determination of the correction factors, range between 6 and 28 %. The correlated errors are between 16 and 23 % and are dominated by uncertainties in the track finding efficiencies and the luminosity measurement. Comparing experimental results and Monte Carlo predictions, one clearly sees that the data favour a harder p_T-spectrum than the models that were considered. The best description is obtained with the `Perugia0`-tune of PYTHIA, which does not include diffractive processes.
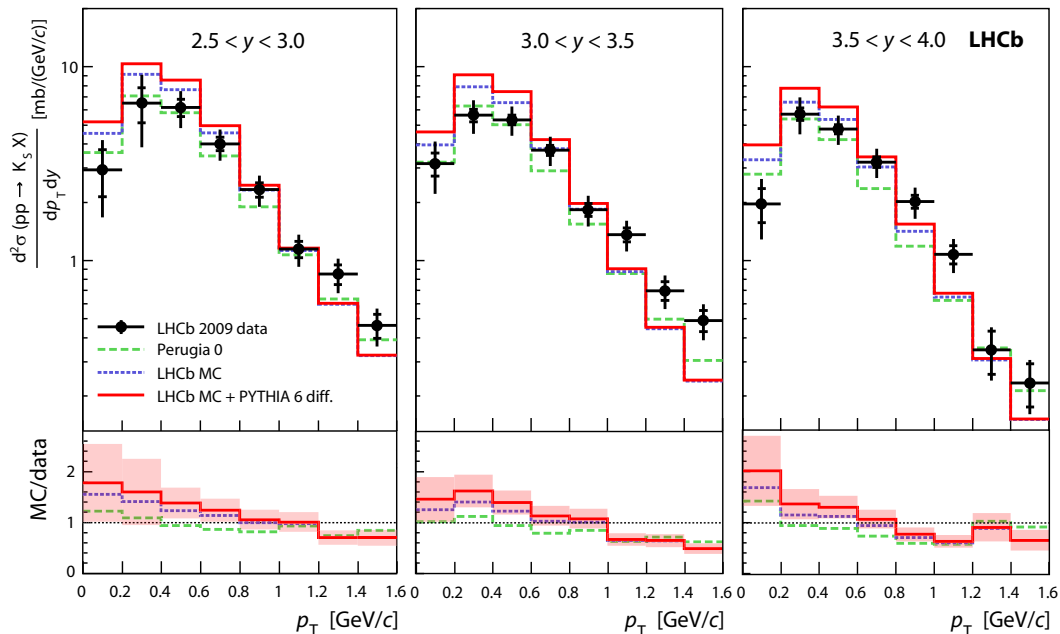
Fig. 14. Differential cross-section for K_s^0-production in pp collisions at $\sqrt{s} = 0.9$ TeV as a function of transverse momentum p_T and rapidity y. The vertical bars on the data points show the total uncertainties, the purely statistical errors are indicated by the tick marks. The histograms are predictions from different settings of the PYTHIA model. The lower plots show the MC/data ratios, with the shaded bands the experimental uncertainty.
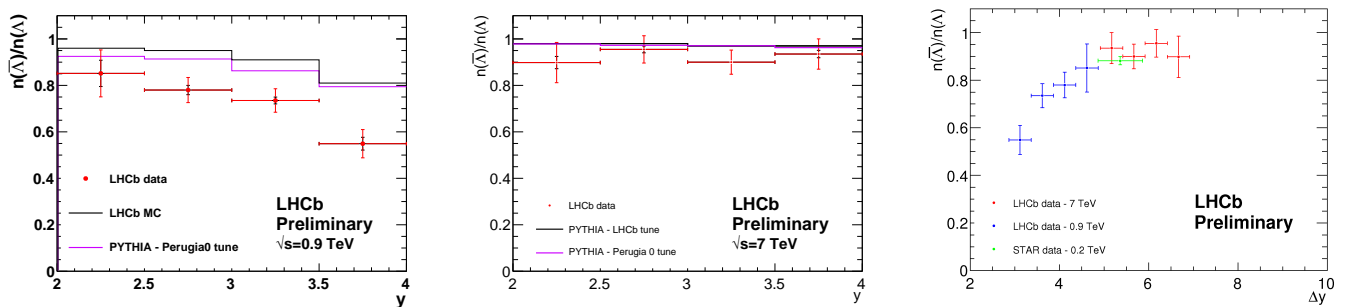

Fig. 15. $\bar{\Lambda}/\Lambda$ cross-section ratio as a function of rapidity for center-of-mass energies $\sqrt{s} = 0.9$ TeV and $\sqrt{s} = 7$ TeV compared with expectations from Monte Carlo models (left), and as a function of the rapidity distance to the beam particle (right).

2.3.3 Baryon Number Transport and Baryon Suppression

Other observables probing the dynamics of particle production in high energy hadron collisions are cross-section ratios, where luminosity and many systematic uncertainties cancel. Results from the study of the $\bar{\Lambda}/\Lambda$ cross-section ratio for center-of-mass energies $\sqrt{s} = 0.9$ TeV and $\sqrt{s} = 7$ TeV are shown in Fig.15. While Λ-baryons have two of their three valence quarks in common with the proton, all three antiquarks of the $\bar{\Lambda}$ have to be produced in the collision. The ratio of the production cross-sections thus measures the baryon-number transport from the beam particles to the final state. In general one observes that the measured ratio is lower, i.e. larger baryon number transport, than the expectation from the Monte Carlo models. The effect becomes stronger in the forward region and when going to lower center-of-mass energies.

A natural variable to study baryon number transport is the rapidity difference to the beam. While for $\sqrt{s} = 0.9$ TeV the beam rapidity is at $y_b = 6.6$ it rises to $y_b = 8.3$ at $\sqrt{s} = 7$ TeV. At the lower energy the LHCb acceptance thus reaches much closer to the beam than at $\sqrt{s} = 7$ TeV. Plotting the $\bar{\Lambda}/\Lambda$ cross-section ratio, as a function of $\Delta y = y_b - y$, also shown in Fig. 15, scaling is observed. The LHCb results are in good agreement with measurements by the STAR collaboration.
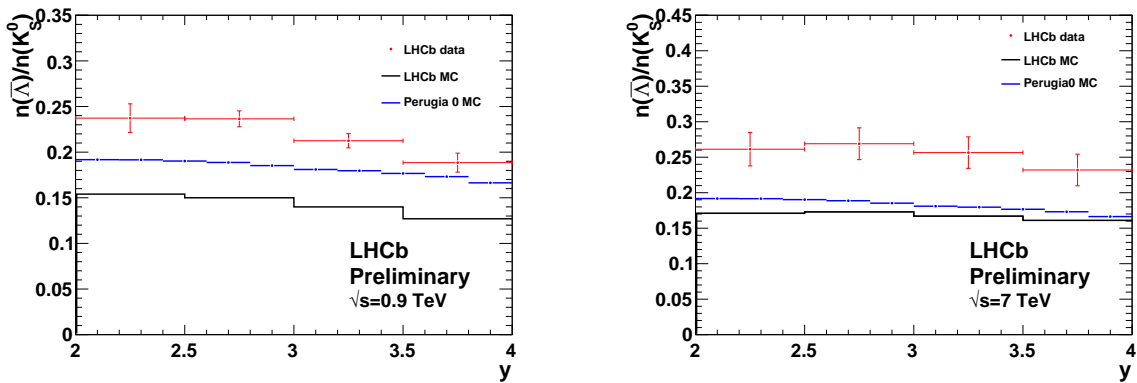
Fig. 16. $\bar{\Lambda}/K_S^0$ cross-section ratio as a function of rapidity for center-of-mass energies $\sqrt{s} = 0.9\,\mathrm{TeV}$ and $\sqrt{s} = 7\,\mathrm{TeV}$. The measurements are compared with expectations from Monte Carlo models. (Note the slightly different vertical scales in the two plots.)
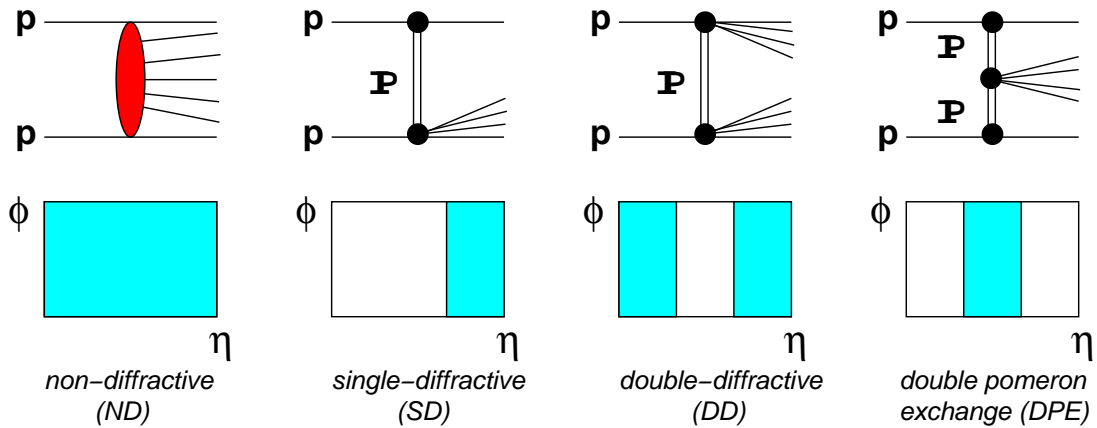

Fig. 17. Schematic classification of inelastic proton-proton collisions. The upper row shows some born-level type diagrams for different classes of interactions, the lower row illustrates the angular range into which particles produced in the collision are emitted. Note that in the upper row rapidity runs from top to bottom, while it goes from left to right in the lower row.

Another ratio to look at is the $\bar{\Lambda}/K_S^0$ cross-section ratio. Since the $\bar{\Lambda}$ has no valence quarks in common with the initial state protons, this ratio measures the suppression of baryon- relative to meson-production. Experimental results compared to Monte Carlo predictions are shown in Fig.16. Both data and Monte Carlo show a slight increase in the ratio when going from $\sqrt{s} = 0.9\,\mathrm{TeV}$ to $\sqrt{s} = 7\,\mathrm{TeV}$. This is plausible, since particle masses and kinematic factors in general should become less important at higher energies. It is, however, striking that in both cases the ratio is significantly underestimated by the Monte Carlo models. Since both the $\bar{\Lambda}$ and the K_S^0 contain a single (anti)strange valence quark, the discrepancy cannot be explained by a mismatch in strangeness suppression between data and Monte Carlo. Instead it probes directly the understanding baryon formation in the fragmentation process.

2.3.4 Prospects for the Study of Diffractive Interactions

A schematic view of different types of inelastic pp-collisions contributing to minimum bias interactions is presented in Fig. 17. Here the basic distinction is colour-octet (gluon) and colour-singlet (pomeron) exchange between the colliding protons. In the language of QCD the pomeron is understood as a color-singlet two-gluon state. Colour exchange implies that the structure of both protons is resolved with the consequence that the colour fields stretched between the partons lead to particle production in the full rapidity range. In contrast, colour-singlet exchange is phenomenologically described by pomerons coupling to the protons as a whole. No colour is transferred and the protons can either scatter elastically or be excited into a high mass state which then decays to produce multi-particle final states. Depending on whether only one or both protons are excited these processes are referred to as single- or double-diffractive scattering. An example for a higher order process involving pomerons is double pomeron exchange, where both protons stay intact and the two pomerons interact to form a massive central system.
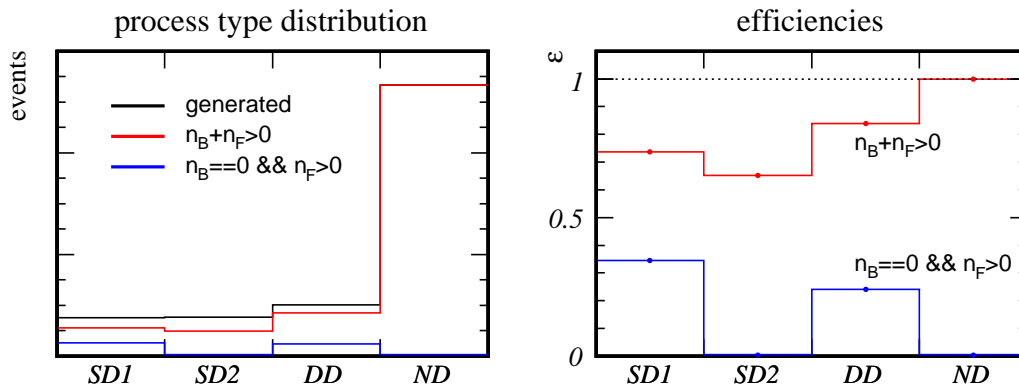
Fig. 18. Generator level MC study: Mix of single diffractive, double diffractive and non-diffractive events generated by PYTHIA 8.135. Here `SD1` refers to single diffractive scattering where the excited proton travels in the direction of the LHCb detector, in `SD2` the decaying heavy mass moves into the opposite direction. The left hand plot shows the mix of events generated (black), passing the VeLo track-segment trigger(red) and the diffraction selection (blue). The right hand plot shows the selection efficiencies for the two cases.
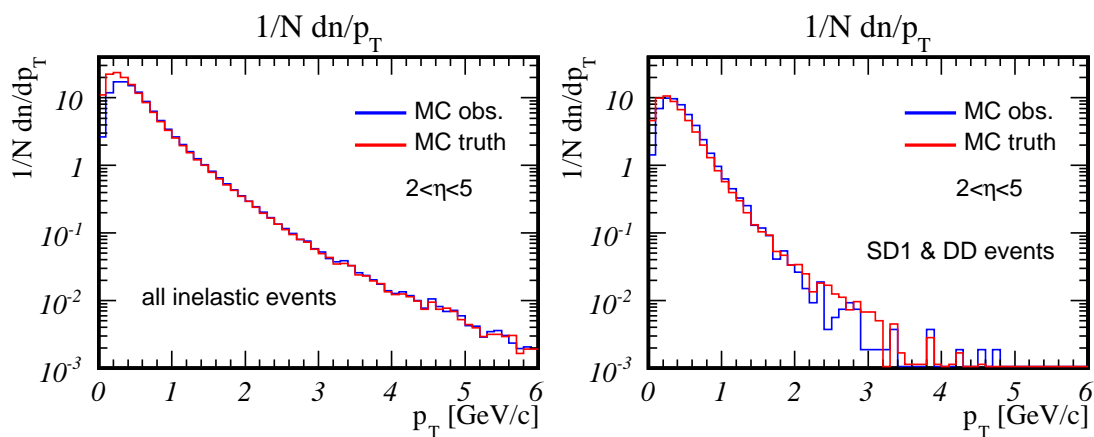

Fig. 19. Generator level MC study: comparison of generated and observable transverse momentum spectra of charged particles in the pseudo rapidity range $2 < \eta < 5$ when asking for a single VeLo track (left) or, in addition, a rapidity gap (right). The spectra are normalized to the number of accepted events. The losses at small transverse momenta are due to incomplete geometric coverage at low p_T and low η.

The above classification of pp-interactions is most adequate at small momentum transfers. With increasing momentum transfer, however, the simple picture breaks down. The two protons are resolved into an increasing number of partons and the interaction is described by ladder-diagrams of all possible topologies. Diffractive and non-diffractive scattering is no longer an unambiguous classification, and even the notion of colour singlet exchange becomes frame dependent 4.5.

Another conceptual problem with Fig. 17 is that the upper row represents Born-level type diagrams, i.e. amplitudes, while the lower one is a pictorial representation of the cross-section. In many Monte Carlo models, such as e.g. PYTHIA [15], the different contributions to the total cross-section are generated independently and interference terms are ignored. Furthermore, parameter tuning generally allows to trade e.g. a larger diffractive component against a smaller non-diffractive part. It follows that event classification into diffractive and non-diffractive parts based on a Monte Carlo implementation is to some extent arbitrary and always model dependent. A better approach would be to avoid any such artificial classifications, and instead perform measurements subject to experimental cuts which enhance or suppress certain contributions to the cross section.

To study the prospects for measuring the properties of events with dominantly diffractive contributions, a simple generator level analysis, ignoring finite resolution and imperfect efficiencies, of charged particle transverse momentum spectra has been performed. The study is based on PYTHIA 8.135 available from [55]. Single proton-proton collisions with a center-of-mass energy $\sqrt{s} = 7$ TeV were generated with process selection `pythia.readString("SoftQCD:all=on")`. The VeLo was simulated with its nominal geometry, and a track was assumed to be measured if at least three stations were hit.

The event selection was based on the VeLo track segments only. Denoting by n_B and n_F the number of VeLo track segments in the backward ($\eta < 0$) and forward ($\eta > 0$) hemispheres, two selection criteria were studied: (a) $n_B + n_F > 0$ and (b) $n_B == 0 \ \&\& \ n_F > 0$. Both criteria ask for at least one track segment in the VeLo, the second corresponds to the additional requirement of a rapidity gap $\Delta\eta = 2.5$ for charged tracks and thus is expected to enhance the fraction of diffractive events in the sample. To obtain a quantitative measure for the level of enrichment which can be achieved, the PYTHIA process type was analyzed for all events. While evidently giving model dependent estimates for the fractions of different events, the qualitative picture is expected to be generic.

For accepted events the transverse momentum spectrum then was determined using all tracks with a VeLo-segment and within the acceptance of the tracking system behind the magnet. The latter was approximated by the requirement $p > 2\,\mathrm{GeV}/c$ the pseudo-rapidity range $2 < \eta < 5$. Results are shown in Figs. 18 and 19. The left hand plot of Fig. 18 shows the mix of single diffractive, double diffractive and non-diffractive events generated by PYTHIA 8.135. One clearly sees that the requirement of a rapidity gap in the backwards region almost completely suppresses non-diffractive events while keeping between 20% and 30% of diffractive interactions. The comparison of the transverse momentum spectra in Fig. 19 shows very good agreement between generated and observed distribution, i.e. a robust measurement comparing the fully inclusive transverse momentum spectra and the spectra in events dominated by diffraction seems feasible. Measurements of production cross-sections for identified particles and particle ratios are a natural extension of these studies.

2.3.5 Summary and Outlook

First results from the study of minimum bias events by the LHCb experiment at center-of-mass energies $\sqrt{s} = 0.9\,\mathrm{TeV}$ and $\sqrt{s} = 7\,\mathrm{TeV}$ have been presented. Production cross-sections for K_S^0-mesons at $\sqrt{s} = 0.9\,\mathrm{TeV}$ were found to have harder transverse momentum spectra than expected from Monte Carlo models. The baryon number transport from the beam particles to the final state was found to scale with rapidity difference to the beam particles and to be more pronounced that expected from the currently used models. The models also feature a stronger baryon suppression in the fragmentation than is observed in the experiment. Finally, a model independent approach towards the study of diffractive particle production in minimum bias events has been presented. Generator level Monte Carlo studies suggest that asking for a rapidity gap of $\Delta\eta = 2.5$ in the backward region of the VeLO allows to select event samples dominated by diffractive processes which, making use of the excellent tracking and particle identification capabilities of the LHCb detector, then can be studied in detail in the pseudo-rapidity range $2 < \eta < 5$.

3 Multi-parton Interactions in Event Generators

The description of low p_T hadronic activity used in experimental analyses relies on models implemented in Monte Carlo (MC) event generators. These generators combine a perturbative description in terms of multiple scatterings with phenomenological models for soft, non-perturbative physics. Recently, the implementation of MPI effects in Monte Carlo models has quickly progressed through an increasing level of sophistication and complexity that has deep general implications for the LHC physics. In this chapter recent developments within the PYTHIA and HERWIG frameworks are reviewed.

3.1 Multiparton Interactions in Pythia 8
Contributing author: R. Corke

3.1.1 MPI in PYTHIA 8

The original MPI model, first introduced in previous versions of PYTHIA, featured $p_\perp$ ordering, perturbative QCD cross sections dampened in the $p_\perp \to 0$ limit, and a variable impact parameter formalism [8]. These features remain in the MPI framework of PYTHIA 8 [56] and have been extended to give a wide range of possible underlying-event processes, including all $2 \to 2$ QCD processes, prompt photon production and others [9]. This newer model was developed after the introduction of transverse-momentum-ordered parton showers, opening the way to have a common $p_\perp$ evolution scale for initial-state radiation (ISR), final-state radiation (FSR) and MPI [10]. This common evolution is most important for ISR and MPI, which both directly compete for momentum from the beams.

With such an interleaving, the probability for the ith interaction or shower branching to take place at $p_\perp = p_{\perp i}$ is given by the combined evolution equation

$$
\frac{\mathrm{d}\mathcal{P}}{\mathrm{d}p_\perp} = \left(\frac{\mathrm{d}\mathcal{P}_{\mathrm{MPI}}}{\mathrm{d}p_\perp} + \sum \frac{\mathrm{d}\mathcal{P}_{\mathrm{ISR}}}{\mathrm{d}p_\perp} + \sum \frac{\mathrm{d}\mathcal{P}_{\mathrm{FSR}}}{\mathrm{d}p_\perp} \right)
$$
$$
\times \exp\left(-\int_{p_\perp}^{p_{\perp i-1}} \left(\frac{\mathrm{d}\mathcal{P}_{\mathrm{MPI}}}{\mathrm{d}p'_\perp} + \sum \frac{\mathrm{d}\mathcal{P}_{\mathrm{ISR}}}{\mathrm{d}p'_\perp} + \sum \frac{\mathrm{d}\mathcal{P}_{\mathrm{FSR}}}{\mathrm{d}p'_\perp} \right) \mathrm{d}p'_\perp \right) , \tag{2}
$$

where contributions from MPI, ISR and FSR are unitarised by a Sudakov-like factor. The sums for ISR and FSR run over all initiator and final-state partons respectively, including those for MPI subsystems, giving full showers from these interactions.

Focusing on just the MPI contribution, the probability for an interaction is given by

$$\frac{\mathrm{d}\mathcal{P}_{\mathrm{MPI}}}{\mathrm{d}p_\perp} = \frac{1}{\sigma_{\mathrm{ND}}}\frac{\mathrm{d}\sigma}{\mathrm{d}p_\perp}\,\exp\left(-\int_{p_\perp}^{p_{\perp i-1}}\frac{1}{\sigma_{\mathrm{ND}}}\frac{\mathrm{d}\sigma}{\mathrm{d}p'_\perp}\mathrm{d}p'_\perp\right)\,, \tag{3}$$

where $\mathrm{d}\sigma/\mathrm{d}p_\perp$ is given by the convolution of PDF factors with the partonic QCD $2 \to 2$ cross section. This cross section is dominated by t-channel gluon exchange, and diverges roughly as $\mathrm{d}p_\perp^2/p_\perp^4$. To avoid this divergence, the idea of colour screening is introduced into the model. The concept of a perturbative cross section is based on the assumption of free incoming states, which is not the case when partons are confined in colour-singlet hadrons. One therefore expects a colour charge to be screened by the presence of nearby anti-charges; that is, if the typical charge separation is d, gluons with a transverse wavelength $\sim 1/p_\perp > d$ are no longer able to resolve charges individually, leading to a reduced effective coupling. This is introduced by regularising the interaction cross section according to

$$\frac{\mathrm{d}\hat{\sigma}}{\mathrm{d}p_\perp^2} \propto \frac{\alpha_S^2(p_\perp^2)}{p_\perp^4} \to \frac{\alpha_S^2(p_{\perp 0}^2 + p_\perp^2)}{(p_{\perp 0}^2 + p_\perp^2)^2}\,, \tag{4}$$

where $p_{\perp 0}$ (related to $1/d$ above) is now a free parameter in the model. This parameter is expected to scale with energy, and the ansatz is that it does so in a manner similar to the total cross section, an effective power related to the Pomeron intercept. The form of the scaling is given by

$$p_{\perp 0}(E_{\mathrm{CM}}) = p_{\perp 0}^{\mathrm{ref}} \times \left(\frac{E_{\mathrm{CM}}}{E_{\mathrm{CM}}^{\mathrm{ref}}}\right)^{E_{\mathrm{CM}}^{\mathrm{pow}}}\,, \tag{5}$$

where a reference $p_{\perp 0}$ is given at some reference energy, and scaled according to $E_{\mathrm{CM}}^{\mathrm{pow}}$.

Up to this point, all parton-parton interactions have been assumed to be independent, such that the probability to have n interactions in an event, $\mathcal{P}_n$, is given by Poissonian statistics. This picture is now changed, first by requiring that there is at least one interaction, such that there is a physical event, and second by including an impact parameter, b. In general, the amount of MPI activity in an event will be directly related to the time-integrated overlap of the incoming hadrons during collision, given by

$$\mathcal{O}(b) = \int \mathrm{d}t \int \mathrm{d}^3x\, \rho(x,y,z)\, \rho(x+b,y,z+t)\,, \tag{6}$$

after a suitable scale transformation to compensate for the boosted nature of the incoming hadrons. Different matter distributions are available, including a single Gaussian, double Gaussian and an intermediate overlap function. While requiring at least one interaction results in $\mathcal{P}_n$ being narrower than Poissonian, when the impact parameter dependence is added, the overall effect is that $\mathcal{P}_n$ is broader than Poissonian.

When the $p_\perp$ evolution has come to an end, colour reconnection is performed. It has been noted, especially by Rick Field [57], that a large amount of colour reconnection is necessary to correctly describe data, such as the mean $p_\perp$ as a function of charged multiplicity in minimum-bias events. In PYTHIA 8, this is performed by giving each MPI subsystem a probability to reconnect with a harder system

$$\mathcal{P} = \frac{p_{\perp\mathrm{rec}}^2}{(p_{\perp\mathrm{rec}}^2 + p_\perp^2)}, \qquad p_{\perp\mathrm{rec}} = R*p_{\perp 0}, \tag{7}$$

where R is a user-tunable parameter and $p_{\perp 0}$ is the same parameter as in eq. (4). The idea of colour reconnection can be motivated by noting that MPI leads to many colour strings that will overlap in physical space. Moving from the limit of $N_C \to \infty$ to $N_C = 3$, it is perhaps not unreasonable to consider these strings to be connected differently due to a coincidence of colour, so as to reduce the total string length and thereby the potential energy. With the above probability for reconnection, it is easier to reconnect low $p_\perp$ systems, which can be viewed as them having a larger spatial extent such that they are more likely to overlap with other colour strings. Currently, however, given the lack of a firm theoretical basis, the need for colour reconnection has only been established within the context of specific models.

3.1.2 Rescattering

A process with a rescattering occurs when an outgoing state from one scattering is allowed to become the incoming state of another. This is illustrated schematically in Fig. 20, where (a) shows two independent $2 \to 2$ processes while
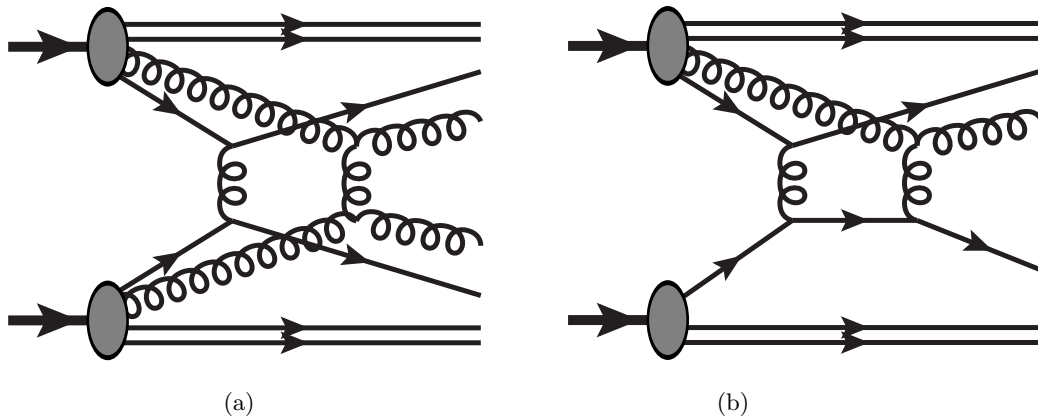
Fig. 20. (a) Two $2 \to 2$ scatterings and (b) a $2 \to 2$ scattering followed by a rescattering

(b) shows a rescattering process. An estimate for the size of such rescattering effects is given by Paver and Treleani [58]. Although rescattering is expected to be a small effect when compared to independent $2 \to 2$ processes, it should be allowed to take place. It would show up in the collective effects of MPI, manifesting itself as changes to multiplicity, $p_\perp$ and other distributions, although after a retuning of $p_{\perp 0}$ and other model parameters, it is likely that its impact is significantly reduced. A full implementation of rescattering has been made, allowing the generation of fully hadronic final states [59], and an outline is given below.

The starting point for the implementation of rescattering is the typical case of small-angle t-channel gluon scattering. In this case, the combination of a scattered parton and one of the hadron remnants will closely match one of the original incoming hadrons, and the PDF can then be written as

$$f(x, Q^2) \to f_{rescaled}(x, Q^2) + \sum_n \delta(x - x_n) \; . \tag{8}$$

Here, each time a scattering occurs, one parton becomes fixed at a specific x_n value, while the remainder is still a continuous probability distribution, although rescaled to take into account the momentum taken from it. In this way, the original disjoint $2 \to 2$ MPI are supplemented by single rescatterings, where one parton is taken from the rescaled PDF and the other is a delta function, and double rescatterings, where both partons are delta functions.

Of course, in general, it is not possible to uniquely identify a scattered parton with one of the hadron remnants, so an approximate prescription must be used. In particular, we have studied a rapidity based scheme, where at one extreme, partons with rapidity $y > 0$ belong to beam A and those with $y < 0$ to beam B ("step") and at the other, all partons belong to both beams simultaneously ("sim"). A natural suppression in the amount of single rescattering for the simultaneous case means that results do not differ greatly compared to the step prescription. The amount of rescattering is also dependent on the amount of underlying activity per event, as the more branchings and scatterings in an event, the more partons that are available to rescatter. To study this effect, two different tunes have been studied. These are labelled "old" and "new", where the primary difference is a reduced amount of MPI activity in the new tune.

In Fig. 21, the $p_\perp$ distribution of single rescatterings is shown compared to normal MPI (pp, $\sqrt{s} = 14 \, \text{TeV}$) for the two tunes. In the ratio plot, double rescattering with the simultaneous prescription and the old tune is also shown (with these settings, the effect is largest). As the $p_\perp$ evolution progresses downwards, more and more partons become available to rescatter and the rate grows. As expected, however, the rate of single rescattering is small compared to normal MPI. As an indicator of the effect of energy on the growth of rescattering, Tab. 1 shows the average number of scatterings and rescatterings for different types of event at Tevatron and LHC energies (step option only, old and new tunes). Double rescattering is always a very small effect and was neglected in the subsequent hadron-level studies.

With the full framework implemented, a range of different observables were studied to look for definitive signatures of rescattering, including exclusive jet rates, effects on the amount of colour reconnection required to match data, enhancement in the $p_\perp$ spectra of final-state hadrons and $\Delta R/\Delta \phi$ distributions. Unfortunately we were unable to find any "smoking-gun" signatures. One possible approach to further study where rescattering plays a role would be to tune the generator, both with and without rescattering, and to examine differences in the overall fit.

3.1.3 Tuning prospects

In this section, tunes of the generator are briefly presented, first for Tevatron data only, and then for an early set of LHC data [60]. Parameters relating to final-state showers and hadronisation have been left unchanged, having been
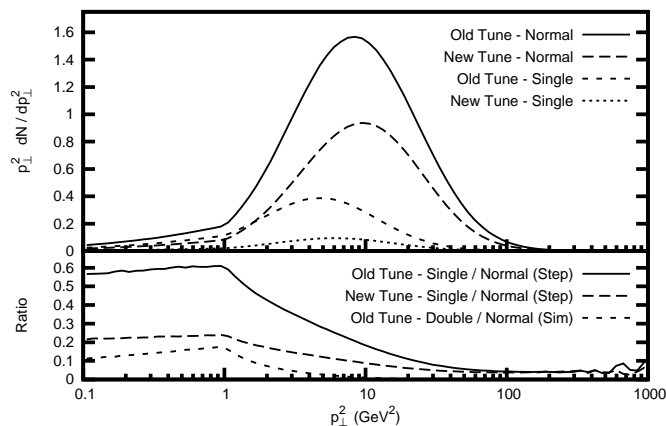
Fig. 21. $p_\perp$ distribution of normal MPI and single rescatterings (pp, $\sqrt{s} = 14$ TeV, old and new tunes). Double rescattering with the simultaneous prescription and the old tune is also shown in the ratio plot

		Tevatron		LHC	
		Min Bias	**QCD Jets**	**Min Bias**	**QCD Jets**
Old	**Scatterings**	2.81	5.09	5.19	12.19
	Single rescatterings	0.41	1.32	1.03	4.10
	Double rescatterings	0.01	0.04	0.03	0.15
New	**Scatterings**	2.50	3.79	3.40	5.68
	Single rescatterings	0.24	0.60	0.25	0.66
	Double rescatterings	0.00	0.01	0.00	0.01

Table 1. Average number of scatterings, single rescatterings and double rescatterings in minimum bias and QCD jet events at Tevatron (p$\bar{\text{p}}$, $\sqrt{s} = 1.96$ TeV, QCD jet $\hat{p}_{\perp\text{min}} = 20$ GeV) and LHC (pp, $\sqrt{s} = 14.0$ TeV, QCD jet $\hat{p}_{\perp\text{min}} = 50$ GeV) energies for both the old and new tunes

previously tuned to LEP data. It should be stressed that the parameter space used to make these tunes is somewhat limited, and the tunes themselves have been made "by hand" following the principles outlined in [60].

Tevatron data

Two tunes to Tevatron data have been produced, Tune 2C using the CTEQ6L1 PDF set and Tune 2M using MRST LO** [40,61]. The MRST LO** PDF set has a relaxed momentum sum rule such that it contains more momentum that CTEQ6L1, leading to lower α_s and higher $p_{\perp 0}$ parameters. For both tunes, the matter distribution uses an overlap function, intermediate between the single Gaussian and the default double Gaussian settings. The balance between ISR and MPI activity is primarily tuned by comparisons to $p_\perp(Z^0)$ and jet-jet azimuthal angle distributions, both of which are driven strongly by ISR.

In Fig. 22, results from Tune 2C are shown using the Rivet analysis framework for (a) the charged multiplicity at $\sqrt{s} = 1.8$ TeV and (b) the transverse region charged particle density in Rick Field's leading jet analysis [62,57,63]. Comparisons are made both to data, and to the Pro-Q20 and Perugia 0 tunes of PYTHIA 6 [35,32]. In both cases, Tune 2C is in good agreement.

LHC data

Tune 4C is a modification of Tune 2C, where MPI and colour reconnection parameters have been changed to give a good match to LHC data (with ISR settings left unchanged). Additionally, the diffractive cross section has been slightly damped, to better match an early ATLAS study [64]. One notable aspect of this tune is a reduced amount of colour reconnection required to match $\langle p_\perp \rangle(N_{\text{CH}})$ data in minimum-bias events. This reduction also affects the balance between the charged particle density and the scalar $p_\perp$ sum density in the transverse region of the underlying event, leading to a slightly worse description of this data.
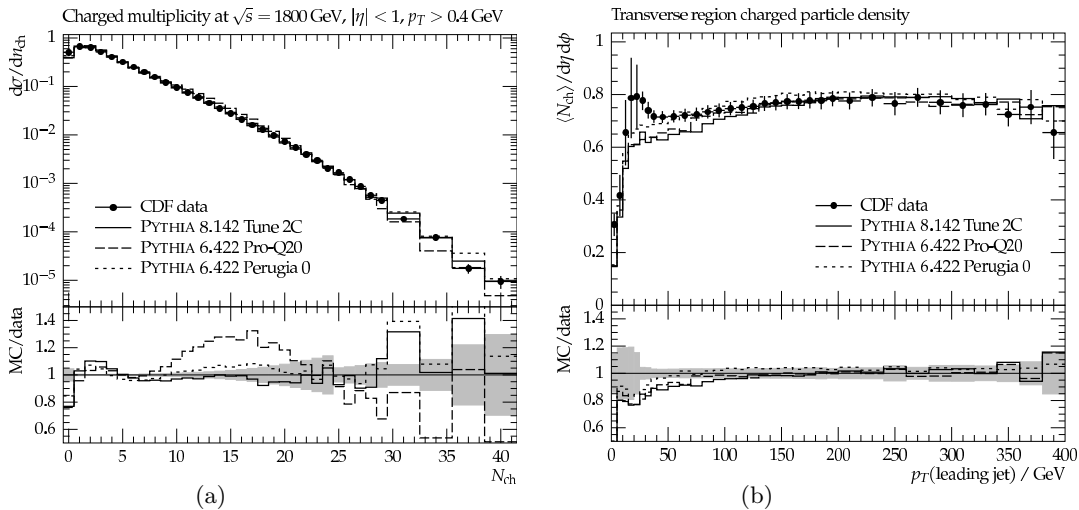
Fig. 22. Results from Tune 2C for (a) the charged multiplicity at $\sqrt{s} = 1.8\,\text{TeV}$ and (b) the transverse region charged particle density in Rick Field's leading jet analysis
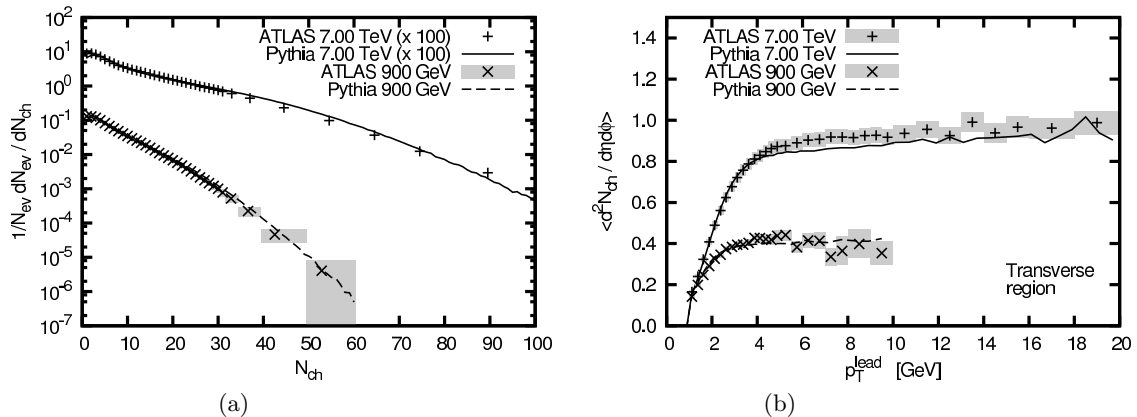

Fig. 23. Results from Tune 4C compared to ATLAS data at $\sqrt{s} = 0.9$ and $7\,\text{TeV}$ showing (a) the charged multiplicity and (b) the transverse region charged particle density

In Fig. 23, results from Tune 4C are shown against ATLAS data at $\sqrt{s} = 0.9$ and 7 TeV showing (a) the charged multiplicity and (b) the transverse region charged particle density [65,66,67]. The broad features of the data are reproduced, and it is hoped that a more complete tuning will increase agreement further. It is noted that Tunes 2C and 2M give too little activity when compared to LHC data and Tune 4C gives too much activity when compared to Tevatron data.

3.1.4 Conclusions

The MPI model in PYTHIA 8 is an evolution of the original framework introduced in earlier versions of PYTHIA and has been well proven in comparisons to experimental data. Of course, it is not the final word in the modelling of soft MPI and undoubtedly there are further physics aspects that can be included. One possible extension we have implemented is rescattering, outlined above. Although we were unable to find a distinct signature for these processes, there is still future scope for the study of effects on an overall generator tune.

Long awaited LHC data are now being published and will hopefully help to constrain different models and model parameters. One current concern is the need for different tunes to describe Tevatron and LHC data, and it remains to be seen if there is some region in parameter space where this is possible. So far it is not possible to rule out differences due to experimental effects or deficiencies in the model, e.g. related to the energy dependence of $p_{\perp 0}$. We look forward to future data that may help to resolve these issues.

3.2 Multiple Partonic Interactions in HERWIG++

Contributing authors: S. Gieseke, Ch. Röhr, A. Siódmok

The modelling of underlying events in Herwig++ is based on the fact that at high enough energies the hard inclusive cross section will eventually exceed the total cross section [52]. Generally speaking, we write the hard inclusive cross section for partonic $2 \to 2$ scatters as

$$\sigma^{\mathrm{inc}}(s; p_t^{\mathrm{min}}) = \sum_{i,j} \int_{p_t^{\mathrm{min}\,2}} \mathrm{d}p_t^2 f_{i/h_1}(x_1, \mu^2) \otimes \frac{\mathrm{d}\hat{\sigma}_{i,j}}{\mathrm{d}p_t^2} \otimes f_{j/h_2}(x_2, \mu^2)\,, \tag{9}$$

which is the usual collinear factorization ansatz. With recent parton distribution functions and lower limits for the transverse momentum, p_t^{min}, in the perturbative regime of a few GeV, Eq. 9 results in values for $\sigma^{\mathrm{inc}}(s; p_t^{\mathrm{min}})$ which exceed the Donnachie–Landshoff (DL) parametrization [68] of the total cross section σ_{tot}. The simplest way out is the observation that the proton is a spatially extended object, allowing for independent multiple hard interactions, which are strictly all taken into account in the calculation of the inclusive cross section. Therefore, we calculate the average number of hard interactions from an eikonal ansatz as

$$\bar{n}(\boldsymbol{b}, s) = A(\boldsymbol{b}; \mu^2)\sigma^{\mathrm{inc}}(s; p_t^{\mathrm{min}})\,. \tag{10}$$

The overlap function $A(\boldsymbol{b}; \mu^2)$ describes the spatial overlap of the two colliding hadrons (protons) as a function of the impact parameter $\boldsymbol{b}$. The parameter μ^2 characterizes the size of the proton and is proportional to the squared inverse radius. For simplicity, we assume a spatial distribution following the functional form deduced from the electromagnetic elastic form factor. But we do allow for a different width parameter μ of the distribution, as the colour might be distributed differently from the electric charges. The basic ideas for this multiple interaction model follow the model in Ref. [11], which in turn introduces a model similar to the one discussed in Ref. [8].

The extension to soft scatterings, similar to the model of Ref. [69], is kept as simple as possible. First, the transverse momentum of scattered particles is extended to transverse momenta below p_t^{min}. The additional soft contribution to the inclusive cross section is also eikonalized, such that we can as well calculate an average number of soft scatters from the resulting $\sigma_{\mathrm{soft}}^{\mathrm{inc}}$ and an overlap function $A_{\mathrm{soft}}(\boldsymbol{b})$ for the soft scattering centers. The functional form $A_{\mathrm{soft}}(\boldsymbol{b})$ is assumed to be the same as for the hard scatters, but we allow for a different inverse radius, μ_{soft}^2. The phase space of the soft scatters is determined with a simple Gaussian ansatz for the transverse momentum, of which the parameter is determined by the value of $\sigma_{\mathrm{soft}}^{\mathrm{inc}}$.

The consistency of this model with unitarity is given by fixing the two additional parameters $\sigma_{\mathrm{soft}}^{\mathrm{inc}}$ and μ_{soft}^2 from two additional constraints. First, we can calculate the total cross section from the eikonal model and fix it to be consistent with the DL parametrization. In addition, using the optical theorem, we can calculate the t–slope parameter from the eikonal model as well and fix it to a reasonable parametrization.

After in a first step only the model for hard multiple partonic interactions has been introduced [12], we also studied its implications from Tevatron data and total cross section data in a simplified version [70]. Finally, the extension of the model to include soft scatters has been implemented in Herwig++ and is the default underlying event model since version 2.3. The consistency of the model predictions with current Tevatron data has been studied in detail in Ref. [71].

3.2.1 Herwig++ against first LHC data

Equipped with the good description of the Tevatron data, we can now take a first look at the ATLAS measurements made at the 900 GeV and 7 TeV runs at the LHC [65, 36]. We anticipate the possibility that the assumptions made in order to extend the model into the soft region may be far too simple. Nevertheless, we have been able to accommodate the detailed underlying event analyses carried out at the Tevatron. There we have come up with regions in the two–dimensional parameter plane of p_t^{min} and μ^2, where we obtain a similarly good overall χ^2 for the underlying event data and still are consistent with our constraints from the total cross section and the elastic slope parameter. This region roughly follows a line. We now had a first look at Minimum Bias data, particularly the relatively simple distribution of charged particles in pseudorapidity.

As a first step, we have varied our model parameters and compared the results against the 900 GeV data. We find that the shape of the pseudorapidity distribution in Herwig++ is by far too much peaked in the forward directions. In addition, there is not enough freedom in our parameter space to describe $\langle p_\perp \rangle(N_{\mathrm{ch}})$.

A first hint towards the possible improvement of our description of data was found when we varied the probability that any of the additional soft scatters gets disconnected in colour space from the rest of the event and the beam remnants in particular. The value cD = 1 was used as a default, saying that the soft scatters have always been disconnected. Physically this means that there are no colour strings built up between the beam remnants and the soft particles produced in the soft underlying event. When they are build up more and more, as we see when we
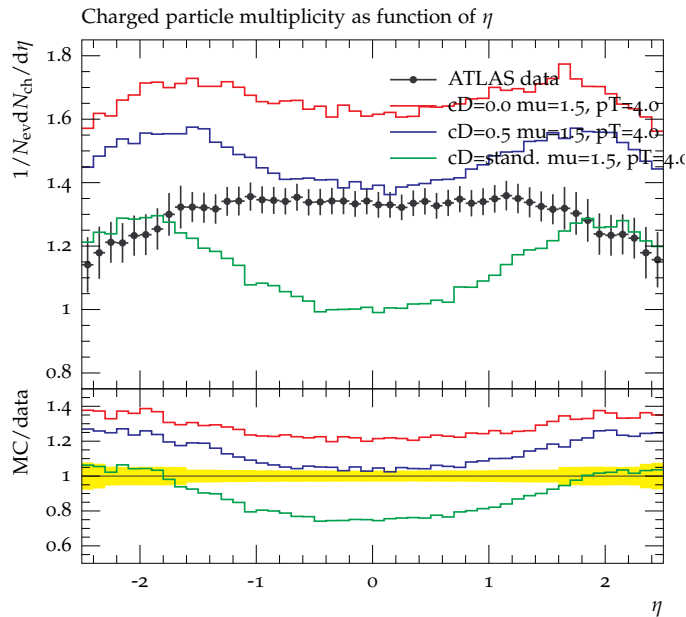
Fig. 24. Pseudorapidity distribution of charged particles in Minimum Bias events at 900 GeV compared to ATLAS data. The most sensitive model parameter was the colour disruption probability for soft events.

vary the parameter towards the other extreme value 0 (always connected), we find that we produce many additional soft particles, resulting in an evenly filled plateau in rapidity. Having checked also other parameters, such as parton distribution functions and their behaviour at small x values, we found that the effect of the colour disruption parameter was most important. Fig. 24 shows the sensitivity to the colour disruption parameter.

A second hint is given by the unability to describe $\langle p_\perp \rangle (N_{ch})$ which is considered to be very sensitive to non-perturbative colour reconnections. So, as final additional modification we have considered a newly implemented model for soft colour reconnections in HERWIG++. We find that only with the two latter modifications we can give a sensible description of minimum bias events.

A colour reconnection model is a very significant modification of the final state as the production of charged particles is affected in its multiplicity as well as in its phase space distribution, once a multiple partonic interaction model is used. Hence, before moving on to LHC data, we have checked the new model against data that we previously described quite well. First we considered LEP final states and found no sensitivity whatsoever. This was expected as the colour structure of the event is well-defined by the perturbative parton shower evolution. The Tevatron underlying event analysis, that we were always able to reproduce, was slightly improved, as expected. In particular, the tension between p_t^{sum} and N_{ch} against the leading-jet transverse momentum has been reduced.

Moving on to the LHC, we have used the ATLAS data with a cut $N_{ch} \geq 6$ in order to remove diffractive events [36] as we currently have no diffractive model in HERWIG++. We have included the variation of the colour disruption parameter and the colour reconnection model and tuned our model to the new data. We used data from the run at $\sqrt{s} = 900$ GeV as well as from $\sqrt{s} = 7$ TeV. The tuned results are shown in Figs. 25 and 26.

We find that the overall agreement with the data is very good. The expected need for the modification of the colour structure in multiple partonic interaction events is in fact given.

3.2.2 Conclusion

We have introduced a simple colour reconnection model in HERWIG++ in order to complete the hadronization of events with multiple partonic interactions. We find very good agreement with first data on non–diffractive Minimum Bias events, measured by ATLAS. The model is included in the recent release HERWIG++ 2.5 [72].

4 Theory of Multi-Parton Scattering

The theoretical investigation of MPI has a long history [73,74,75,47,76] and has experienced a renewed interest in more recent times [77,78,79,51,80,81,82,83,84,85,86], driven by the need to understand the hadronic activity at the
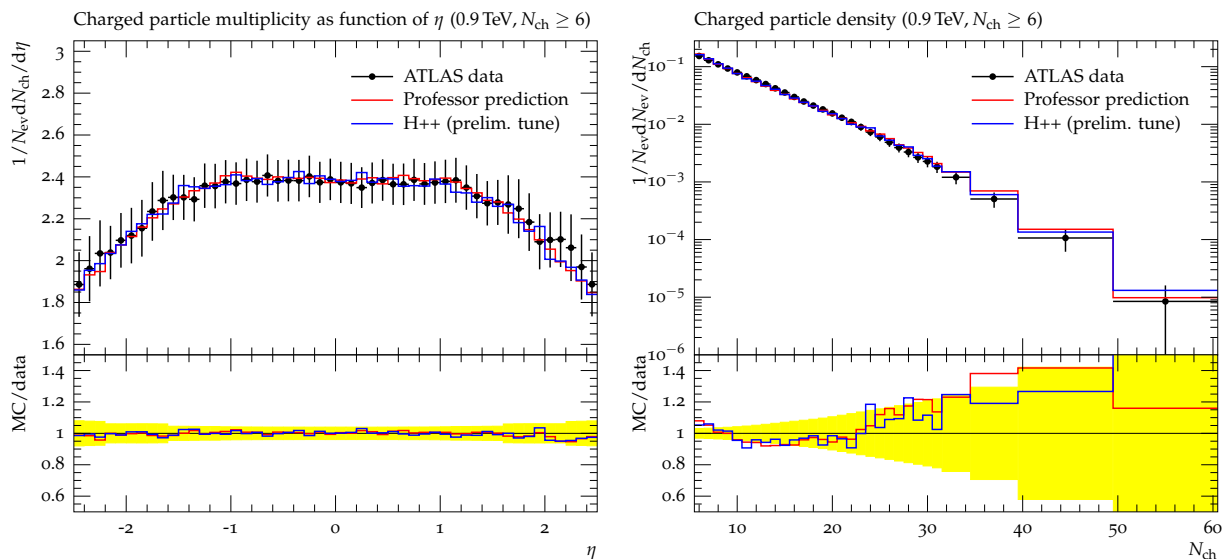
Fig. 25. Pseudorapidity and charged particle distribution from the ATLAS $N_{ch} \geq 6$ analysis at $900\,\mathrm{GeV}$ compared to HER-WIG++. The data points are read off preliminary, but publicly available, ATLAS figures.

LHC. The phenomenology of multiple parton interactions relies on a rather simple and intuitive cross section formula, where multi-parton distributions are multiplied with the cross sections for each individual hard scatter, cf. Chapter 5. It is natural to ask whether such a factorization formula can be derived in QCD and to which extent it needs to be modified or extended. Sections 4.1 and 4.2 present two independent efforts to address these questions, respectively taking the production of two electroweak gauge bosons or of two jet pairs as examples processes for DPS.

Accurate predictions of DPS cross sections also require good modelling of double parton distribution functions (dPDFs) used in phenomenological studies. Typically, they are constructed from standard single PDFs neglecting possible correlations between the longitudinal momenta and transverse positions of the two partons involved. The development of the first set of LO dPDFs in the framework assuming factorization between the longitudinal and transverse components is described in Section 4.3 of this chapter. However, as discussed there and in Section 4.1, the validity of the transverse-longitudinal factorization is being contested.
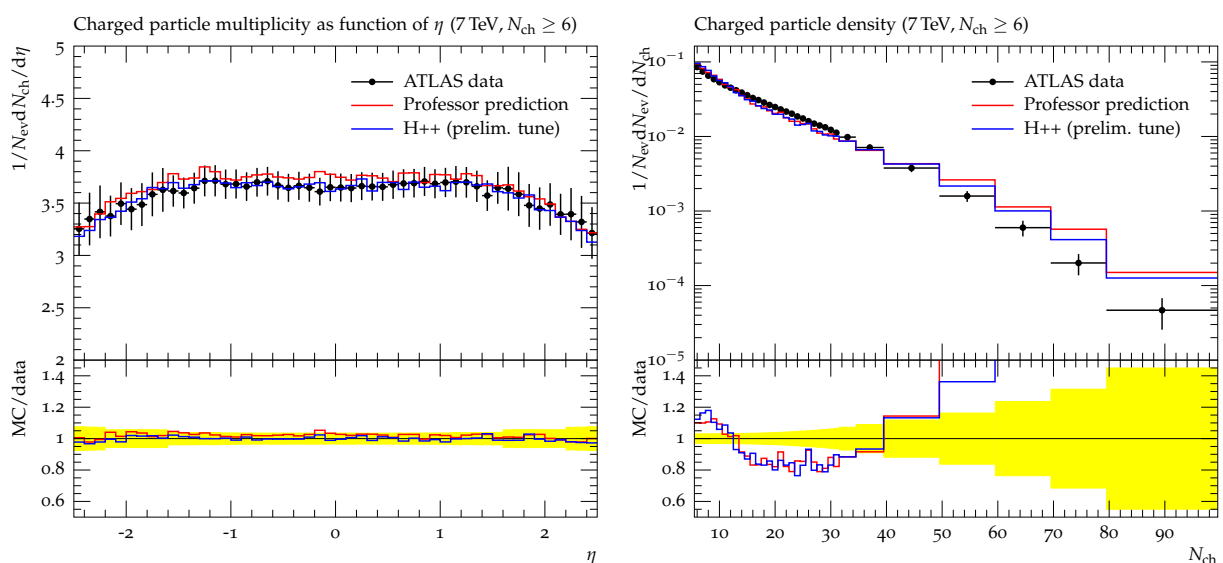

Fig. 26. Pseudorapidity and charged particle distribution from the ATLAS $N_{ch} \geq 6$ analysis at $7\,\mathrm{TeV}$ compared to HERWIG++. The data points are read off preliminary, but publicly available, ATLAS figures.

This chapter contains also a discussion, in Section 4.4, of general features of MPI in a probabilistic framework employing a functional approach. The probabilistic picture naturally leads to considering the inclusive and exclusive cross sections, which are linked by the sum rules. They can be used to obtain information on MPI properties, such as two-particle correlations, since inclusive and exclusive cross sections are measured independently.

The MPI are also very strongly connected to the small-x phenomena of saturation and diffraction. In general, the cut diagrams for MPI differ from multiple parton chain diagrams for saturation and diffraction only by the position of the cut. In high energy pp scattering unitarity requires the presence of MPI as well as a large diffractive cross section. A model to describe diffractive excitations, its relation with the multi-regge formalism and its MC implementation is discussed in Section 4.5.

4.1 Multiple parton interactions: some theoretical considerations
Contributing author: M. Diehl

4.1.1 The basic cross section formula

As an example for a process to which multiparton interactions contribute we consider the production of two electroweak gauge bosons (W, Z or γ^*) with transverse momenta much smaller than their masses or virtualities. Since the driving force for studying multiple interactions is the necessity to describe details of the final state, we keep the cross section differential in the transverse boson momenta. For the production of a single gauge boson there is a powerful theory involving transverse-momentum dependent parton densities [87,88,89,90], which can to a large extent be generalized to the case of multiple hard scattering.

Figure 27a shows a graph for two-boson production by double parton scattering. This graph can be evaluated using the standard hard-scattering approximations, neglecting small momentum components compared with large ones. Simple kinematic considerations show that the transverse momenta of the scattering partons are in general *not* equal in the scattering amplitude and its complex conjugate, as indicated in the figure. It is convenient to Fourier transform from the transverse-momentum differences $\boldsymbol{r}$ and $\bar{\boldsymbol{r}}$ to transverse position variables $\boldsymbol{y}$ and $\bar{\boldsymbol{y}}$. The constraint $\boldsymbol{r} + \bar{\boldsymbol{r}} = \boldsymbol{0}$ from momentum conservation then turns into $\boldsymbol{y} = \bar{\boldsymbol{y}}$ for the Fourier conjugate positions, and the cross section reads[2]

$$\frac{d\sigma}{\prod_{i=1}^{2} dx_i\, d\bar{x}_i\, d^2\boldsymbol{q}_i}\bigg|_{\text{Fig. 27a}} = \frac{1}{S} \sum_{\substack{a_1,a_2=q,\Delta q,\delta q \\ \bar{a}_1,\bar{a}_2=\bar{q},\Delta\bar{q},\delta\bar{q}}} \left[\prod_{i=1}^{2} \int d^2\boldsymbol{k}_i\, d^2\bar{\boldsymbol{k}}_i\, \delta^{(2)}(\boldsymbol{q}_i - \boldsymbol{k}_i - \bar{\boldsymbol{k}}_i) \right]$$

$$\times\, \hat{\sigma}_{1,a_1\bar{a}_1}(q_1^2)\, \hat{\sigma}_{2,a_2\bar{a}_2}(q_2^2) \int d^2\boldsymbol{y}\, F_{a_1,a_2}(x_i, \boldsymbol{k}_i, \boldsymbol{y})\, F_{\bar{a}_1,\bar{a}_2}(\bar{x}_i, \bar{\boldsymbol{k}}_i, \boldsymbol{y})\,, \tag{11}$$

where $\hat{\sigma}_{i,a_i\bar{a}_i}$ denotes the hard-scattering cross section for single-boson production. The statistical factor S is 2 if the produced bosons are identical and 1 if they are not. Up to power corrections, the momentum fractions of the colliding partons are fixed by the measurable momenta as

$$x_i = q_i^+/p^+ = (k_i^+ \pm \tfrac{1}{2}r^+)/p^+\,, \qquad\qquad \bar{x}_i = q_i^-/\bar{p}^- = (\bar{k}_i^- \pm \tfrac{1}{2}\bar{r}^-)/\bar{p}^-\,, \tag{12}$$

---

[2] In other parts of this chapter, and in Chapter 5, the symbols D or Γ are used to denote the multiple parton distributions instead of F used here. Similarly, transverse coordinates are denoted by $\boldsymbol{b}$, instead of $\boldsymbol{y}$.
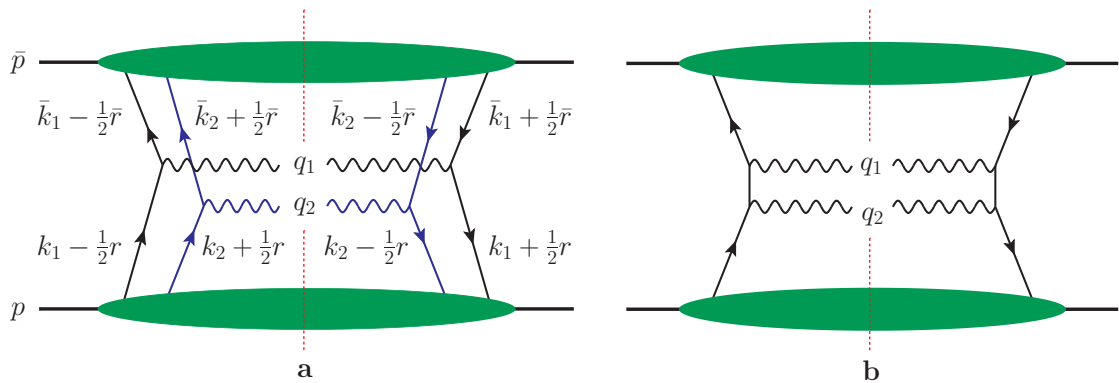

Fig. 27. Graphs for the production of two gauge bosons by double (a) or single (b) hard scattering. The dotted line denotes the final-state cut.

where we have introduced light-cone coordinates $v^{\pm} = (v^0 \pm v^3)/\sqrt{2}$ for each four-vector v. The definition of the double-parton distributions in (11) closely resembles the one for a transverse-momentum dependent single-quark distribution [87,88,89,90]. For instance, the distribution of two quarks in the proton with momentum p is given by

$$F_{a_1,a_2}(x_i, \boldsymbol{k}_i, \boldsymbol{y}) = \left[\prod_{i=1}^{2} \int \frac{dz_i^- \, d^2\boldsymbol{z}_i}{(2\pi)^3} \, e^{i(x_i z_i^- \, p^+ - \boldsymbol{z}_i \boldsymbol{k}_i)} \right] 2p^+ \int dy^-$$

$$\times \left. \left\langle p \middle| \bar{q}(-\tfrac{1}{2}z_2)\, \varGamma_{a_2}\, q(\tfrac{1}{2}z_2)\, \bar{q}(y - \tfrac{1}{2}z_1)\, \varGamma_{a_1}\, q(y + \tfrac{1}{2}z_1) \middle| p \right\rangle \right|_{z_1^+ = z_2^+ = y^+ = 0}. \tag{13}$$

One can identify $\boldsymbol{k}_i$ as the "average" transverse momentum of each quark and $\boldsymbol{y}$ as the "average" transverse distance between the quarks, where the "average" refers to the physical scattering amplitude and its conjugate. The result (11) thus has an intuitive interpretation: two bosons with transverse momenta $\boldsymbol{q}_i$ are produced in the collision of partons with average transverse momenta $\boldsymbol{k}_i$ and $\bar{\boldsymbol{k}}_i$. The two collisions occur at an average transverse distance $\boldsymbol{y}$, which is equal to the average transverse distance between the two partons in each colliding proton. At a more formal level, $F(x_i, \boldsymbol{k}_i, \boldsymbol{y})$ has the structure of a Wigner distribution [91] in its transverse momentum and position arguments.

Integrating over the transverse parton momenta, one obtains a collinear two-parton distribution $F_{a_1,a_2}(x_i, \boldsymbol{y}) = \int d^2\boldsymbol{k}_1 \, d^2\boldsymbol{k}_2 \; F_{a_1,a_2}(x_i, \boldsymbol{k}_i, \boldsymbol{y})$, which can be interpreted as the probability for finding two quarks with momentum fractions x_1 and x_2 at a relative transverse distance $\boldsymbol{y}$ in the proton. These distributions naturally appear if one integrates the cross section (11) over the transverse momenta $\boldsymbol{q}_1$ and $\boldsymbol{q}_2$ of the bosons,

$$\frac{d\sigma}{\prod_{i=1}^{2} dx_i \, d\bar{x}_i} \bigg|_{\text{Fig. 27a}} = \frac{1}{S} \sum_{\substack{a_1, a_2 = q, \Delta q, \delta q \\ \bar{a}_1, \bar{a}_2 = \bar{q}, \Delta\bar{q}, \delta\bar{q}}} \hat{\sigma}_{1, a_1 \bar{a}_1}(q_1^2) \, \hat{\sigma}_{2, a_2 \bar{a}_2}(q_2^2)$$

$$\times \int d^2\boldsymbol{y} \; F_{a_1, a_2}(x_i, \boldsymbol{y}) \, F_{\bar{a}_1, \bar{a}_2}(\bar{x}_i, \boldsymbol{y}). \tag{14}$$

This is the simple cross section formula mentioned in the introduction. It was already derived in [47,92] and underlies most phenomenological studies of multiparton interactions. Note that (14) and its generalization (11) to measured transverse momenta have an intuitive physical interpretation, but that they arise from the calculation of lowest-order Feynman graphs as in figure 27a, using standard approximations. One does not need to appeal to semi-classical arguments to obtain these results.

For each bilinear operator in the matrix element (13) there are three relevant Dirac matrices $\varGamma_{a_i}$,

$$\varGamma_q = \tfrac{1}{2}\gamma^+, \qquad\qquad \varGamma_{\Delta q} = \tfrac{1}{2}\gamma^+\gamma_5, \qquad\qquad \varGamma_{\delta q}^j = \tfrac{1}{2}i\sigma^{j+}\gamma_5 \quad \text{with } j = 1, 2, \tag{15}$$

which respectively project on unpolarized, longitudinally polarized and transversely polarized quarks. Note that polarized two-parton distributions exist even in an unpolarized proton, where they describe spin correlations *between* the two partons. For small but comparable x_1 and x_2 one may well have sizeable spin correlations between two quarks (which are close in phase space for $x_1 \sim x_2$), even if there is little correlation between the polarizations of a quark and the proton (which are far apart in phase space). The relevance of such correlations in multiple interactions was pointed out already in [92] but has to our knowledge not been included in phenomenology.

If parton spin correlations are sizeable, they can have a strong impact on observables. For the production of two gauge bosons one can easily see that the product $F_{\Delta q, \Delta q} \, F_{\Delta \bar{q}, \Delta \bar{q}}$ of longitudinal spin correlations enters the cross section with the same weight as the unpolarized term $F_{q,q} \, F_{\bar{q}, \bar{q}}$. One also finds that product $F_{\delta q, \delta q} \, F_{\delta \bar{q}, \delta \bar{q}}$ of transverse spin correlations give rise to a $\cos(2\varphi)$ modulation in the angle φ between the decay planes of the two bosons and thus affects the distribution of final-state particles.

4.1.2 Power behavior

It is easy to determine the power behavior of the cross section formula (11) for double hard scattering. The parton-level cross sections $\hat{\sigma}$ behave like $1/Q^2$, where $Q^2 \sim q_1^2 \sim q_2^2$ denotes the size of the large squared invariant masses of the gauge bosons. We find

$$\frac{d\sigma}{\prod_{i=1}^{2} dx_i \, d\bar{x}_i \, d^2\boldsymbol{q}_i} \bigg|_{\text{Fig. 27a}} \sim \frac{1}{Q^4 \varLambda^2}, \tag{16}$$

where $\varLambda$ denotes the size of the transverse momenta $\boldsymbol{q}_1 \sim \boldsymbol{q}_2$ or the scale of non-perturbative interactions, whichever is larger. To obtain (16), we have used that the two-parton distributions scale like $F \sim 1/\varLambda^2$ and that the typical
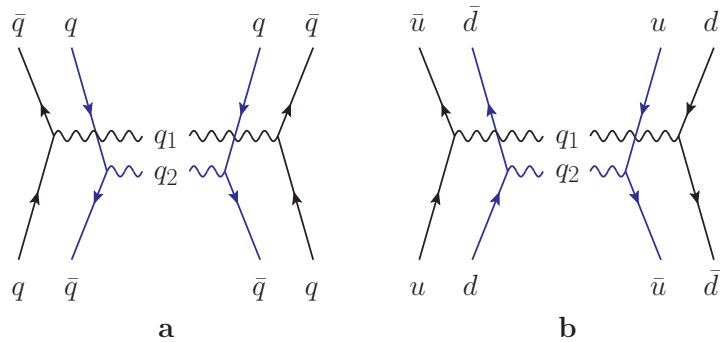
Fig. 28. Example graphs for interference terms in fermion number (a) and in quark flavor (b). The blobs indicating two-parton distributions are not shown. Labels q and $\bar{q}$ indicate whether a line is represented by a quark or a conjugate quark field in the operator definition. Momenta are assigned as in figure 27.

transverse distance $\boldsymbol{y}$ between the partons is of order $1/\Lambda$. The same power behavior as in (16) is obtained for the case where both bosons are produced in a single hard scattering, as shown in figure 27b. Multiple hard interactions are therefore *not* power suppressed as long as one keeps the cross section differential in the transverse momenta of the particles produced in the hard parton collisions.

The situation changes when one integrates over $\boldsymbol{q}_1$ and $\boldsymbol{q}_2$. In the double-scattering mechanism both transverse momenta are restricted to size Λ, but for a single hard scattering one has $|\boldsymbol{q}_1 + \boldsymbol{q}_2| \sim \Lambda$ whereas the individual transverse momenta can be as large as Q. Because of this phase space effect one has

$$\frac{d\sigma}{\prod_{i=1}^{2} dx_i \, d\bar{x}_i} \bigg|_{\text{Fig. 27a}} \sim \frac{\Lambda^2}{Q^4} \, , \qquad\qquad \frac{d\sigma}{\prod_{i=1}^{2} dx_i \, d\bar{x}_i} \bigg|_{\text{Fig. 27b}} \sim \frac{1}{Q^2} \, . \qquad (17)$$

In the transverse-momentum integrated cross section, multiple hard scattering is therefore a power correction. This is required for the validity of the usual factorization formulae, which contain only the single-scattering contribution.

4.1.3 Additional terms in the cross section

In the formulae given so far, we have ignored the color structure of the multiparton distributions. The quark lines with momentum fraction x_1 in figure 27a can couple to a color singlet (as in single-parton distributions) but they can also couple to a color octet, provided that the lines with momentum fraction x_2 are coupled to a color-octet as well. In the latter case, the color structure of the operators in (13) is $(\bar{q} \, \Gamma_{a_2} \lambda^a q) \, (\bar{q} \, \Gamma_{a_1} \lambda^a q)$. Such color-octet distributions contribute to the multiple-scattering cross section, as was already pointed out in [76]. They do not have a probability interpretation, and little is known about them. The color structure of two-gluon distributions is even more involved.

There are more multiparton distributions that have no probability interpretation but rather the structure of interference terms. As shown in figure 28a, the parton with momentum fraction x_1 can be a quark in the scattering amplitude but an antiquark in the conjugate amplitude, provided that the opposite holds for the parton with momentum fraction x_2. Furthermore, one can have interference in the quark flavor, as shown in figure 28b.

While it is quite straightforward to include these extra contributions in the cross section formula, the additional number of two-parton distributions needed to obtain quantitative results is daunting. It is therefore important to have some guidance about the size and behavior of these functions.

4.1.4 High transverse momentum and evolution

The predictive power of the theory is increased in the kinematic region where the transverse momenta $\boldsymbol{q}_i$ are small compared with Q but large compared with a typical non-perturbative scale. At least some of the transverse parton momenta must then be large as well, and one can evaluate the corresponding parton distributions in terms of a hard scattering subprocess at scale $|\boldsymbol{q}_i|$ and parton distributions that depend on fewer variables.

An important example for this are ladder graphs such as the one in figure 29a. Since the partons with momentum fraction x_1 are not connected to those with momentum fraction x_2, the momentum mismatch $\boldsymbol{r}$ is small. In position space this corresponds to an inter-parton distance $\boldsymbol{y}$ of hadronic size. An important feature of these ladder graphs is that their color factors disfavor the color octet distributions mentioned in the previous section. How strong this suppression is quantitatively remains to be studied.
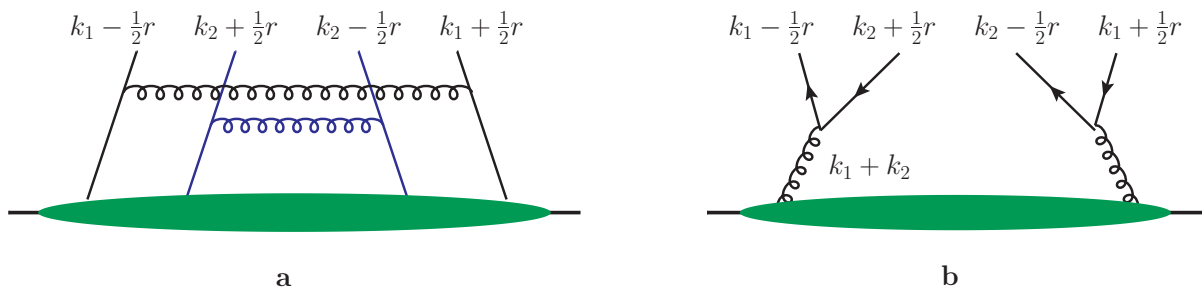
Fig. 29. (a) Ladder graph for a two-parton distribution, which generates perturbatively large $\boldsymbol{k}_1$ and $\boldsymbol{k}_2$ at small $\boldsymbol{r}$. (b) Graph for a quark-antiquark distribution, where the partons with momentum fractions x_1 and x_2 originate from the splitting of a single gluon.
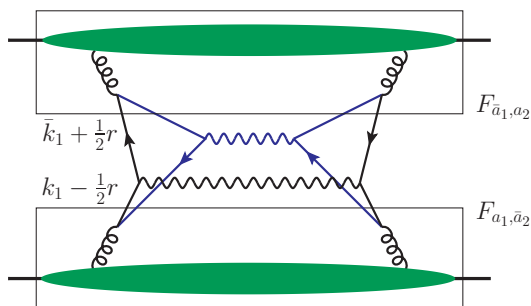

Fig. 30. Graph for the cross section where both two-parton distributions $F_{a_1,\bar{a}_2}$ and $F_{\bar{a}_1,a_2}$ (indicated by boxes) involve the splitting of one into two partons.

In the graph of figure 29b, the two partons with momentum fractions x_1 and x_2 originate from the splitting of a single parton. Such graphs are relevant for the region of large $\boldsymbol{r}$, i.e. of short distance $\boldsymbol{y}$, and also for large $\boldsymbol{k}_1 - \boldsymbol{k}_2$. One finds that they generate strong spin correlations between the partons; the graph in the figure for instance forces the helicities of the quark and antiquark to add up to zero.

Both graphs in figure 29 lead to divergent integrals if one integrates over $\boldsymbol{k}_1$ and $\boldsymbol{k}_2$ at fixed $\boldsymbol{r}$. Proper regularization of these divergences gives the evolution equation for collinear two-parton distributions; in particular splitting graphs as in figure 29b give the famous inhomogeneous term in this equation [93,94]. Remarkably, one finds however that *no* such inhomogeneous term appears in the evolution of the distributions $F(x_i, \boldsymbol{y})$ at any finite value of $\boldsymbol{y}$, provided one uses the definition (13) with minimal subtraction of divergences.

The splitting mechanism of figure 29b is responsible for a behavior $F(x_i, \boldsymbol{y}) \sim 1/\boldsymbol{y}^2$ at short distances $\boldsymbol{y}$, which renders the integral in the cross section (14) infinite. The same mechanism already gives divergent integrals in the differential cross section (11). Furthermore, there is a double counting problem associated with this splitting contribution: the graph in figure 30 describes double hard scattering with a $1 \to 2$ parton splitting in each proton, but it also represents a single hard-scattering mechanism, namely two-gluon fusion $gg \to VV$ into two bosons via a box graph. Therefore, either the cross section formulae (11) and (14), or the definition (13) of two-parton distributions, or both must be modified in a way that removes singularities at small $\boldsymbol{y}$, and a corresponding prescription for calculating $gg \to VV$ must be given to avoid double counting. This remains a task for future work. More details on the topics and results discussed here can be found in [95].

4.2 The four jet production at LHC and Tevatron in QCD
Contributing authors: B. Blok, Yu. Dokshitzer, L. Frankfurt and M. Strikman

In spite of an extensive theoretical and experimental work, various aspects of the high energy hadronic collisions at Tevatron and LHC are still poorly understood. This is especially true for the multijet production which is of a paramount importance for the understanding of pQCD dynamics at high energy colliders, and for the search of new particles. Here we summarize the first steps of the program to address the topic of MPI starting from the first principles of the perturbative QCD which is necessary for an accurate account of the significant disbalance of the momenta of the jets (presence of the Sudakov form factors). Among original results presented here are the derivation of the formulae in the leading logarithmic approximation for production of 4 jets. Our key finding is that it is possible to isolate the

kinematics where the leading twist processes $2 \to 4$ are not enhanced. This result will allow to improve the reliability of the Tevatron studies of the four jet production in the multiparton kinematics and point out directions for the corresponding analysis at the LHC.

Another critical issue is the formulation of the problem in terms of the momentum representation double generalized parton distributions and introduction of the mean field approximation for this object. This new formulation is very effective for the more detailed studies which are now under way. In addition it brings a link with the original formulation in the coordinate space [96, 92, 97, 98, 99, 100, 101, 102, 103, 104, 105, 106, 107], and resolves an issue of the value of the strength of the double interaction within this approximation. Previously there was a question whether a conclusion of ref. [102, 103], that the observed rate is a factor of two larger than the theoretical prediction can be due to uncertainties related to many Fourier transforms which were required to convert the HERA data to the experimental number. A new formulation, though mathematically equivalent, has completely resolved this issue. This poses serious constraints on the Monte Carlo models of pp scattering at collider energies which are not satisfied by many of the current models.

These issues are of broad interest for both the theorists and experimentalists.

The standard approach to the multijet production is the QCD improved parton model. It is based on the assumption that the cross section of a hard hadron–hadron interaction is calculable in terms of the convolution of parton distributions within colliding hadrons with the cross section of a hard two-parton collision. An application of this approach to the processes with production of four jets implies that all jets in the event are produced in a hard collision of *two* initial state partons.

The recent data due to CDF and D0 collaborations [3, 4] do not contradict the dominance of this mechanism in the well defined part of the phase space. At the same time these data provide the evidence that there exists a kinematical domain where a more complicated mechanism becomes important, namely the double hard interaction of two partons in one hadron with two partons in the second hadron.

Within the parton model picture, the four jets produced this way should pair into two groups such that the transverse momenta of two jets in each pair compensate each other. In what follows we refer to this kinematics as *back-to-back dijet production*. We consider the dijets for the case

$$\delta_{13}^2 \equiv (\boldsymbol{j}_{1t} + \boldsymbol{j}_{3t})^2 \ll j_{1t}^2 \simeq j_{3t}^2, \quad \delta_{24}^2 \ll j_{2t}^2 \simeq j_{4t}^2, \tag{18}$$

where δ is the total transverse momentum of the dijet and j_{it} the transverse momentum of an individual jet (see Fig. 31). The hardness condition $\delta^2 \gg R^{-2}$ is implied, with R the characteristic hadron size (non-perturbative scale). (The events with disbalances $\delta^2 \le R^{-2}$, give a small contribution both to total and differential cross sections, since they are suppressed by Sudakov form factors. (for a detailed detailed discussion of the issue in the review [108] . Evidently this nonperturbative contribution is not enhanced in the Leading Logarithmic Approximation).

Importantly, in this kinematical region the hard scattering of four partons from the wave functions of the colliding hadrons remains the dominant source for four-jet production even when the pQCD parton multiplication phenomena are taken into account.

The reason for that is the following. When the two partons from each hadron emerge from the *initial state parton cascades* and then engage into double hard scattering, the resulting differential distribution of the final state jets lacks the double back-to-back enhancement factor $d\sigma \propto \delta_{13}^{-2}\delta_{24}^{-2}$ which is there in the case of two independent hard scatterings. For the two-parton scattering, the characteristic perturbative enhancement $d\sigma \propto \delta^{-2}$ results from a coherent enhancement of the amplitude due to integration over a large transverse disk, $\rho^2 \sim \delta^{-2} \gg j_t^{-2}$. The two partons that originate from a perturbative splitting form a relatively compact system in the impact parameter space, so that the double hard interaction of such pairs produces only a single perturbative enhancement factor, $(\boldsymbol{\delta}_{13}+\boldsymbol{\delta}_{24})^{-2}$, which does not favor the back-to-back dijet kinematics (18). The distribution of four jets so produced is much more isotropic and can be suppressed by choosing proper kinematical cuts.

So, the aim of this section is to consider the four-jet production in the hard collisions of *four* initial state partons. We show that the cross section of back-to-back dijet production is calculable in terms of new nonperturbative objects — the double-parton Generalized Parton Distributions (DPGPDs). The properties of the DPGPDs can be rigorously studied within QCD. In particular, we report here the derivation of the geometric picture for multiple parton collisions in the impact parameter space. Up till now, this picture was being used based on a semi-intuitive reasoning [96, 92, 97, 98, 99, 100, 101, 102, 103, 104, 105, 106, 107].

In the kinematical domain (18) the direct calculation of the light cone Feynman diagrams (momenta of the partons in the initial and final states are shown in Fig. 31) using the separation of hard and soft scales shows that the four $\to$ four cross section for the collisions of hadrons "a" and "b" has the form:

$$\sigma_4 = \int \frac{d^2\overrightarrow{\Delta}}{(2\pi)^2} \int dx_1 \int dx_2 \int dx_3 \int dx_4$$

$$\times D_a(x_1, x_2, p_1^2, p_2^2, \overrightarrow{\Delta}) D_b(x_3, x_4, p_1^2, p_2^2, -\overrightarrow{\Delta})$$
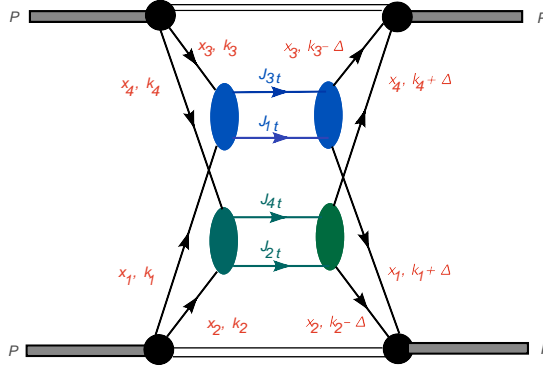
Fig. 31. Kinematics of double hard collision - momenta of the colliding partons in in and out states

$$\times \; \frac{d\sigma^{13}}{d\hat{t}_1} \frac{d\sigma^{24}}{d\hat{t}_2} d\hat{t}_1 d\hat{t}_2. \tag{19}$$

Here $D_\alpha(x_1, x_2, p_1^2, p_2^2, \overrightarrow{\Delta})$ are the new DPGPDs for hadrons "a" and "b" defined below. (In the following we will consider the case of pp collisions and omit the subscript α. Summing over collisions of various types of partons is implied. In practice however we will keep hard scattering of gluons only since it gives the dominant contribution.). Remember that the light cone fractions x_i are actually fixed by final jet parameters and energy momentum constraints.

With account of the radiative pQCD effects, in full analogy with the "DDT formula" for two-body collisions, the differential distribution (19) acquires Sudakov form factors [108,109] depending on the logarithms of the large ratios of scales, j_t^2/δ^2, and the GPDs become scale dependent: $p_1^2 \sim \delta_{13}^2$, $p_2^2 \sim \delta_{24}^2$. It should be mentioned that the structure of the final formula depends on what one actually measures in the experiment — whether energetic single particles with large transverse momenta in the final state or "jets" — and on how the jets are precisely defined. A more detailed account of the pQCD effects will be given in a future publication.

For brevity we will not write explicitly the virtuality scales of the DPGPDs and will use the form: $D(x_1, x_2, \overrightarrow{\Delta})$. Note that these distributions depend on the new transverse vector $\overrightarrow{\Delta}$ that is equal to the difference of the momenta of partons from the wave function of the colliding hadron in the amplitude and the amplitude conjugated. Such dependence arises because the difference of parton transverse momenta within the parton pair is not conserved. The integration limits in $x_i, \hat{t}$ are subject to standard limits determined by kinematic cuts.

Within the parton model approximation the cross section has the form:

$$\sigma_4 = \sigma_1 \sigma_2 / \pi R_{\text{int}}^2, \tag{20}$$

where σ_1 and σ_2 are the cross sections of two independent hard binary parton interactions. The factor πR_{int}^2 characterizes the transverse area occupied by the partons participating in the hard collision. (In the experimental [3,4] and some of the theoretical papers this factor was denoted as an effective cross section. Our Eq. 21 below shows that such wording is not satisfactory since πR_{int}^2 does not have the meaning of the interaction cross section.) The data [3,4] indicates that πR_{int}^2 is practically constant in the kinematical range studied at the Tevatron.

Eq. 19 leads to the general model independent expression for

$$\frac{1}{\pi R_{\text{int}}^2} = \int \frac{d^2 \overrightarrow{\Delta}}{(2\pi)^2} \frac{D(x_1, x_2, -\overrightarrow{\Delta}) D(x_1, x_2, \overrightarrow{\Delta})}{D(x_1) D(x_2) D(x_3) D(x_4)}, \tag{21}$$

in terms of DPGPDs. Here $D(x_i)$ are the corresponding structure functions.

The DPGPDs are expressed through the light cone wave functions of the colliding hadrons as follows. Suppose that in a four $\rightarrow$ four process the two partons in the nucleon in the initial state wave function have the transverse momenta $\overrightarrow{k_1}, \overrightarrow{k_2}$. Then in the conjugated wave function they will have the momenta $\overrightarrow{k_1} + \overrightarrow{\Delta}, \overrightarrow{k_2} - \overrightarrow{\Delta}$. This is because only sum of parton transverse momenta but not the difference is conserved.

The relevant DPGPDs are:

$$D\left(x_1, x_2, p_1^2, p_2^2, \overrightarrow{\Delta}\right) = \sum_{n=3}^{\infty} \int \frac{d^2 k_1}{(2\pi)^2} \frac{d^2 k_2}{(2\pi)^2} \theta(p_1^2 - k_1^2)$$

$$\times \, \theta(p_2^2 - k_2^2) \int \prod_{i \neq 1,2} \frac{d^2 k_i}{(2\pi)^2} \int_0^1 \prod_{i \neq 1,2} dx_i$$

$$\times \ (\psi_n(x_1, \boldsymbol{k}_1, x_2, \boldsymbol{k}_2, ., \boldsymbol{k}_i, x_i..)$$

$$\times \ \psi_n^+(x_1, \overrightarrow{k_1} + \overrightarrow{\Delta}, x_2, \overrightarrow{k_2} - \overrightarrow{\Delta}, x_3, \boldsymbol{k}_3, ...) + h.c.)$$

$$\times \ (2\pi)^3 \delta(\sum_{i=1}^{i=n} x_i - 1)\delta(\sum_{i=1}^{i=n} \boldsymbol{k}_i). \tag{22}$$

Note that this distribution is diagonal in the space of all partons except the two partons involved in the collision. Here ψ is the parton wave function normalized to one in a usual way. An appropriate summation over color and Lorentz indices is implied. In the case of kinematics $1 \gg x_1 \geq x_2$ we expect only distributions without the spin flip to be important.

Let us stress that it follows from the above formulae that in the impact parameter space these GPDs have a probabilistic interpretation. In particular these DPGPD are positively definite in the impact parameter space, cf. Eq. 28. Note that in the same way one can introduce the N-particle GPD, G_N, which can be probed in the production of N pairs of jets. In this case the first N arguments k_i in Eq. 22 are shifted by $\overrightarrow{\Delta_i}$ subject to the constraint $\sum_i \overrightarrow{\Delta_i} = 0$. So the cross section is proportional to

$$\sigma_{2N} \propto \int \prod_{i=1}^{i=N} \frac{d\overrightarrow{\Delta_i}}{(2\pi)^2} D_a(\overrightarrow{\Delta}_1, ...\overrightarrow{\Delta}_N)$$

$$\times \ D_b(\overrightarrow{\Delta}_1, ...\overrightarrow{\Delta}_N)\delta(\sum_{i=1}^{i=N} \overrightarrow{\Delta}_i). \tag{23}$$

These GPDs can be easily rewritten in the form of the matrix elements of the operator product. For example:

$$D(\Delta) = < N| \int d^4x_1 d^4x_2 d^4x_3$$

$$\times \ G_{i+}^a(x_1)G_{j+}^b(x_2)G_{i+}^a(x_3)G_{j+}^b(x_4)$$

$$\times \ \exp(ip_1^+(x_1 - x_3)^- + ip_2^+(x_2 - x_4)^-$$

$$+ \ i\boldsymbol{\Delta}_t(\boldsymbol{x}_4 - \boldsymbol{x}_3)_t)|N>, \tag{24}$$

calculated at the virtualities p_1^2, p_2^2 at fixed $\overrightarrow{\Delta}$. Here we gave an example for the most relevant case of gluons without a flip in color and spin spaces. In general a number of distributions can be written, depending on different contractions of transverse Lorentz indices and color indices. The classification of the relevant distributions is the same as the classification of the quasipartonic operators in ref. [110]. Note that the presence of the transverse external parameter $\boldsymbol{\Delta}$ does not change the classification, since the corresponding new structures will be strongly suppressed at high energies. we wrote the operator expression in the light cone gauge. In arbitrary gauge we shall need Wilson loop W(C) connecting points with contracted color indices

In the approximation of uncorrelated partons it follows from Eq. 22 that

$$D(x_1, x_2, p_1^2, p_2^2, \boldsymbol{\Delta}) = G(x_1, p_1^2, \boldsymbol{\Delta})G(x_2, p_2^2, \boldsymbol{\Delta}), \tag{25}$$

where $G(x, \overrightarrow{\Delta})$ are conventional one-particle GPDs. These GPDs can be approximated as $G_N(x, Q^2, \boldsymbol{\Delta}) = G_N(x, Q^2)F_{2g}(\Delta)$, where $F_{2g}(\Delta)$ is the two-gluon form factor of the nucleon extracted from hard exclusive vector meson production (we suppress here the dependence of F_{2g} on x) [111] and $G_N(x, Q^2)$ conventional parton distribution of a nucleon. (Here Q^2 is the virtuality due to the radiation, cf. discussion after Eq. 19.) Thus :

$$\frac{1}{\pi R_{\text{int}}^2} = \int \frac{d^2\Delta}{(2\pi)^2} F_{2g}^4(\Delta) = \frac{m_g^2}{28\pi}. \tag{26}$$

Here at the last step we used the dipole fit $F_{2g}(\Delta) = 1/(\Delta^2/m_g^2 + 1)^2$ to the two-gluon form factor. Using the transverse gluon radius of the nucleon we obtain

$$R_{\text{int}}^2 = 7/2r_g^2, \qquad r_g^2/4 = dF_{2g}(t)/dt_{t=0}. \tag{27}$$

This result coincides with the one for the area πR_{int}^2 obtained earlier in [102,103] using the geometric picture in the impact parameter space. That derivation involved taking Fourier transform of the two-gluon form factor and calculating a rather complicated six-dimensional integral which could potentially lead to large numerical uncertainties. The form of Eq. 27 clearly indicates that numerical uncertainties are small.

It was emphasized in [102,103] that the experiments on four-jet production report a smaller value of πR_{int}^2 as compared to the one obtained above in the independent particle approximation (though the issue of how well the contribution of the $2 \to 4$ processes was subtracted still remains, cf. discussion in the beginning of this section). It is at least a factor of two smaller — that is a four-jet cross section is a factor of two larger — than Eq. 27 gives. (The GPDs for sea quarks appear to decrease with Δ somewhat faster, resulting in a smaller $1/\pi R_{int}^2$, see discussion in [112].)

It follows from Eq. 21 that the value of R_{int}^2 is determined by the range of integration over Δ. Hence the characteristic Δ in the integral measures the effective distance between the parton pairs (which in principle may differ for different flavor combinations). According to the above evaluation within the independent parton approximation the integral for $1/R_{\text{int}}^2$ is dominated by small $\Delta^2 \sim 0.1\, m_g^2$. The contribution of large Δ is suppressed by the two-gluon form factor of a nucleon. This reasoning indicates the important role of inter-parton correlations. In other words, the integral over Δ is effectively cut off by a scale of the nonperturbative correlations. Such correlations naturally arise in nonperturbative QCD regime in a number of nucleon models, such as constituent quark model (gluon cloud around constituent quark) [102,103], or string model (gluon structure of string). The detailed analysis of the additional correlations due to the hard– soft interplay will be reported elsewhere.

Let us now show that results presented here lead to the intuitive geometric picture in the impact parameter space mentioned above [96,92,97,98,99,100,101,102,103,104,105,106,107].

The first step is to make transformation into coordinate space i.e., to make Fourier transform from variables k_i in Eq. 22 to coordinates b_i. Performing integration over k_i we obtain that transverse coordinates of partons in the amplitude and the amplitude conjugated are equal $\rho_i = \rho_f$. In the calculation we use the fact that upper limit of integration over k_t^2 is very large compared with the inverse hadron size. Next step is to perform integration over Δ which produces $\delta(\boldsymbol{\rho}_1 - \boldsymbol{\rho}_2 - \boldsymbol{\rho}_3 + \boldsymbol{\rho}_4) = \int d^2 B \delta(\boldsymbol{\rho}_1 - \boldsymbol{\rho}_3 - \boldsymbol{B})\delta(\boldsymbol{\rho}_2 - \boldsymbol{\rho}_4 - \boldsymbol{B})$.

The delta functions express the fact that within the accuracy $1/p_t$ where p_t is the hard scale, the interactions of partons from different nucleons occur at the same point. $\boldsymbol{B}$ is the relative impact parameter of two nucleons.

The expression for the cross section in the impact parameter space has the form which corresponds to geometry of Fig.32

$$\sigma_4 = \int d^2 B d^2 \rho_1 d^2 \rho_2 d^2 \rho_3 d^2 \rho_4 D(x_1, x_2, \boldsymbol{\rho}_1, \boldsymbol{\rho}_2)$$

$$\times\, D(x_3, x_4, \boldsymbol{\rho}_3, \boldsymbol{\rho}_4)\delta(\boldsymbol{b}_1 + (\boldsymbol{B} - \boldsymbol{b}_3))\delta(\boldsymbol{b}_2 + (\boldsymbol{B} - \boldsymbol{b}_4)) =$$

$$= \int d^2 B d^2 \rho_1 d^2 \rho_2 D(x_1, x_2, \boldsymbol{\rho}_1, \boldsymbol{\rho}_2)$$

$$\times\, D(x_3, x_4, -\boldsymbol{B} + \boldsymbol{\rho}_1, -\boldsymbol{B} + \boldsymbol{\rho}_2). \tag{28}$$

Here the DPGPD in the impact parameter space representation is given by

$$D\left(x_1, x_2, \boldsymbol{\rho}_1, \boldsymbol{\rho}_2\right) =$$

$$= \sum_{n=3}^{n=\infty} \int \prod_{i \geq 3}^{i=n} \left[dx_i d^2 \rho_i\right] \psi_n(x_1, \boldsymbol{\rho}_1, x_2, \boldsymbol{\rho}_2, ...x_i, \boldsymbol{\rho}_i,)$$

$$\times\, \psi_n^+(x_1, \boldsymbol{\rho}_1, x_2, \boldsymbol{\rho}_2, ..., x_i, \boldsymbol{\rho}_i, ...)\delta(\sum_{i=1}^{i=n} x_i \boldsymbol{\rho}_i). \tag{29}$$

where the delta function expresses the center of mass constraint $\sum_{i=1}^{i=n} x_i \boldsymbol{\rho}_i = 0$. This is analogous to the case of single parton GPDs, see [113,114]. The functions $\psi(x_1, \boldsymbol{\rho}_1, x_2, \boldsymbol{\rho}_2, ...)$ are just the Fourier transforms in the impact parameter

space of the light cone wave functions and are given by

$$\psi_n \left(x_1, \boldsymbol{\rho}_1, x_2, \boldsymbol{\rho}_2, ... \right) = \int \prod_{i=1}^{i=n} \frac{d^2 k_i}{(2\pi)^2} \exp(i \sum_{i=1}^{i=n} \boldsymbol{k}_i \boldsymbol{\rho}_i)$$

$$\times \ \psi_n(x_1, \boldsymbol{k}_1, x_2, \boldsymbol{k}_2, ..)(2\pi)^2 \delta(\sum \boldsymbol{k}_i). \tag{30}$$
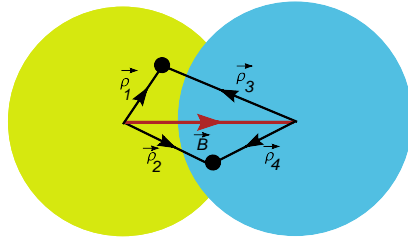

Fig. 32. Geometry of two hard collisions in impact parameter picture.

Thus the GPD defined in Eq. 22 is equivalent to the representation for cross section that indeed corresponds to the simple geometrical picture, but instead of a triple integral we now have an integral over one momentum Δ. Moreover, to determinate the cross section we need to know the $D(\Delta)$. The GPD defined in Eq. 22 is useful for calculation of many different processes. At the same time the knowledge of the full double GPD is necessary for complete description of events with a double jet trigger since the pedestal strongly depends on the impact parameter $\boldsymbol{B}$ [102,103].

Let us stress that this picture is a natural generalization of the correspondence between momentum representation and geometric picture for a conventional case of two $\rightarrow$ two collisions. Indeed in this case it is easy to see that the cross section in the momentum representation

$$\sigma_2 = \int f(x_1, p^2) f(x_2, p^2) \frac{d\sigma^h}{d\hat{t}} d\hat{t} \tag{31}$$

has a simple geometric representation

$$\sigma_2 = \int d^2 \rho_1 d^2 B f(x_1, \boldsymbol{\rho}_1, p^2) f(x_2, \boldsymbol{B} - \boldsymbol{\rho}_1, p^2) \frac{d\sigma^h}{d\hat{t}} d\hat{t}, \tag{32}$$

where $f(x, \boldsymbol{\rho}, p^2) = \psi^+(x, \boldsymbol{\rho}, p^2)\psi(x, \boldsymbol{\rho}, p^2)$ and $\psi(\boldsymbol{\rho}, p^2)$ is the Fourier transform of the light cone wave function defined above.

Let us now summarize our results. We have argued that there exists the kinematical domain where the four $\rightarrow$ four hard parton collisions form the dominant mechanism of four-jet production. In this region we calculated the cross section, see Eqs. 19-21 and found that it can be expressed through new two particle GPDs (see Eq. 22), expressed through light cone wave functions. These GPDs depend on a transverse vector $\boldsymbol{\Delta}$ that measures the transverse distance within the parton pairs. (Equivalent expressions for these GPDs can be easily given in terms of the operator products.) In the impact parameter space we derived the widely used intuitive geometric picture. We argued that the enhancement of a four-jet cross section is due to short range correlations in the hadron, as determined by the range of integral of Δ. The contribution of perturbative correlations in the appropriate kinematic domain is suppressed. The detailed study of the interplay of the contribution of hard/soft correlations will be reported elsewhere.

It was argued recently [82,115], cf. 4.3, that the cross section can be expressed in terms of two parton distribution functions. Our analysis indicates that a more detailed treatment of the QCD evolution effects is necessary. We found that it is necessary to introduce the new 2-particle DPGPDs which depend on additional parameter Δ. The parameter Δ expresses the fact that the difference in transverse components of the parton momenta is not conserved and therefore different in $|in\rangle$ and $\langle out|$ states in the double hard collisions.

4.3 Double parton distribution functions

Contributing author: J. R. Gaunt, W. J. Stirling

If we make only the assumption that the hard processes A and B may be factorised, then we may write the cross section for DPS in very general terms as follows:

$$\sigma_{(A,B)}^D = \frac{m}{2} \sum_{i,j,k,l} \int \Gamma_{ij}(x_1, x_2, \boldsymbol{b}; Q_A, Q_B) \hat{\sigma}_{ik}^A(x_1, x_1') \hat{\sigma}_{jl}^B(x_2, x_2') \tag{33}$$

$$\times \Gamma_{kl}(x_1', x_2', \boldsymbol{b}; Q_A, Q_B) dx_1 dx_2 dx_1' dx_2' d^2 \boldsymbol{b}$$

The structure of the DPS cross section formula is similar to that for single parton scattering (SPS), in the sense that it too is expressed in terms of parton level cross sections $\hat{\sigma}$ multiplied by parton distributions Γ. However, whilst the parton level cross sections used in (33) are the same as those used for SPS, the parton distributions of (33) are significantly more complex than the single PDFs. They are the generalised two-parton PDFs (or, using the language of [116]and Section 4.2, the two-parton GPDs). The quantity $\Gamma_{ij}(x_1, x_2, b; Q_A, Q_B)$ can be interpreted as the probability to find a pair of partons in the proton which have flavours i and j, longitudinal momenta x_1 and x_2, and are separated in impact parameter by $\boldsymbol{b}$, when the partons are probed at scales Q_A and Q_B respectively. m is a symmetry factor that equals 1 if $A = B$ and 2 otherwise.

Two further assumptions are often applied to (33). First, it is assumed that the two-parton GPD may be decomposed into a (typically flavour independent) transverse piece, and a longitudinal piece:

$$\Gamma_{ij}(x_1, x_2, \boldsymbol{b}; Q_A, Q_B) \simeq F(\boldsymbol{b}) D_p^{ij}(x_1, x_2; Q_A, Q_B) \tag{34}$$

In this case the DPS cross section reduces to:

$$\sigma_{(A,B)}^{DPS} = \frac{m}{2\sigma_{\text{eff}}} \sum_{i,j,k,l} \int dx_1 dx_2 dx_1' dx_2' \ D_p^{ij}(x_1, x_2; Q_A, Q_B) \ D_p^{kl}(x_1', x_2'; Q_A, Q_B) \tag{35}$$

$$\times \hat{\sigma}_{ik}^A(x_1, x_1') \hat{\sigma}_{jl}^B(x_2, x_2')$$

with σ_{eff} a constant. Second, it is assumed that $D_p^{ij}(x_1, x_2; Q_A, Q_B)$ may be written as a product of single PDFs (sPDFs):

$$D_p^{ij}(x_1, x_2; Q_A, Q_B) \simeq D_p^i(x_1; Q_A) D_p^j(x_2; Q_B) \tag{36}$$

The analysis of $\gamma + 3$ jet events performed by the CDF collaboration [3] indicates that (36) approximately holds for sea partons at moderately low x. However, it is clear even from elementary considerations that this assumption must be violated on some level - for example, the left hand side of (36) must go to zero at the kinematic bound $x_1 + x_2 = 1$ whilst the product of sPDFs is finite along this line. One might ask as to whether theory can make any predictions on the size of the deviations from (36).

In 1982, Shelest, Snigirev and Zinovjev derived a 'double DGLAP' equation dictating the LO scaling violations of a quantity $D_p^{ij}(x_1, x_2; Q)$ which we shall refer to as the double PDF or dPDF [94]. Snigirev identified this quantity with the factorised longitudinal piece of the two-parton GPD for the case in which the two scales are equal ($Q_A = Q_B = Q$) [77]. The equation reads as follows:

$$Q^2 \frac{dD_p^{j_1 j_2}(x_1, x_2; Q)}{dQ^2} = \frac{\alpha_s(Q^2)}{2\pi} \left[\sum_{j_1'} \int_{x_1}^{1-x_2} \frac{dx_1'}{x_1'} D_p^{j_1' j_2}(x_1', x_2; Q) P_{j_1' \to j_1}\left(\frac{x_1}{x_1'}\right) \right.$$

$$+ \sum_{j_2'} \int_{x_2}^{1-x_1} \frac{dx_2'}{x_2'} D_p^{j_1 j_2'}(x_1, x_2'; Q) P_{j_2' \to j_2}\left(\frac{x_2}{x_2'}\right)$$

$$\left. + \sum_{j'} D_p^{j'}(x_1 + x_2; Q) \frac{1}{x_1 + x_2} P_{j' \to j_1 j_2}\left(\frac{x_1}{x_1 + x_2}\right) \right] \tag{37}$$

The first two terms on the right hand side of (37) are associated with changes in the dPDF due to independent branching processes – processes in which there are a pair of partons, one of which has the appropriate x and flavour, and the other of which splits, either giving rise to the other parton of the appropriate x and flavour, or removing it. The most interesting term is the final inhomogeneous term, which represents the increase in the dPDF due to a single parton with momentum fraction $x_1 + x_2$ splitting into a pair with the appropriate x values and flavours. We call this the 'sPDF feed term' for obvious reasons. The functions $P_{j \to j_1 j_2}(x)$ that appear in this term are known as the $1 \to 2$ splitting functions, and may be obtained trivially at LO from the real splitting parts of the usual splitting functions.

An important prediction of the double DGLAP equation is that even if the dPDF may be taken to be a product of single PDFs at some particular scale Q_0, then at any other scale the dPDFs deviate from factorised forms (with more deviation the further away one moves from Q_0).

More recently [82], we demonstrated that certain equalities are preserved by the double DGLAP equation, provided that they hold at some initial scale Q_0. By comparing these equations to an equation in conditional probability, we interpreted these equalities as the number and momentum sum rules for the dPDFs, and argued that they should hold at the initial scale Q_0. The sum rules are:

$$\text{Momentum Sum Rule:} \qquad \sum_{j_1} \int_0^{1-x_2} dx_1 x_1 D_p^{j_1 j_2}(x_1, x_2; Q) = (1 - x_2) D_p^{j_2}(x_2; Q) \tag{38}$$

$$\text{Number Sum Rule:} \qquad \int_0^{1-x_2} dx_1 D_p^{j_{1v} j_2}(x_1, x_2; Q) = \begin{cases} N_{j_{1v}} D_p^{j_2}(x_2; Q) & \text{when } j_2 \neq j_1 \text{ or } \bar{j}_1 \\ (N_{j_{1v}} - 1) D_p^{j_2}(x_2; Q) & \text{when } j_2 = j_1 \\ (N_{j_{1v}} + 1) D_p^{j_2}(x_2; Q) & \text{when } j_2 = \bar{j}_1 \end{cases} \tag{39}$$

The symbol $j_{1v} \equiv j_1 - \bar{j}_1$ ($j_1 \neq g$), and $N_{j_{1v}}$ is the number of 'valence' j_1 quarks in the proton. The first sum rule is a simple statement of the fact that if one observes a parton with momentum fraction x_2 in the proton, the momentum fractions of all other partons must add up to $1 - x_2$. The second rule states that if one observes a parton with flavour j in the proton, the number of partons of flavour j elsewhere in the proton must be reduced by one (we use the term 'number effects' to describe this simple phenomenon). The sum rules give us some information about the deviations of the dPDFs from factorised forms at any scale – certainly, factorised forms do not obey the relations (38) and (39).

In this contribution, we principally wish to discuss the development of our publicly available set of LO dPDFs – the GS09 dPDFs – which have been constructed incorporating pQCD evolution effects and sum rule constraints [82]. This discussion may be found in Section 4.3.1. However, we should also like to mention some theoretical problems that we have recently uncovered in the aforementioned 'dPDF framework' for calculating proton-proton cross sections – this is covered in Section 4.3.2.

4.3.1 The GS09 dPDFs

The GS09 dPDF package comprises a grid of dPDF values spanning the ranges $10^{-6} < x_1 < 1$, $10^{-6} < x_2 < 1$, $1 \text{ GeV}^2 < Q^2 < 10^9 \text{ GeV}^2$, which is available along with interpolation code from HepForge [117]. It has been obtained by constructing inputs that approximately satisfy the sum rules at $Q_0 = 1$ GeV, and then numerically evolving these inputs up to higher scales according to the dDGLAP equation. The sPDF set to which we have chosen our dPDF set to correspond is (a slightly modified version of) the MSTW2008LO set [118].

Given the paucity of experimental data regarding the dPDFs, and in accordance with simple arguments and the CDF results, we base our inputs on factorised products of MSTW2008LO sPDFs. However, we modify these basic forms in several ways to ensure that the input dPDFs approximately satisfy the sum rules.

First, all of the dPDFs are multiplied by a factor $\rho^{ij}(x_1, x_2)$ which is designed to take account of phase space effects. This factor should ensure the appropriate behaviour of the dPDFs near the kinematic boundary $x_1 + x_2 = 1$ – namely, a smooth decrease to zero. In previous studies, universal phase factors such as $(1 - x_1 - x_2)$ and $(1 - x_1 - x_2)^2$ were used – however, with the benefit of knowledge of the momentum sum rules, we can see that neither of these options is fully satisfactory. Double PDFs including these factors badly violate the momentum sum rules along the lines $x_1 = 0$ and $x_2 = 0$. In these regions, a phase factor of approximately 1 would be more sensible (to reflect the fact that, ignoring number effects, removing a very low momentum parton does not strongly affect the probability of finding any other parton). Indeed, factorised forms satisfy the sum rules perfectly along the lines $x_1 = 0$ and $x_2 = 0$.

It was discovered that the following form for ρ^{ij} gives rise to inputs which satisfy the momentum sum rules (plus appropriate number sum rules) well:

$$\rho^{ij}(x_1, x_2) = (1 - x_1 - x_2)^2 (1 - x_1)^{-2-\alpha(j)} (1 - x_2)^{-2-\alpha(i)} \tag{40}$$

$\alpha(i)$ is 0 if i is a sea parton, and 0.5 if it is a valence parton. The latter two factors on the right hand side are included to compensate the decrease of the $(1 - x_1 - x_2)^2$ factor along the lines $x_1 = 0$ and $x_2 = 0$.

We recall that there are only a finite number of valence quarks in the proton, as opposed to an infinite number of sea quarks and gluons. Number effects are therefore most significant in the context of valence quarks, and on this basis we have chosen to only take account of valence number effects in our inputs. This is done by dividing the $u_v u_v$ part of any dPDF by two, and completely subtracting the $d_v d_v$ part. The reasoning behind this is that removing one up valence quark essentially halves the probability to find another, whilst there is no chance of finding two valence down quarks in the proton.
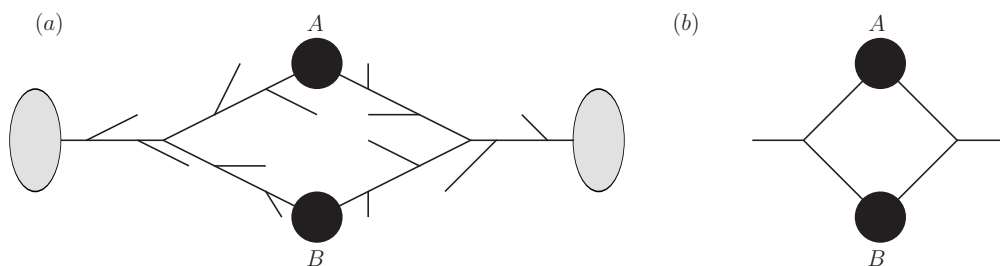
Fig. 33. (a): A diagram that apparently contributes to the leading order DPS cross section according to the 'dPDF framework' described in Section 1. **(b):** If the dPDF framework of Section 1 is valid, then it should be possible to derive the $1 \to 2$ splitting functions by examining the IR singular parts of this parton-level diagram.

Finally, we have added extra terms to input distributions whose flavour indices contain $j\bar{j}$ combinations to take account of so-called '$j\bar{j}$ correlations'. These are essentially related to sea parton number effects, although they can alternatively be thought of as arising during evolution from some lower scale to Q_0 via $g \to j\bar{j}$ splittings. It is important to include these terms in the equal flavour valence-valence ($j_v j_v$) inputs since the '$j\bar{j}$ correlation' term is much larger for these than the quasi-factorised piece at low x.

With these adjustments, our dPDF inputs satisfy all sum rules to better than 25% accuracy for $x \lesssim 0.8$ (in the normal 'double human' basis).

4.3.2 Is the proton-proton DPS cross section describable in terms of dPDFs?

Let us consider the calculation of the cross section for a particular (equal-scale) DPS process using the framework outlined at the beginning of this section – that is, folding parton level cross sections together with the dPDFs of (37) according to (35). Due to the presence of the sPDF feed term in the dDGLAP equation, there will be a contribution to the leading order cross section corresponding to diagrams like figure 33(a) in this calculation. For figure 33(a) to make a contribution to the leading order DPS cross section, it must be the case that there is a $\int dk_\perp / k_\perp$ singularity associated with every branching, even at the vertices at which the branches on either side of the diagram split into two. Only then will the branches on either side of the diagram contribute a leading $(\alpha_S \log(Q^2))^N$ factor to the cross section.

Indeed, if the dPDF framework is valid, then it should be possible to derive the $1 \to 2$ splitting functions by examining the IR singular parts of figure 33(b), just as it is possible to derive (say) the P_{qq} splitting function by examining the IR singular part of a Drell-Yan diagram with one ISR gluon [119]. However, it has been established that the diagram of figure 33(b) possesses no IR divergence in several specific cases (in each study, quarks ran around the loop – the cases that have been examined are $gg \to W^+W^-$ [120], $gg \to ZZ$ [121], and $2\gamma \to 2\gamma + 2\gamma$ [122]). We conjecture that figure 33(b) has no IR divergence whatever the initiating partons, loop partons, or hard processes are, and that figure 33(a) does not contribute to the leading order DPS cross section for similar reasons.

There is a further, more obvious, problem with the dPDF framework. In this framework, the same transverse separation profile is effectively assigned to every part of the dPDF, with the width of the profile being of the same order as the proton radius. This seems sensible for those parts of the dPDF that have arisen as a result of independent branchings. On the other hand, pairs of partons arising as a result of perturbative parton splittings do not 'know' about the size of the proton – how can it be appropriate to assign an effective transverse area of approximately the size of the proton to these pairs?

There is clearly a flaw in the dPDF framework. The root of the problem seems to be the assumption that the two-parton GPD may be decomposed into longitudinal and transverse pieces (as one might have guessed from the previous paragraph). Parton pairs arising from perturbative splittings have a singular transverse separation profile, which differs significantly from the $\boldsymbol{b}$ profile of partons produced by independent branching [86].

The dPDF introduced in Section 1 actually seems to be the integral of the two-parton GPD over $\boldsymbol{b}$. As a result it is directly accessed only in DPS processes in which the two particles probing the proton are uncorrelated in transverse space (e.g. the two-nucleon contribution to proton-heavy nucleus DPS [123,124]). It is nonetheless interesting to ask how 'wrong' it is numerically to use (35) plus GS09 dPDFs to calculate DPS cross sections. At present, we can be reasonably certain that the contribution associated with the sPDF feed parts of both dPDFs being multiplied together should not be included. However, numerically one finds that the accumulated contribution of the sPDF feed term to any dPDF is about 10% at low x [82] – therefore this contribution only represents roughly $10\% \times 10\% = 1\%$ of the cross section. To definitively answer this question of how wrong the dPDF framework is, we must discover the correct framework for calculating proton-proton DPS – we are currently working on this.

4.4 MPI: General Features and Consistency Requirements
Contributing authors: G. Calucci and D. Treleani

4.4.1 Incoherence and MPI

MPI cross sections are expressed by the incoherent sum of the contributions due to different numbers of interactions[125, 126,59]. A given final state may be however generated by various competing processes, characterized by different numbers of partonic collisions and the cross section is the result of diagonal and off-diagonal contributions. Terms with different numbers of interactions, giving rise to the same final state, populate the final state phase space in a different way and, in the kinematical regions where the contributions to the cross section are similar, important interference effects should be expected.
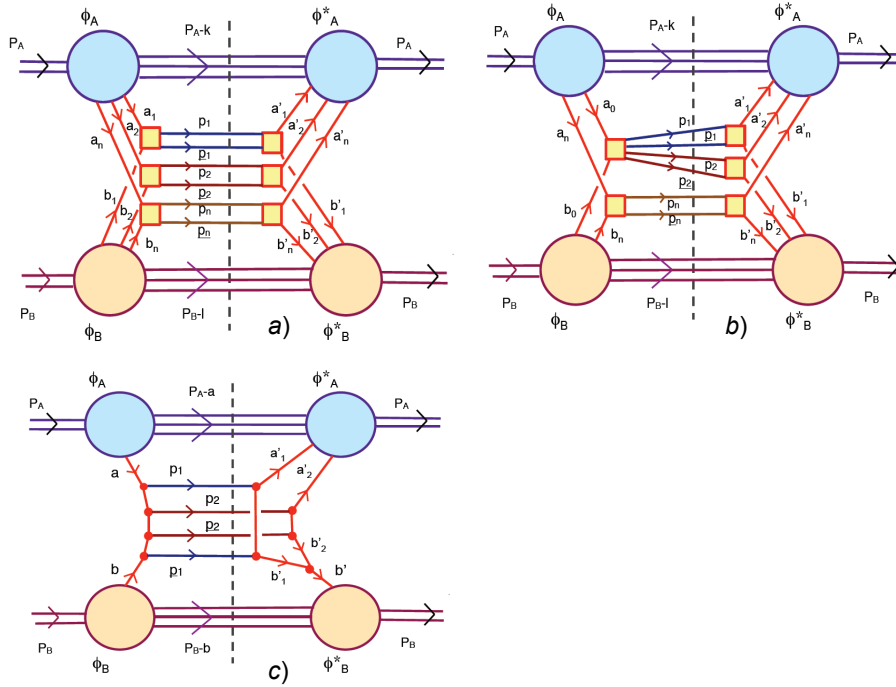

Fig. 34. a) A diagonal and b) a off diagonal contribution to the MPI cross section. c) an interference and higher order term.

A diagonal contribution, corresponding to a term with n-partons in the initial state of each interacting hadron, is given by the incoherent super-positions of n disconnected parton interactions, localized in n different points in transverse space, Fig. 1a). On the other hand, the hard component of the interaction, corresponding to the interference between a term with n partons and a term with $n' < n$ partons, is disconnected and localized in no more than n' points in transverse space, Fig. 1b) [81]. Partons are localized in the hadron by the momenta exchanged in the interaction. When partons are localized inside non overlapping regions, much smaller as compared to the hadron size, they are only connected one with another through soft exchanges and the picture of independent parallel collisions, which characterizes a diagonal contribution to the cross section, is a meaningful one. If, on the contrary, several partons are localized by the interaction inside overlapping regions, much smaller as compared to the hadron size, they are allowed to interact by exchanging momenta of the size of their virtuality. In an interference term more than two initial state partons are localized in the same interaction region[81]. Because of the localization in transverse space, the problem of interferences is thus linked to the problem to evaluate the scattering amplitude, at higher orders in the coupling constant and including higher twists in the hadron structure, Fig. 1c). One may hence argue that interference terms do not represent corrections to the n-pairs of partons scattering inclusive cross section. They rather correct the n'-pairs of partons, with $n' < n$, scattering inclusive cross section.

Given the two very different scales in the process, the hadron size and the large momenta exchanged, the hard component of the interaction may be disconnected, with the different hard parts linked only through soft exchanges

and localized in different regions in transverse space. Different MPI terms are hence conveniently understood as the contributions to the final state due to the different disconnected regions, where the hard component of the interaction is localized. In the simplest case, in each different disconnected region the interaction may be evaluated at the lowest order in the coupling constant. In each single partonic collision all transverse momenta balance and a MPI process contributes to the cross section by generating different groups of final state partons where the large transverse momenta are compensated separately.

When MPI are understood in the topological sense described above, different MPI terms, corresponding to different localizations in transverse space, do not interfere and the final cross section is obtained by the simple superposition of the cross sections, due to the contributions of the different topological configurations of the hard component of the interaction. MPI hence add incoherently. A remarkable consequence is that MPI allow a probabilistic description.

4.4.2 The Probabilistic Picture of MPI: A Functional Approach, Cancellation of Unitarity Corrections

As Multiple Parton Interactions add incoherently, the problem may be discussed within a probabilistic framework[51][80]. A functional approach is most general. One may start by introducing the probabilities W_n, to find the hadron in configurations with n-partons with coordinated $u_1 \dots u_n$, $u_i \equiv (b_i, x_i)$, where b_i are the transverse parton coordinates and x_i the fractional momenta, and the multi-parton generating functional, $\mathcal{Z}$:

$$W_n(u_1 \dots u_n), \qquad \mathcal{Z}[J] = \sum_n \frac{1}{n!} \int J(u_1) \dots J(u_n) W_n(u_1 \dots u_n) du_1 \dots du_n. \tag{41}$$

Probability conservation implies the normalization condition $\mathcal{Z}[1] = 1$, while the probabilities of the various configurations, W_n, are the coefficients of the expansion of $\mathcal{Z}[J]$ at $J = 0$. The coefficients of the expansion of $\mathcal{Z}[J]$ at $J = 1$ give the many body densities, i.e. the inclusive distributions:

$$D_1(u) = \frac{\delta \mathcal{Z}}{\delta J(u)} \bigg|_{J=1}, \qquad D_2(u_1, u_2) = \frac{\delta^2 \mathcal{Z}}{\delta J(u_1) \delta J(u_2)} \bigg|_{J=1} \qquad \dots \tag{42}$$

Correlations, which describe how much the distribution deviates from a Poissonian, are obtained by the expansion of the logarithm of the generating functional, $\mathcal{F}[J] \equiv \ln \mathcal{Z}[J]$, at $J = 1$:

$$\mathcal{F}[J] = \int D_1(u)[J(u) - 1] du + \sum_{n=2}^{\infty} \frac{1}{n!} \int C_n(u_1 \dots u_n) \big[J(u_1) - 1 \big] \dots$$
$$\dots \big[J(u_n) - 1 \big] du_1 \dots du_n \tag{43}$$

One has $\mathcal{F}[1] = 0$ and, in the case $C_n \equiv 0, n \geq 2$, the multi-parton distribution is a Poissonian.
Given the multiparton distributions W_n, one may express the hard cross section in a functional form:

$$\sigma_{hard} = \int d\beta \quad \sum_{n,m} \frac{1}{n!} \frac{\delta}{\delta J(u_1)} \dots \frac{\delta}{\delta J(u_n)} \mathcal{Z}_A[J] \frac{1}{m!} \frac{\delta}{\delta J'(u'_1 - \beta)} \dots \frac{\delta}{\delta J'(u'_m - \beta)} \mathcal{Z}_B[J']$$
$$\times \left\{ 1 - \prod_{i=1}^{n} \prod_{j=1}^{m} [1 - \hat{\sigma}_{i,j}(u, u')] \right\} \prod du du' \bigg|_{J=J'=0} \tag{44}$$

here β is the impact parameter between the two interacting hadrons A and B and $\hat{\sigma}_{i,j}$ is the probability for the parton i (of A) to have an hard interaction with the parton j (of B).
The hard cross section is obtained by summing all contributions due to all different hadronic configurations (the sums over n and m). For each pair of values n and m, one has a contribution to σ_{hard} when at least one hard interaction takes place. Given n and m, the probability to have at least one hard interaction is represented by the term in curly brackets.
The cross section is analogous to the expression of the inelastic nucleus-nucleus cross section in the Glauber model[127] and takes into account both disconnected interactions (which imply $n = m$) and rescatterings (when $n \neq m$). In the present case one is interested in disconnected interactions. One may hence simplify the expression in Eq.(4) by neglecting all rescatterings. To that purpose the term in curly brackets is replaced with the following expression:

$$\left\{1 - \exp \sum_{ij} \ln(1 - \hat{\sigma}_{ij})\right\} = 1 - \exp\left[-\sum_{ij}\left(\hat{\sigma}_{ij} + \frac{1}{2}\hat{\sigma}_{ij}\hat{\sigma}_{ij} + \dots\right)\right]$$

$$\Rightarrow \sum_{ij} \hat{\sigma}_{ij} - \frac{1}{2}\sum_{ij}\sum_{k\neq i, l\neq j} \hat{\sigma}_{ij}\hat{\sigma}_{kl} \dots \tag{45}$$

where, in the second line, all repeated indices (which correspond to rescatterings) have been suppressed. In particular only the first term of the expansion of the logarithm in the first line in Eq.(5) needs to be taken into account. The symmetry of the integrand with respect to the indices allows obtaining a compact expression of the hard cross section:

$$\sigma_{hard}(\beta) = \exp(\partial) \cdot \exp(\partial')\left[1 - \exp\left(-\partial \cdot \hat{\sigma} \cdot \partial'\right)\right]\mathcal{Z}_A[J]\mathcal{Z}_B[J']\Big|_{J=J'=0}$$

$$= \left[1 - \exp\left(-\partial \cdot \hat{\sigma} \cdot \partial'\right)\right]\mathcal{Z}_A[J]\mathcal{Z}_B[J']\Big|_{J=J'=1} \tag{46}$$

where all convolutions are understood.

Eq.(6) includes all MPI, which are identified with the disconnected collisions. The hard cross section σ_{hard} is easily expressed as a sum of MPI:

$$\sigma_{hard}(\beta) = \left[1 - \exp\left(-\partial \cdot \hat{\sigma} \cdot \partial'\right)\right]\mathcal{Z}_A[J]\mathcal{Z}_B[J']\Big|_{J=J'=1}$$

$$= \sum_{N=1}^{\infty} \frac{\left(\partial \cdot \hat{\sigma} \cdot \partial'\right)^N}{N!}\mathrm{e}^{-\partial \cdot \hat{\sigma} \cdot \partial'}\,\mathcal{Z}_A[J]\mathcal{Z}_B[J']\Big|_{J=J'=1} \tag{47}$$

It's instructive to work out the average number of collisions:

$$\langle N\rangle\sigma_{hard}(\beta) = \sum_{N=1}^{\infty} \frac{N\left(\partial \cdot \hat{\sigma} \cdot \partial'\right)^N}{N!}\mathrm{e}^{-\partial \cdot \hat{\sigma} \cdot \partial'}\,\mathcal{Z}_A[J]\mathcal{Z}_B[J']\Big|_{J=J'=1}$$

$$= \partial_{J_1} \cdot \hat{\sigma} \cdot \partial_{J'_1}\sum_{N=0}^{\infty} \frac{\left(\partial \cdot \hat{\sigma} \cdot \partial'\right)^N}{N!}\mathrm{e}^{-\partial \cdot \hat{\sigma} \cdot \partial'}\,\mathcal{Z}_A[J]\mathcal{Z}_B[J']\Big|_{J=J'=1}$$

$$= \left(\partial_{J_1} \cdot \hat{\sigma} \cdot \partial_{J'_1}\right)\mathcal{Z}_A[J]\mathcal{Z}_B[J']\Big|_{J=J'=1}$$

$$= \int D_A(x_1; b_1)\hat{\sigma}(x_1 x'_1)D_B(x'_1; b_1 - \beta)dx_1 dx'_1 d^2 b_1 \equiv \sigma_S(\beta) \tag{48}$$

where $\hat{\sigma}(x_1 x'_1)$ in the last line of Eq.(8) is the parton-parton cross section integrated with a cutoff. Given the localization of the interactions in transverse space, the parton-parton interaction probability has been treated as a δ-function of the transverse coordinates, namely $\hat{\sigma}(u, u') = \hat{\sigma}(x, x')\delta(\mathbf{b} - \mathbf{b}')$.

The average $\langle N\rangle\sigma_{hard}$ is hece equal to σ_S, the single scattering inclusive cross section of the QCD parton model. In an analogous way one obtains

$$\frac{\langle N(N-1)\rangle}{2!}\sigma_{hard}(\beta) = \frac{1}{2!}\int D_A(x_1 x_2; b_1 b_2)\hat{\sigma}(x_1 x'_1)\hat{\sigma}(x_2 x'_2)$$

$$\times D_B(x'_1 x'_2; b_1 - \beta, b_2 - \beta)dx_1 dx'_1 d^2 b_1 dx_2 dx'_2 d^2 b_2 \equiv \sigma_D(\beta) \tag{49}$$

where σ_D is the double parton scattering inclusive cross section. The relation is easily extended to any number of MPI. One obtains

$$\frac{\langle N(N-1)\dots(N-K+1)\rangle}{K!}\sigma_{hard}(\beta) = \frac{1}{K!}\int D_A(x_1\dots x_K; b_1\dots b_K)\hat{\sigma}(x_1 x'_1)\dots\hat{\sigma}(x_K x'_K)$$

$$\times D_B(x'_1\dots x'_K; b_1 - \beta\dots b_K - \beta)\prod_{i=1}^{K} dx_i dx'_i d^2 b_i \equiv \sigma_K(\beta) \tag{50}$$

which proves that, *when rescatterings are neglected*, for any choice of multiparton distributions, the inclusive cross sections are given by the moments of the distribution in the number of collisions.

4.4.3 Inclusive and Exclusive Cross Sections, Sum Rules

In proton-proton collisions, the inclusive cross sections are thus the moments of the distribution in the number of MPI. The most basic information on the distribution in the number of collisions, the average number, is hence given by the single scattering inclusive cross section of the QCD parton model. Analogously the Kth scattering inclusive cross section gives the Kth moment of the distribution in the number of collisions and is related directly to the K-partons distribution of the hadron structure.

A way alternative to the set of moments, to provide the whole information of the distribution, is represented by the set of the different terms of the probability distribution of multiple collisions. Correspondingly, in addition to the set of the inclusive cross sections, one may consider the set of the "exclusive" cross sections, where one selects the events where only a given number of collisions are present[51]. The cross sections called now "exclusive" are in fact partially inclusive cross sections, since one sums over all large p_t partons outside a given phase space interval and over all soft fragments.

Interestingly, in its study of double parton collisions, the CDF experiment[3] did not measure the double parton scattering inclusive cross section. The events selected where in fact only those containing just double parton collisions, while all events with triple scatterings (about 17% of the sample of all events with double parton scatterings) where removed. The resulting quantity measured by CDF is hence different with respect to the inclusive cross sections usually discussed in large momentum transfer physics. In fact CDF measured the double parton scattering "exclusive" cross section.

One should emphasize that the "exclusive" cross sections are not given by the usual QDC-parton model expression of large p_t processes. While the inclusive cross sections are in fact linked directly to the multi-parton structure of the hadron, the link of the "exclusive" cross sections with the hadron structure is much more complex. The requirement of having only events with a given number of hard collisions implies in fact that the corresponding cross section (being proportional to the probability of not having any further hard interaction) depends, at least in principle, on the whole series of multiple hard collisions and hence on an infinite non-perturbative input. One has

$$\sigma_{hard} = \sum_{N=1}^{\infty} \tilde{\sigma}_N, \qquad \sigma_K = \sum_{N=K}^{\infty} \frac{N(N-1)\ldots(N-K+1)}{K!}\tilde{\sigma}_N \qquad (51)$$

where $\tilde{\sigma}_N$ is the "exclusive" cross section of N partonic collisions, while σ_K is the inclusive cross section of K partonic collisions. Notice that Eq. 51 is a set of sum rules that relate inclusive and "exclusive" MPI cross sections. Notice also that MPI add incoherently in the final cross section, leading to a different probabilistic picture of the process in each phase space interval, in such a way that one may associate a different probability distribution of MPI to each different phase space choice of observing the final state. In a given phase space window only a small number of MPI might give a sizable contribution to σ_{hard}. If, as an example, the relevant contributions to σ_{hard} are at most from triple collisions, one may write

$$\tilde{\sigma}_1 = \sigma_S - 2\sigma_D + 3\sigma_T$$
$$\tilde{\sigma}_2 = \sigma_D - 3\sigma_T$$
$$\tilde{\sigma}_3 = \sigma_T \qquad (52)$$

which shows how to express the "exclusive" cross sections in terms of well defined elements of the non perturbative hadron structure, in the phase space window under consideration.

Any final state phase space window identifies an interval in momentum transfer and in fractional momenta, which represents the domain of definition of the corresponding probability distribution of MPI. The same interval in momentum transfer and fractional momenta represents also the integration domain of the integrated terms, which appear in the "exclusive" differential cross sections. Integrated terms appear in the "exclusive" differential cross sections because of the normalization of the probability distribution. The limits of the integrated terms are thus fixed unambiguously by normalization and coincide with the kinematical limits adopted to select the final state.

$$d\sigma_S(u, u') = D_A(u)d\hat{\sigma}(u, u')D_B(u')$$
$$d\tilde{\sigma}_1(u, u') = D_A(u)d\hat{\sigma}(u, u')D_B(u')\Big[1 - \int D_A(u_1)\hat{\sigma}(u_1, u_1')D_B(u_1')du_1 du_1'\Big]$$
$$\qquad - \Big[\int D_A(u)d\hat{\sigma}(u, u')C_B(u', u_1')\hat{\sigma}(u_1', u_1)D_A(u_1)du_1 du_1' + A \leftrightarrow B\Big]$$
$$\qquad - \int C_A(u_1, u)d\hat{\sigma}(u, u')C_B(u', u_1')\hat{\sigma}(u_1', u_1)du_1 du_1' \qquad (53)$$

In Eq.(13) the explicit expressions of the single scattering inclusive, $\sigma_S(u, u')$, and "exclusive", $\tilde{\sigma}_1(u, u')$, differential cross sections are given as a function of the coordinates u, u' of the observed partons. The expression of the inclusive cross section holds at all orders in $\hat{\sigma}$, while the "exclusive" cross section is at the order $\hat{\sigma}^2$.
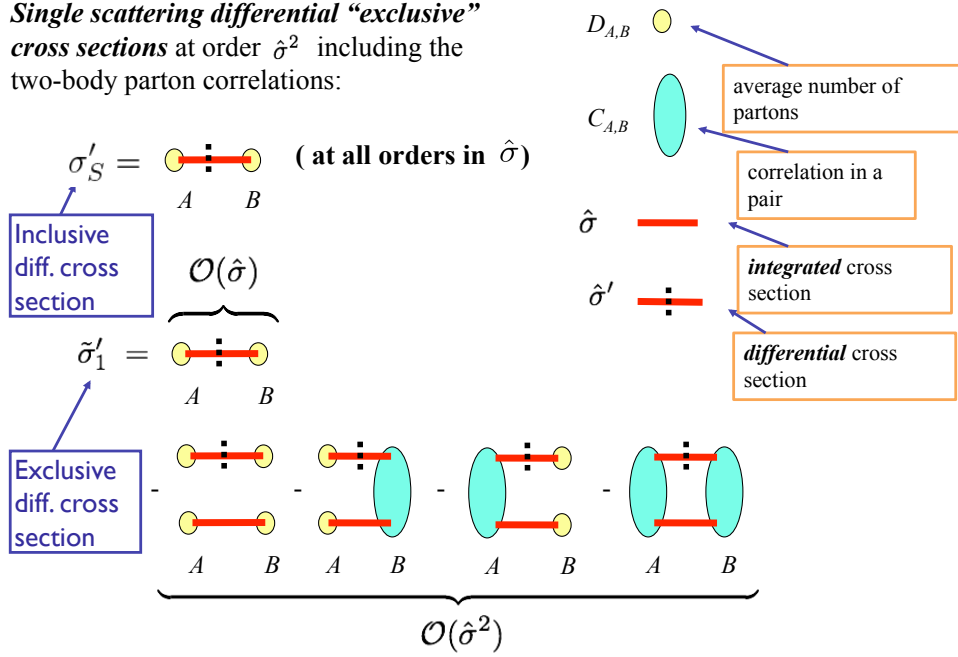

Fig. 35. Single scattering differential inclusive and "exclusive" cross sections including the two-body parton correlations. The "exclusive" cross section is at order $\hat{\sigma}^2$.

By restricting the phase space interval of the observed final state, $\tilde{\sigma}_1$ is therefore well expressed by the term linear in $\hat{\sigma}$. In that limit the probability of interaction is well approximated by the average of the distribution, while $\tilde{\sigma}_2$ is negligibly small and the single parton scattering "exclusive" cross section is well represented by the single scattering expression of the simple QCD parton model σ_S. When the phase space volume is increased, the single scattering "exclusive" cross section becomes increasingly different from the single scattering of the simple QCD parton model and the difference between σ_S and $\tilde{\sigma}_1$ allows a direct measure of the importance of correlations, Fig.2.

Notice that the components of the hadron structure, namely the terms D and C, are well defined quantities, as they do not mix when the kinematical limits adopted to select the final state are changed. The effect of modifying the kinematical limits adopted to select the final state is in fact only to change the integration domain of each term, namely to probe the multi-parton structure of the hadron in different domains in x and Q^2[51].

Inclusive and "exclusive" cross sections result from independent measurements. By checking the sum rules, comparing the measured integrated inclusive cross section with the sum of the measured integrated "exclusive" cross sections, taken with the proper multiplicity factors, up to a given order in the number of collisions, one has hence a direct indication of the importance of terms with larger numbers of partonic collisions in a given phase space interval. In a phase space interval where, as an example, only single and double collisions give sizable contributions, one may thus obtain information on the effect of two body parton correlations by looking at the difference between the single scattering inclusive and "exclusive" differential cross sections:

$$\frac{d\sigma_S}{dyd\mathbf{p}_t} - \frac{d\tilde{\sigma}_1}{dyd\mathbf{p}_t} = \frac{d\sigma_S}{dyd\mathbf{p}_t} \frac{\sigma_S}{\sigma_{eff}} \qquad (54)$$

By comparing the behavior, as a function of fractional momenta, of the difference in the left hand side of Eq.(14) with the right hand side one obtains information on the value of the effective cross section and on the dependence of σ_{eff} on y and $\mathbf{p}_t$.

4.4.4 Concluding Summary

Given the extended nature of the interacting systems, the hard component of a hadronic interaction is, in general, disconnected. The different terms of a MPI process correspond to the different regions where the hard component of the interaction is localized. In a single partonic collision all transverse momenta balance and a MPI process contributes to the cross section by generating different groups of final state partons where the large transverse momenta are compensated separately. A consequence is that terms with different numbers of hard interactions add incoherently and the MPI cross section is obtained by the superposition of the cross sections, due to the contributions of the different topologies of the hard component of the interaction.

The physical picture of MPI is hence probabilistic, which leads naturally to consider two different sets of cross sections, the inclusive cross sections, given by the moments of the probability distribution of MPI, and the "exclusive" cross sections, given by the different terms of the probability distribution. The inclusive cross sections depend on all the different terms of the distribution in multiplicity of partonic interactions, each counted with a different multiplicity factor, while each "exclusive" cross section corresponds to a given term of the distribution. A consequence is that inclusive and "exclusive" cross sections, which result from independent measurements, are linked by sum rules, which are implied by the relations expressing the moments of a probability distribution.

Of course different final state phase space windows lead to different probability distributions of MPI and the number of MPI can be controlled by adjusting the final state phase space interval. The sum rules are thus saturated with a different number of terms in each different final state phase space interval. The number of terms needed to saturate the sum rules in the phase space interval under consideration provides a quantitative measure of the importance of terms with larger numbers of partonic interactions. Given the number of terms needed to saturate the sum rules, the non-perturbative input to the "exclusive" cross sections is given explicitly in terms of well defined properties of the hadron structure, which hence allow to evaluate unambiguously also the "exclusive" cross sections in perturbative QCD.

4.5 Multiple interactions, diffraction, and the BFKL pomeron
Contributing author: G. Gustafson

In high energy pp scattering the cross section for minijet production becomes very large, and unitarity implies that multiple interactions, saturation, and diffraction become important. Effects of saturation and multiple interactions are most easily described in impact parameter space, as parton rescattering is represented by a convolution in transverse momentum space, which corresponds to a simple multiplication in transverse coordinate space.

The proton has an internal substructure, which may be excited in a diffractive scattering process, and diffractive excitation represents large fractions of the cross section in pp collisions or DIS. In the Good–Walker formalism [128] diffractive excitation is described by the fluctuations in the scattering amplitude. In most analyses of pp collisions this mechanism is used only for low mass excitation, while high mass excitation is described by a triple-regge formula [129, 130], where regge trajectories and couplings are fitted to experimental data (for recent analyses see *e.g.* Refs. [131, 132,133]).

The proton substructure is represented by a parton cascade, which at high energies is described by BFKL evolution. The fluctuations in this evolution are known to be very large [134]. An analysis of these fluctuations, within the Lund Dipole Cascade model, is able to reproduce the experimental cross sections for diffractive excitation in pp collisions or DIS [135,136]. This implies that the effective pomeron couplings in the multi-pomeron formalism can be estimated without any new free parameters.

It should also be noticed that the classification of diffractive events varies between different formalisms, and cannot be uniquely defined. Therefore it is recommended to study gap events rather than diffractive events.

4.5.1 The eikonal approximation and the Good–Walker formalism

As mentioned in the introduction, diffraction, saturation, and multiple interactions are most easily described in impact parameter space. If the scattering is driven by absorption into inelastic states i, with weights $2f_i$, the elastic amplitude is given by

$$T = 1 - e^{-F}, \quad \text{with } F = \sum f_i. \tag{55}$$

For a structureless projectile we find:

$$\begin{cases} d\sigma_{tot}/d^2b = \langle 2T \rangle, \\ \sigma_{el}/d^2b = \langle T \rangle^2, \\ \sigma_{inel}/d^2b = \langle 1 - e^{-\sum 2f_i} \rangle \sim \sigma_{tot} - \sigma_{el}. \end{cases} \tag{56}$$

If the projectile has an internal structure, the mass eigenstates Ψ_k can differ from the eigenstates of diffraction Φ_n, which have eigenvalues T_n. With the notation $\Psi_k = \sum_n c_{kn}\Phi_n$ (with $\Psi_{in} = \Psi_1$) the elastic amplitude is given by $\langle\Psi_1|T|\Psi_1\rangle = \sum c_{1n}^2 T_n = \langle T\rangle$, while the amplitude for diffractive transition to mass eigenstate Ψ_k is given by $\langle\Psi_k|T|\Psi_1\rangle = \sum_n c_{kn}T_n c_{1n}$. The corresponding cross sections become

$$d\sigma_{el}/d^2b = (\sum c_{1n}^2 T_n)^2 = \langle T\rangle^2 \tag{57}$$

$$d\sigma_{diff}/d^2b = \sum_k \langle\Psi_1|T|\Psi_k\rangle\langle\Psi_k|T|\Psi_1\rangle = \langle T^2\rangle. \tag{58}$$

The diffractive cross section here includes elastic scattering. Subtracting this gives the cross section for diffractive excitation, which is determined by the fluctuations in the scattering process:

$$d\sigma_{diff\,ex}/d^2b = d\sigma_{diff} - d\sigma_{el} = \langle T^2\rangle - \langle T\rangle^2. \tag{59}$$

4.5.2 Dipole cascade models

Mueller's dipole cascade model [137,138,139] is a formulation of BFKL evolution in transverse coordinate space. Gluon radiation from the color charge in a parent quark or gluon is screened by the accompanying anticharge in the color dipole. This suppresses emissions at large transverse separation, which corresponds to the suppression of small $k_\perp$ in BFKL. For a dipole $(\mathbf{x}, \mathbf{y})$ the probability per unit rapidity (Y) for emission of a gluon at transverse position $\mathbf{z}$ is given by

$$\frac{d\mathcal{P}}{dY} = \frac{\bar{\alpha}}{2\pi} d^2\mathbf{z} \frac{(\mathbf{x} - \mathbf{y})^2}{(\mathbf{x} - \mathbf{z})^2(\mathbf{z} - \mathbf{y})^2}, \quad \text{with } \bar{\alpha} = \frac{3\alpha_s}{\pi}. \tag{60}$$

The dipole is split into two dipoles, which (in the large N_c limit) emit new gluons independently. The result is a cascade, where the number of dipoles grows exponentially with Y.

When two cascades collide, a pair of dipoles with coordinates $(\mathbf{x}_i, \mathbf{y}_i)$ and $(\mathbf{x}_j, \mathbf{y}_j)$ can interact via gluon exchange with the probability $2f_{ij}$, where

$$f_{ij} = f(\mathbf{x}_i, \mathbf{y}_i|\mathbf{x}_j, \mathbf{y}_j) = \frac{\alpha_s^2}{8}\left[\log\left(\frac{(\mathbf{x}_i - \mathbf{y}_j)^2(\mathbf{y}_i - \mathbf{x}_j)^2}{(\mathbf{x}_i - \mathbf{x}_j)^2(\mathbf{y}_i - \mathbf{y}_j)^2}\right)\right]^2. \tag{61}$$

Summing over all dipoles in the cascades then reproduces the LL BFKL result. The elastic scattering amplitude is given by $T = 1 - \exp(-\sum f_{ij})$, and the cross sections are given by Eqs. (56, 57, 58).

The *Lund cascade model* [140,141,142] is a generalization of Mueller's model, which includes:
– NLL BFKL effects
– Nonlinear effects in the evolution
– Confinement effects

For an incoming virtual photon splitting in a $q\bar{q}$ pair, the initial state wavefunction is determined by perturbative QCD. For an incoming proton we make an ansatz in form of an equilateral triangle of dipoles. After evolution the result is rather insensitive to the exact form of the initial state. The model is also implemented in a MC program DIPSY. The model reproduces successfully the total and (quasi)elastic cross sections for DIS and pp scattering.

4.5.3 Fluctuations and diffractive excitation

The fluctuations in the evolution are large, and the model can also describe diffractive excitation within the Good–Walker formalism, without new parameters beyond those adjusted to the total and elastic cross sections [135]. This is similar in spirit to the early analysis by Miettinen and Pumplin [143]. In DIS saturation effects are not very important, while in pp collisions saturation effects strongly suppress the fluctuations, and thus the cross section for diffractive excitation.

γ^*p **collisions**

The distribution in the non-saturated scattering amplitude, F, is shown in Fig. 36 for different impact parameters. The distribution can be approximately described by a power $\frac{dP}{dF} \approx A\,F^{-p}$ (with a cutoff for small F-values), which is illustrated by the straight lines in the figure. The width of this distribution is rather large, and the approximation gives the ratio $d\sigma_{diff.ex.}/d\sigma_{tot} \approx 1 - 1/2^{2-p}$. In the simulations the power p is rather independent of the impact parameter, and therefore this result is also valid for the integrated cross sections. This gives $\sigma_{diff}/\sigma_{tot} \sim 0.13$ at $Q^2 = 50\,\text{GeV}^2$, decreasing for larger Q^2, but fairly insensitive to the energy W.
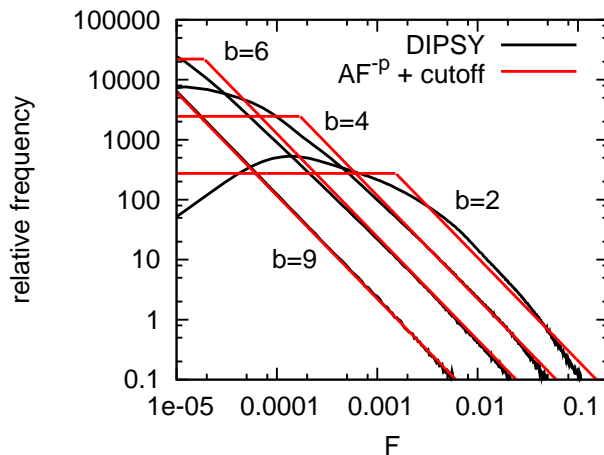
Fig. 36. Distribution in the one-pomeron amplitude F in DIS for $Q^2 = 14$ GeV^2 and $W = 220$ GeV. The photon is here represented by a dipole with size $r = 1/Q$. The impact parameter b is measured in GeV^{-2}.
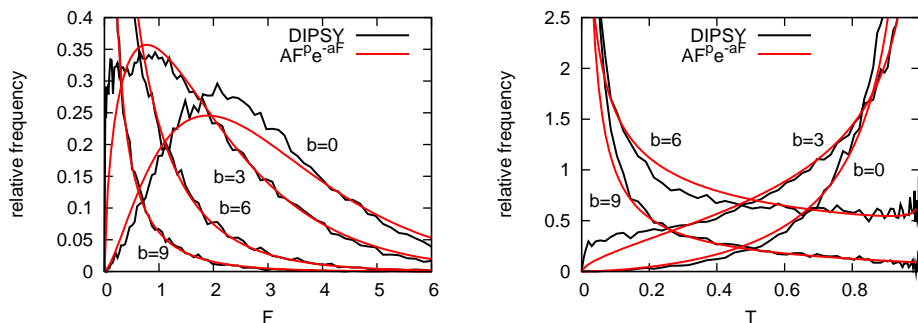

Fig. 37. Distribution in the one-pomeron amplitude (F, left) and the uniterized amplitude (T, right) in pp collisions at 2 TeV. Notation as in Fig. 1.

pp collisions

In pp scattering the Born amplitude is large, and therefore unitarity effects are important. Figure 37 shows both the Born amplitude and the unitarized amplitude at 2 TeV for different b-values. We see that the width of the Born amplitude is large, and without unitarization the fraction of diffractive excitation would be similar to that for $\gamma^* p$ for lower Q^2-values. (The smooth lines are fits of the form $AF^p e^{-aF}$.)

However, the unitarized amplitude is limited by 1, and the width, and therefore the diffractive excitation, is very much reduced. This is in particular the case for central collisions where the amplitude approaches the black disc limit, as seen in the right panel in Fig. 37. This result corresponds to the effect of enhanced diagrams in the conventional triple-regge approach. The impact parameter profile is shown in Fig. 38. We see that the cross section for diffractive excitation is largest in a ring with radius $b \sim 1$ fm. This result also implies that factorization is not satisfied when comparing diffractive excitation in DIS and pp scattering.

4.5.4 Comparison with multi-regge analyses

It is also interesting to compare the results from the Good–Walker analysis with the multi-regge formalism. To this end we study the contribution from the *bare pomeron*, meaning the one-pomeron amplitude without contributions from saturation, enhanced diagrams or gap survival form factors. When s, M_X^2, and s/M_X^2 are all large, pomeron exchange should dominate. The results of the MC for the total, elastic, and single diffractive cross sections are shown by the crosses in the right panel in Fig. 38. We note that the results are very well reproduced by a triple-regge expression with a single pomeron pole, with the parameters

$$\alpha(0) = 1.21, \quad \alpha' = 0.2 \, \text{GeV}^{-2}, \quad g_{pP}(t) = (5.6 \, \text{GeV}^{-1}) \, e^{1.9t}, \quad g_{3P}(t) = 0.31 \, \text{GeV}^{-1}, \tag{62}$$

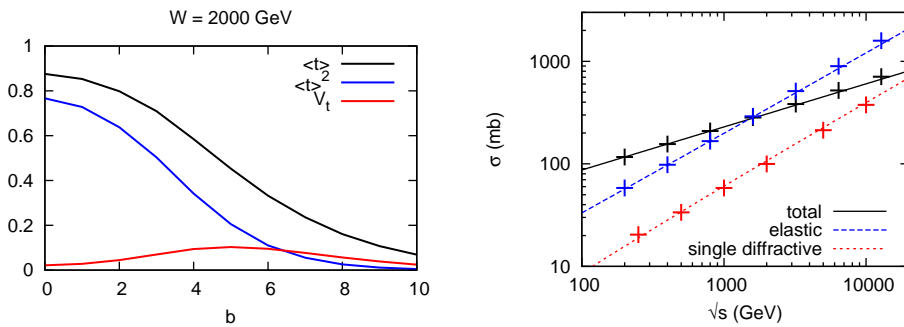which is shown by the straight lines. Also the t-dependence of diffractive excitation is well reproduced.

Fig. 38. *Left*: Impact parameter distributions for $\langle T \rangle = (d\sigma_{\mathrm{tot}}/d^2b)/2$, $\langle T \rangle^2 = d\sigma_{\mathrm{el}}/d^2b$, and $V_T = d\sigma_{\mathrm{diffex}}/d^2b$ in pp collisions at $W = 2$ TeV. b is in units of GeV^{-1}. *Right*: The total, elastic, and single diffractive cross sections in the one-pomeron approximation. The crosses are model calculations and the lines are from a tuned triple-regge parametrisation.

These results can also be compared with multi-regge analyses, where *e.g.* Ryskin *et al.* [131] obtain $\alpha(0) = 1.3$, $\alpha' \leq 0.05\,\mathrm{GeV}^{-2}$, Kaidalov *et al.* [132] find $\alpha(0) = 1.12$, $\alpha' = 0.22\,\mathrm{GeV}^{-2}$, while Gotsman *et al.* [133] find $\alpha(0) = 1.335$, $\alpha' = 0.01\,\mathrm{GeV}^{-2}$. Thus our values are somewhere in between. We also note that the Good–Walker results are reproduced by a single pomeron pole, *i.e.* not by a cut as expected in LL BFKL, or a series of poles as obtained with a running coupling [144]. Also the triple-regge coupling g_{3P} is approximately constant, while in LL BFKL it is proportional to $\sim 1/\sqrt{|t|}$ [138,145].

4.5.5 Can diffraction be uniquely defined?

Multipomeron diagrams are included in the dipole picture, with fixed multi-pomeron couplings. However, all events with no gap are classified as inelastic. This can be compared to the formalism in Ref. [131], in which a large cross section for overlapping double diffraction is obtained.

To compare predictions from different models with each other and with experiments, we need a unique definition of diffraction. One attempt might be events with two separate color singlet systems, containing the original valence quarks. This could be obtained by exchange of two (or more) gluons forming a color singlet. If such a state is obtained in a calculation in perturbative QCD, a gap could, however, be filled by final state radiation or nonperturbative strings, or else a gap could be formed by color reconnection. Thus diffractive events cannot be uniquely defined by perturbative QCD. The definition varies between different schemes, and for a specified event the diffractive capacity is not an observable. The solution must be: study observables, meaning events with a gap.

4.5.6 Summary

- In high energy pp scattering unitarity implies a high probability for multiple interactions, and a large diffractive cross section. In the Good–Walker formalism elastic scattering is given by the average of the scattering amplitude, while the fluctuations determine the diffractive excitation.
- Parton cascades fill the whole rapidity range between projectile and target. The fluctuations in BFKL evolution are large, and within the Lund Dipole Cascade model they can describe diffractive excitation within the Good–Walker formalism, to both low and high masses.
- When the interaction approaches the black disc limit in central pp collisions, fluctuations and diffractive excitation is suppressed. This leads to factorization breaking in comparisons of DIS and pp scattering.
- The result of the model calculations corresponds to a bare pomeron, which is a simple pole, and an almost constant triple-pomeron coupling.
- Diffractive excitation is scheme dependent, and cannot be uniquely defined. Study gap events.

5 Phenomenology of Multi-parton Interactions

Due to its high collision energy and luminosity, the LHC provides a valuable opportunity to observe multiple parton hard-scatterings, in particular many DPS processes. Theoretical investigations of double parton scattering have a long history, with a large number of studies evaluating the DPS contribution to high energy processes [96,58,146,147,148, 149,150,151,152,153,154,155,156].

Compared with the DPS processes already observed, namely final states involving 4 jets (at the AFS collaboration at the CERN ISR [1]), and $\gamma + 3$ jets (at the CDF [3] and the D0 [4] collaborations at the Fermilab Tevatron), processes at the LHC involve different scales and initial state partons, hence providing complementary information on DPS. Moreover, large contributions from double parton scattering could, for example, result in a larger rate for multi-jet production than otherwise predicted, and produce relevant backgrounds in searches for signals of new phenomena. It is thus important to know empirically how large the double parton contribution may be and what dependence on relevant kinematic variables it has. Specifically, the differences between final states produced in SPS and in DPS processes need to be studied in order to separate between these processes and gain more detailed experimental information on DPS. In addition to its role in general LHC phenomenology, the DPS measurements will have an impact on the development of partonic models of hadrons, since the effective cross section for double parton scattering measures the size in impact parameter space of the incident hadron's partonic hard core.

The DPS phenomenology is based on the general expression for the cross section $\sigma_{(A,B)}^{DPS}$, cf. Section 4.3,

$$\sigma_{(A,B)}^{DPS} = \frac{m}{2} \sum_{i,j,k,l} \int dx_1 dx_2 dx_1' dx_2' d^2b \Gamma_{ij}(x_1, x_2, b; t_1, t_2) \Gamma_{kl}(x_1', x_2', b; t_1, t_2) \hat{\sigma}_{ik}^A(x_1, x_1') \hat{\sigma}_{jl}^B(x_2, x_2'). \tag{63}$$

The $\Gamma_{ij}(x_1, x_2, b; t_1, t_2)$ represent double parton distributions. They may be loosely interpreted as the inclusive probability distributions to find a parton $i(j)$ with longitudinal momentum fraction $x_1(x_2)$ at scale $t_1 \equiv \ln(Q_1^2)(t_2 \equiv \ln(Q_2^2))$ in the proton, with the two partons separated by a transverse distance b. The scale $t_1(t_2)$ is given by the characteristic scale of subprocess $A(B)$. The quantity m is a symmetry factor that equals 1 if $A = B$ and 2 otherwise. Separating the transverse part, $\Gamma_{i,j}(x_1, x_2, b; t_1, t_2) = D_{i,j}(x_1, x_2, t_1, t_2) \times F(b)$, Eq. 63 becomes

$$\sigma_{(A,B)}^{DPS} = \frac{m}{2\sigma_{\text{eff}}} \sum_{i,j,k,l} \int dx_1 dx_2 dx_1' dx_2' D_{i,j}(x_1, x_2, t_1, t_2) D_{k,l}(x_1', x_2', t_1, t_2) \hat{\sigma}_{ik}^A(x_1, x_1', t_1) \hat{\sigma}_{jl}^B(x_2, x_2', t_2),$$

$$\sigma_{\text{eff}} = \left[\int d^2b (F(b))^2 \right]^{-1}. \tag{64}$$

If one makes the further assumptions that double parton distributions reduce to the product of two independent one parton distributions, $D_{i,j} = D_i \times D_j$, the DPS cross section can be expressed in the simple form

$$\sigma_{(A,B)}^{DPS} = \frac{m}{2} \frac{\sigma_A \sigma_B}{\sigma_{eff}}. \tag{65}$$

In this section the phenomenological studies for the production of two jets in association with a $b\bar{b}$ pair (in section 5.1), same–sign W pair (in section 5.2) and $Z+$ jets (in section 5.3) are reviewed.

5.1 Dynamical Characteristics of Double Parton Scattering
Contributing author: E. Berger

The concept of a DPS process consisting of two short-distance subprocesses occuring in a given hadronic interaction, with two initial partons being active from each of the incident protons, is shown for illustrative purposes in Fig. 39. It may be contrasted with conventional single parton scattering (SPS) in Fig.40, in which one short-distance subprocess occurs, with one parton active from each initial hadron. Both produce the same 4 parton final state. Our aims in Ref. [157] are to address whether double parton scattering can be shown to exist as a discernible contribution in well defined and accessible final states, and to establish the characteristics features that allow its measurement. We show that double parton scattering produces an enhancement of events in regions of phase space in which the "background" from single parton scattering is relatively small. If such enhancements are observed experimentally, with the kinematic dependence we predict, then we will have a direct empirical means to measure the size of the double parton contribution.

From the perspective of sensible rates and experimental tagging, a good process to examine should be the 4 parton final state in which there are 2 hadronic jets plus a b quark and a $\bar{b}$ antiquark, viz. $b \bar{b} j_1 j_2$. If the final state arises from double parton scattering, then it is plausible that one subprocess produces the $b \bar{b}$ system and another subprocess produces the two jets. There are, of course, many single parton scattering (2 to 4 parton) subprocesses that can result in the $b \bar{b} j_1 j_2$ final state, and we identify kinematic distributions that show notable separations of the two contributions.

The state-of-the-art of calculations of single parton scattering is well developed whereas the phenomenology of double parton scattering is less advanced. For $pp \rightarrow b\bar{b}j_1j_2X$, assuming that the two subprocesses $A(i\ j \rightarrow b\ \bar{b})$ and $B(k\ l \rightarrow j_1\ j_2)$ in Fig. 39 are weakly correlated, and that kinematic and dynamic correlations between the two partons
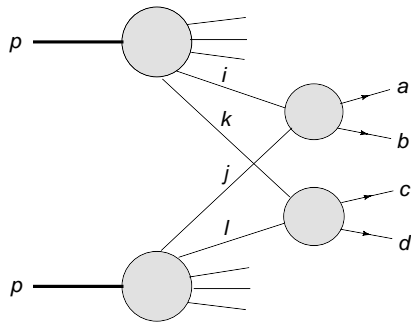
Fig. 39. Sketch of a double-parton process in which the active partons are i and k from one proton and j and l from the second proton. The two hard scattering subprocess are $A(i\ j \to a\ b)$ and $B(k\ l \to c\ d)$.
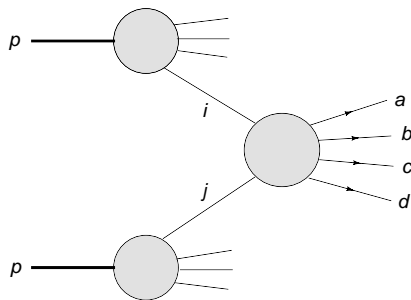

Fig. 40. Sketch of a single-parton process in which the active partons are i from one proton and j from the second proton. The hard scattering subprocess is $A(i\ j \to a\ b\ c\ d)$.

from each hadron may be safely neglected, we employ the common heuristic expression for the DPS differential cross section

$$d\sigma^{DPS}(pp \to b\bar{b}j_1j_2X) = \frac{d\sigma^{SPS}(pp \to b\bar{b}X)d\sigma^{SPS}(pp \to j_1j_2X)}{\sigma_{\text{eff}}}. \tag{66}$$

The numerator is a product of single parton scattering cross sections. In the denominator, there is a term σ_{eff} with the dimensions of a cross section. Given that one hard-scatter has taken place, σ_{eff} measures the size of the partonic core in which the flux of accompanying short-distance partons is confined. Collider data [4] yield values in the range $\sigma_{\text{eff}} \sim 12$ mb. We use this value for the estimates we make, but we emphasize that the goal should be determine its value at LHC energies.

In Ref. [157], we present the details of our calculation of the double parton and the single parton contributions to $p\ p \to b\ \bar{b}\ j_1\ j_2\ X$. We perform full event simulations at the parton level and apply a series of cuts to emulate experimental analyses. We also treat the double parton and the single parton contributions to 4 jet production, again finding that good separation is possible despite the combinatorial uncertainty in the pairing of jets.

5.1.1 Distinguishing variables

Correlations in the final state are predicted to be quite different between the double parton and the single parton contributions. For example, we examine the distribution of events as function of the angle Φ between the planes defined by the $b\bar{b}$ system and by the jj system. If the two scattering processes $ij \to b\bar{b}$ and $kl \to jj$ which produce the DPS final state are truly independent, one would expect to see a flat distribution in the angle Φ. By contrast, many diagrams, including some with non-trivial spin correlations, contribute to the 2 parton to 4 parton final state in SPS $ij \to b\bar{b}$jetjet, and one would expect some correlation between the two planes. In Fig. 41, we display the number of events as a function of the angle between the two planes. There is an evident correlation between the two planes in SPS, while the distribution is flat in DPS, indicative that the two planes are uncorrelated.

Another interesting difference between DPS and SPS is the behavior of event rates as a function of transverse momentum. As an example of this, in Fig. 42, we show the transverse momentum distribution for the leading jet (either a b or light j) for both DPS and SPS. SPS produces a relatively hard spectrum, and for the value of σ_{eff} and the cuts that we use, SPS tends to dominate over the full range of transverse momentum considered. On the other
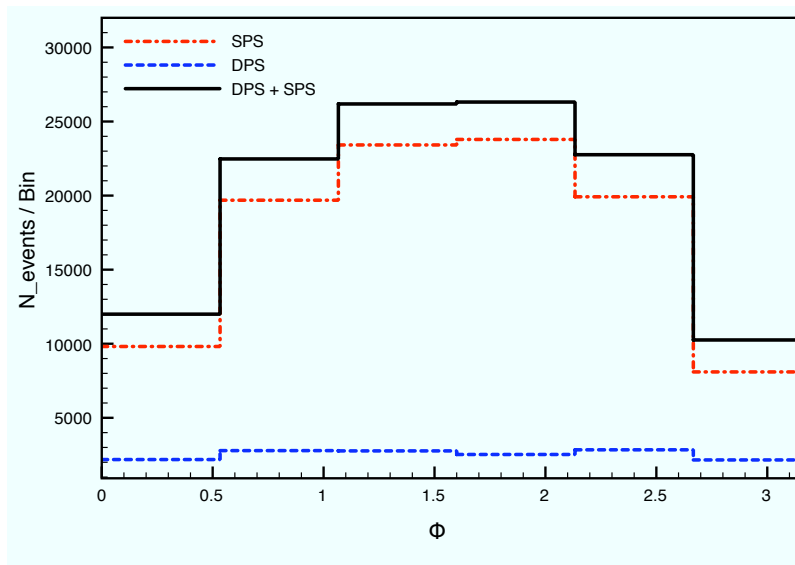
Fig. 41. Event rate as a function of the angle between the two planes defined by the $b\bar{b}$ and jj systems. In SPS events, there is a correlation among the planes which is absent for DPS events.

hand, DPS produces a much softer spectrum which (up to issues of normalization in the form of σ_{eff}) can dominate at small values of transverse momentum. The cross-over between the two contributions to the total event rate is ~ 30 GeV for the acceptance cuts considered. A smaller (larger) value of σ_{eff} would move the cross-over to a larger (smaller) value of the transverse momentum of the leading jet.
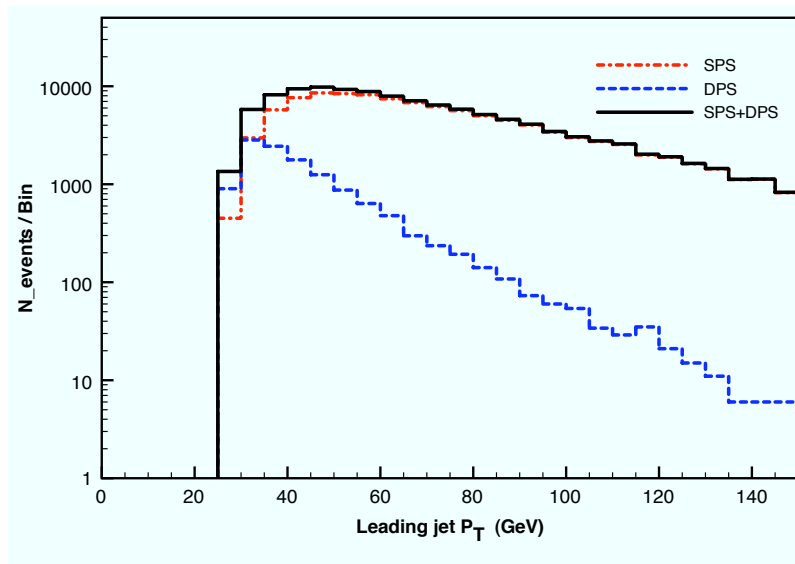

Fig. 42. The transverse momentum p_T distribution of the leading jet in $jjb\bar{b}$ after minimal cuts.

We turn next to the search for variables that may allow for a clear separation of the DPS and SPS contributions. Since the topology of the DPS events includes two $2 \to 2$ hard scattering events, the two pairs of jet objects are roughly back-to-back. We expect the azimuthal angle between the pairs of jets corresponding to each hard scattering event to be strongly peaked near $\Delta\phi_{jj} \sim \Delta\phi_{bb} \sim \pi$. Real radiation of an additional jet, where the extra jet is missed because it fails the threshold or acceptance cuts, allows smaller values of $\Delta\phi_{jj}$. The relevant distribution is shown for light jets (non b-tagged) in Fig. 43a. There is a clear peak near $\Delta\phi_{jj} = \pi$ for DPS events, while the events are more

broadly distributed in SPS events. The secondary peak near small $\Delta\phi_{jj}$ arises from gluon splitting which typically produces nearly collinear jets. The suppression at still lower $\Delta\phi_{jj}$ comes from the isolation cut $\Delta R_{jj} > 0.4$.
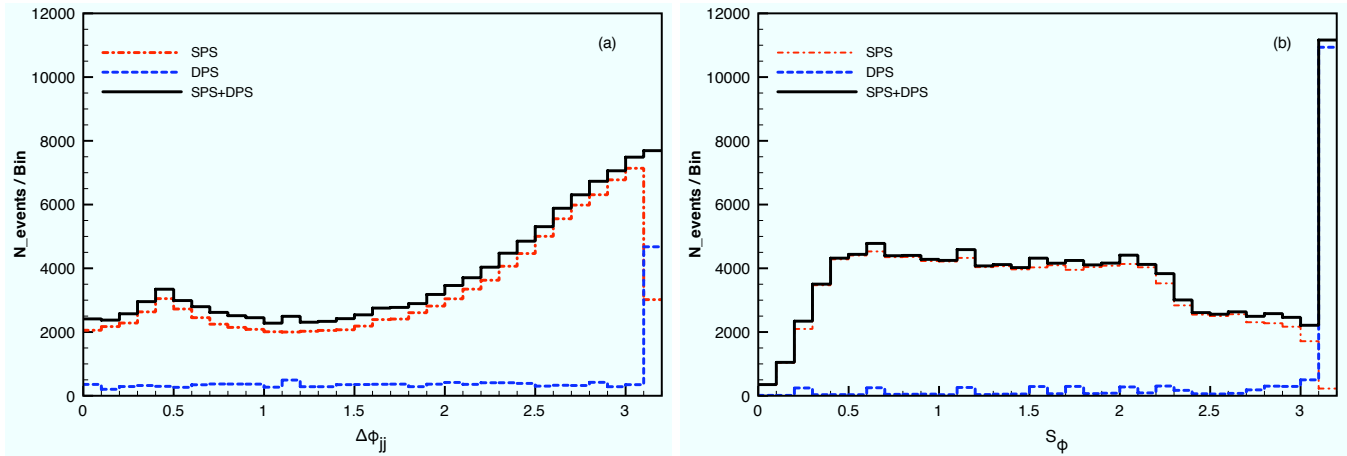

Fig. 43. (a) The difference $\Delta\phi$ in the azimuthal angles of light jet pairs for DPS and both SPS+DPS events. The dijet pairs are back-to-back in DPS events. (b) The variable S_ϕ for DPS and SPS+DPS events provides a stronger separation of the underlying DPS events from the total sample when compared to $\Delta\phi$ for any pair.

The separation of DPS events from SPS events becomes more pronounced if information is used from both the $b\bar{b}$ and jj systems. As an example, we consider the distribution built from a combination of the azimuthal angle separations of both jj and $b\bar{b}$ pairs, using a variable adopted from Ref. [4]:

$$S_\phi = \frac{1}{\sqrt{2}}\sqrt{\Delta\phi(b_1, b_2)^2 + \Delta\phi(j_1, j_2)^2}. \tag{67}$$

In Fig. 43b, we present a distribution in S_ϕ for both DPS and SPS+DPS events. Again, as in the case of the $\Delta\phi$ distribution, the SPS events are broadly distributed across the allowed range of S_ϕ. However, the combined information from both the $b\bar{b}$ and jj systems shows that the DPS events produce a sharp and substantial peak near $S_\phi \simeq \pi$ which is well-separated from the total sample.

The narrow peaks near $\Delta\phi_{jj} = \pi$ in Fig. 43a and near $S_\phi = 1$ in Fig. 43b will be smeared somewhat once soft QCD radiation and other higher-order terms are included in the calculation.

Another possibility for discerning DPS is the use of the total transverse momentum of both the $b\bar{b}$ and jj systems. At lowest order for a $2 \to 2$ process, the vector sum of the transverse momenta of the final state pair vanishes. In reality, radiation and momentum mismeasurement smear the expected peak near zero. Nevertheless, the DPS events are expected to show a reasonably well-balanced distribution in the transverse momenta of the jet pairs. To encapsulate this expectation for both light jet pairs and b-tagged pairs, we use the variable [4]:

$$S'_{p_T} = \frac{1}{\sqrt{2}}\sqrt{\left(\frac{|p_T(b_1, b_2)|}{|p_T(b_1)| + |p_T(b_2)|}\right)^2 + \left(\frac{|p_T(j_1, j_2)|}{|p_T(j_1)| + |p_T(j_2)|}\right)^2}. \tag{68}$$

Here $p_T(b_1, b_2)$ is the vector sum of the transverse momenta of the two final state b jets, and $p_T(j_1, j_2)$ is the vector sum of the transverse momenta of the two (non b) jets.

The distribution in S'_{p_T} is shown in Fig. 44. As expected, the DPS events are peaked near $S'_{p_T} \sim 0$ and are well-separated from the total sample. The SPS events, on the other hand, tend to be far from a back-to-back configuration and, in fact, are peaked near $S'_{p_T} \sim 1$. This behavior of the SPS events is presumably related to the fact that a large number of the $b\bar{b}$ or jj pairs arise from gluon splitting which yields a large p_T imbalance and, thus, larger values of S'_{p_T}.

Our simulations suggest that the variable S'_{p_T} may be a more effective discriminator than S_ϕ. However, given the leading order nature of our calculation and the absence of smearing associated with initial state soft radiation, this picture may change and a variable such as S_ϕ (or some other variable) may become a clearer signal of DPS at the LHC. Realistically, it would be valuable to study both distributions once LHC data are available in order to determine which is more instructive.
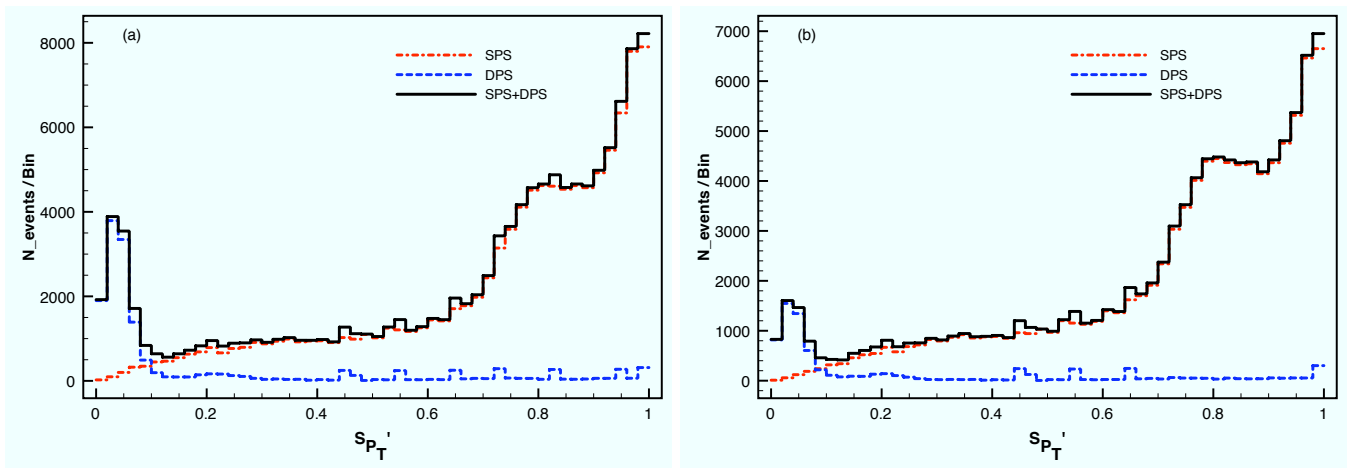
Fig. 44. Distribution of events in S'_{p_T} for the DPS and SPS samples. Due to the back-to-back nature of the $2 \to 2$ events in DPS scattering, the transverse momenta of the jet pair and of the b-tagged jet pair are small, resulting in a small value of S'_{p_T}. In (a) we show the S'_{p_T} distribution for our standard cuts, and in (b) we increase the cut on the transverse momentum of the leading jet, $p_T^{j1} > 40$ GeV. The fraction of DPS events in the whole sample decreases with increasing p_T^{j1}.

The evidence in one-dimensional distributions for distinct regions of DPS dominance prompts the search for greater discrimination in a plane represented by a two dimensional distribution of one variable against another. One scatter plot with interesting features is displayed in Fig. 45. The DPS events are seen to be clustered near $S'_{p_T} = 0$ and are uniformly distributed in Φ. The SPS events peak toward $S'_{p_T} = 1$ and show a roughly $\sin \Phi$ character. While already evident in one-dimensional distributions, these two features are more apparent in the scatter plot Fig. 45. Moreover, the scatter plot shows a valley of relatively low density between $S'_{p_T} \sim 0.1$ and ~ 0.4. In an experimental one-dimensional Φ distribution, one would see the sum of the DPS and SPS contributions. If structure is seen in data similar to that shown in the scatter plot Fig. 45, one could make a cut at $S'_{p_T} < 0.1$ or 0.2 and verify whether the experimental distribution in Φ is flat as expected for DPS events.

5.1.2 Strategy and Further Work

The clear separation of DPS from SPS events in Fig. 45 suggests a methodology for the study of DPS. One can begin with a clean process such as $pp \to b\bar{b}j_1j_2X$ and examine the distribution of events in the plane defined by S'_{p_T} and Φ. We expect to see a concentration of events near $S'_{p_T} = 0$ that is uniformly distributed in Φ. These are the DPS events. Assuming that a valley of low density is observed between $S'_{p_T} \sim 0.1$ and ~ 0.4, one can make a cut there that produces an enhanced DPS sample. Relative to the overall sample, this enhanced sample should show a more rapid decrease of the cross section as a function of the transverse momentum of the leading jet, and the enhanced sample can be used to measure σ_{eff}. A similar examination of other final states, such as 4 jet production, will answer whether the extracted values of σ_{eff} are roughly the same. Theoretical and experimental studies of other processes can follow, such as $b\bar{b}t\bar{t}$, Wjj, and Hjj.

On the phenomenological front, next-to-leading order (NLO) expressions should be included for both the SPS and DPS contributions. The NLO effects are expected to change normalizations and, more importantly, the distributions in phase space. The sharp peaks near $\Delta\phi_{jj} = \pi$ in Fig. 43a, $S_\phi \simeq \pi$ in Fig. 43b, and $S'_{p_T} = 0$ in Fig. 44 will be broader and likely displaced somewhat.

Finally, it would be good to examine the theoretical underpinnings of Eq. (66) and, in the process, gain better insight into the significance of σ_{eff}. A firm basis is desirable for Eq. (66) starting from the formal expression for the differential cross section in terms of the absolute square of the full matrix element integrated over phase space:

$$d\sigma(pp \to b\bar{b}j_1j_2X) = \frac{1}{2s}|M(pp \to b\bar{b}j_1j_2X)|^2 dPS_{b\bar{b}j_1j_2X}. \tag{69}$$

The amplitude $M(pp \to b\bar{b}j_1j_2X)$ should include a sum of amplitudes for 2-parton collisions (one active from each incident hadron, i.e., $2 \to 4$); 3-parton collisions (two active from one hadron and one active from the other); and 4-parton collisions (two active from each hadron or three from one and one from the other), and so forth that all yield the same 4 parton final state. There will be contributions to the final state from the squares of individual amplitudes
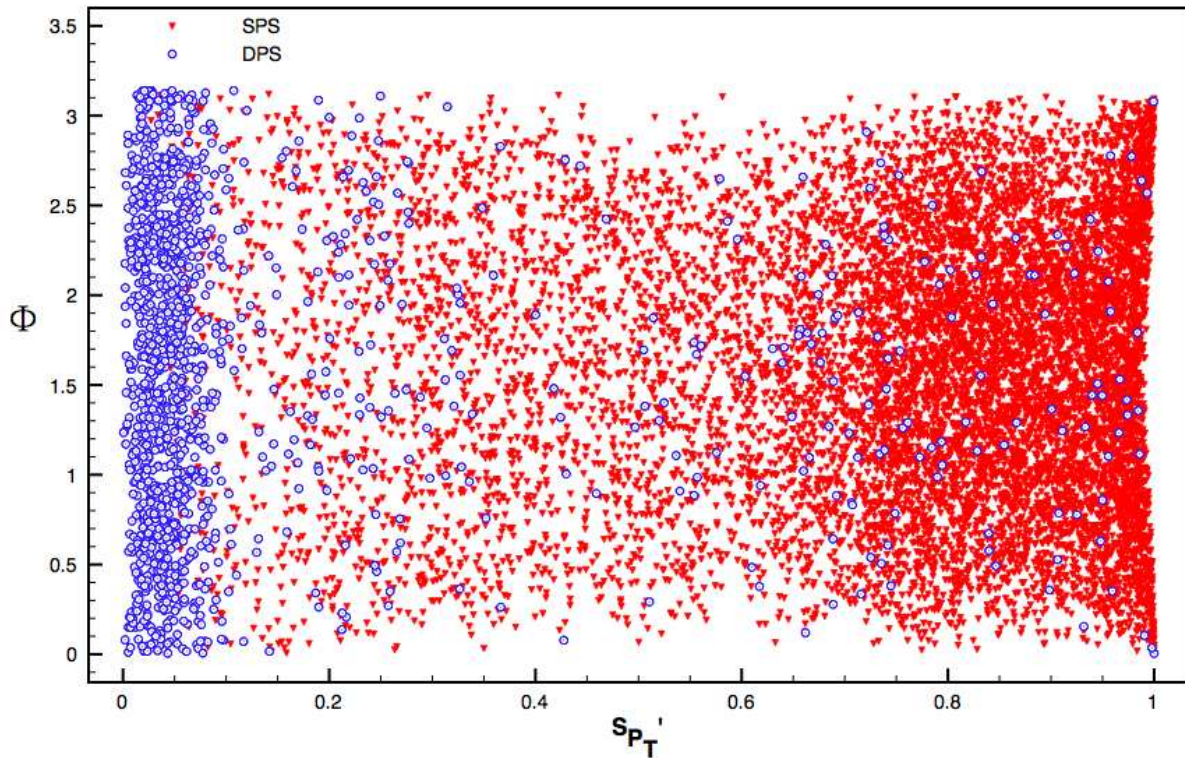
Fig. 45. Two-dimensional distribution of events in the inter-plane angle Φ and the scaled transverse momentum variable S'_{p_T} for the DPS and SPS samples.

as well as interference terms. Specializing to $4 \to 4$, the DPS case, one would start from a 4-parton $\to$ 4-parton hard part. Not evident at this time is how the four-parton matrix element can be reduced to a product of two matrix elements for the single parton scatterings, needed for Eq. (66). The demonstration of clear DPS signals in LHC data would be an important stimulus for further theoretical studies.

5.1.3 NLO DPS Study of $pp \to Wb\bar{b}X \to \ell\nu b\bar{b}X$

In a subsequent paper [158], we investigate the possibility to observe double parton scattering at the early LHC in the process $pp \to Wb\bar{b}X \to \ell\nu b\bar{b}X$. Our analysis is done at next-to-leading order in QCD. It begins with the basic assumption that $Wb\bar{b}$ production consists of two components: the traditional single parton scattering (SPS) process and the double parton scattering (DPS) process where two individual hard scatterings produce the $Wb\bar{b}$ final state.

After identifying the most relevant background processes, we pinpoint a set of observables and cuts which would allow for the best separation between the DPS $Wb\bar{b}$ signal and the backgrounds (including the SPS $Wb\bar{b}$ process). To provide the most precise predictions possible, we generate the DPS $Wb\bar{b}$ signal event sample, the SPS $Wb\bar{b}$ sample, and the dominant background event samples at next-to-leading order in QCD. The main obstacles in the extraction of the DPS signal are the backgrounds from $t\bar{t}$ production and the SPS $Wb\bar{b}$ component. The most efficient way to suppress the $t\bar{t}$ background is with an upper cut on the missing transverse energy of the event, since top quark decays result in larger values of $\not{E}_T$.

To separate the DPS component of $Wb\bar{b}$ from the SPS component, we find it useful again to employ observables which take into account information on the full final state rather than observables which involve one or two particles. Examples are the S'_{p_T} variable and the angle $(\Delta\Theta_{b\bar{b},\ell\nu})$ between the two planes defined by the $b\bar{b}$ and $\ell\nu$ systems, respectively. By displaying the information from these two observables in two-dimensional distributions, we show that it is possible to identify distinct regions in phase space where the DPS events reside. Utilizing cuts on these observables that enhance the DPS $Wb\bar{b}$ sample, we find that the DPS signal can be observed with a statistical significance in the range $S/\sqrt{B} \sim 12 - 15$.

The focus in Ref. [158] is to establish double parton scattering as a discernible physics process at LHC energies and measuring the size of its contribution. Once DPS production of $Wb\bar{b}$ is observed, it will be interesting to assess its

	σ_{GS09}	σ_{MSTW_0}	σ_{MSTW_1}	σ_{MSTW_2}
W^+W^-	0.546	0.496	0.409	0.348
W^+W^+	0.321	0.338	0.269	0.223
W^-W^-	0.182	0.182	0.156	0.136
	R			
	0.784	1.00	1.00	1.00

Table 2. DPS WW total cross sections (in pb) and ratio R defined in Eq. (70) for pp collisions at $\sqrt{s} = 14$ TeV evaluated using different dPDFs sets.

	σ_{GS09}		
	$\sqrt{s} = 7$ TeV	$\sqrt{s} = 10$ TeV	$\sqrt{s} = 14$ TeV
W^+W^-	0.107	0.250	0.546
W^+W^+	0.0640	0.148	0.321
W^-W^-	0.0317	0.0793	0.182
	R		
	0.709	0.751	0.784

Table 3. DPS WW total cross sections (in pb) and ratio R defined in Eq. (70) for pp collisions at different CM energies $\sqrt{s}$.

potential significance as a background in searches for other physics, such as Higgs boson production in association with a W boson (where the Higgs boson decays as $H \to b\bar{b}$), and precise studies of single top quark production where new physics could contribute to the Wtb vertex. A detailed analysis of either of these channels would require a different set of optimized physics cuts. We limit ourselves in Ref. [158] to showing the $b\bar{b}$ invariant mass distribution for the $\ell\nu b\bar{b}$ final state. We see that the DPS $Wb\bar{b}$ component alters the overall shape of the $b\bar{b}$ mass spectrum, enhancing the small mass region. This feature is consistent with our earlier observation that the p_T spectrum of leading jets is softer in the DPS component. The DPS component contributes primarily in the region below 120 GeV or so. At face value, it does not seem to pose a hindrance for searches for Higgs bosons in the HW channel. However, $Wb\bar{b}$ DPS could be a significant background in the search for new particles, with masses in the 50 - 100 GeV range and appearing as resonances in M_{bb}, and it should be accounted for in any analysis.

5.2 Probing double parton scattering with same-sign W pairs at the LHC
Contributing authors: J. R. Gaunt, C.-H. Kom, A. Kulesza, and W. J. Stirling

In this section we focus on $W^\pm W^\pm$ production, followed by decays into same-sign di-leptons (SSDL) plus missing transverse energies ($\not{E}_T$). Our discussion is based on [115] (see [159] for an early study of this process). One advantage in studying DPS $W^\pm W^\pm$ is that single $W^\pm$ production is well described theoretically, and will be accurately measured at the LHC. As a result an approximation with no correlations included will be well modelled. In addition, $W^\pm W^\pm$ production through single parton scattering (SPS) is forbidden at the same order in the SM, i.e. there is no $q\bar{q}' \to W^\pm W^\pm$ contribution, due to $(U(1)_{\mathrm{EM}})$ charge conservation. The lowest order 'background' process is instead $q\bar{q}' \to W^\pm W^\pm jj$, which is of order $\mathcal{O}(\alpha^4)$ or $\mathcal{O}(\alpha_S^2\alpha^2)$. The additional jet activity can be used to distinguish this background from the DPS signal.

Same-sign $W^\pm W^\pm$ production could then potentially be a benchmark DPS process. We will study kinematic properties of this process by including longitudinal correlation effects, namely constraints from momentum and valence number conservation. These constraints are consistently included in the double parton distribution function (dPDF) set GS09 [82]. We refer readers to Section 4.3 and original literature for details on the construction of this dPDF set. We will quantitatively study effects of these constraints by comparing results using GS09 with other simple dPDF models that will be defined later. In the literature, comparison of DPS and SPS $W^\pm W^\pm$ production has mostly been studied at the level of production cross sections. Here we discuss strategies to extract the signal from the background including important contributions from heavy flavour and gauge boson pair productions.

5.2.1 The $W^\pm W^\pm$ signal

Our phenomenological investigation for DPS $W^\pm W^\pm$ production is based on the equation 64, with $m = 1$, $A = B = W^\pm$ and $t_1 = t_2 = \ln(M_W^2)$. We assume $\sigma_{\mathrm{eff}} = 14.5$mb, the value obtained by the CDF $\gamma + 3j$ [3] analysis. We adopt GS09, which incorporates momentum and sum rule constraints, as the default longitudinal dPDF choice. To see the
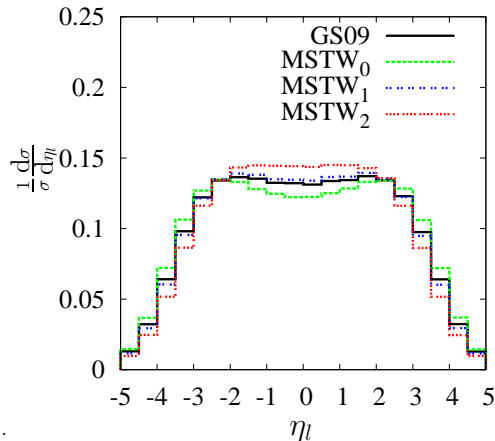
Fig. 46. Normalised l^+ pseudorapidity distributions for pp collisions at $\sqrt{s} = 14$ TeV evaluated using different dPDFs. No cuts are applied.

effect of these constraints, we compare cross sections using factorised dPDFs of the form:

$$
\begin{aligned}
D_{ij}(x_1, x_2) &= D_i(x_1)D_j(x_2) \\
&\times \theta(1 - x_1 - x_2)(1 - x_1 - x_2)^n , \\
n &= 0, 1, 2 ,
\end{aligned}
\tag{70}
$$

hereafter referred to as MSTW$_n$ sets. In the above expression, the factorization scale is again fixed at $\mu_F = M_W$. The completely factorised approximation that has been taken in existing phenomenological studies is obtained by setting $D_{ij}(x_1, x_2) = D_i(x_1)D_j(x_2)$. The sPDFs $D_i(x)$ are taken from the MSTW 2008 LO set. In Table 2, we compare the cross sections and the values of the ratio

$$
R \equiv 4 \frac{\sigma_{W^+W^+} \; \sigma_{W^-W^-}}{\sigma_{W^+W^-}^2} ,
\tag{71}
$$

which measures the deviation from the factorisation approach ($R = 1$ when factorisation is exact) using different dPDFs. In Table 3, the value R as a function of CM energy using GS09 is evaluated. We see that using GS09, factorisation is broken at the 20% to 30% level, and the approximation improves at the higher collider energies as lower x regions are probed. On the contrary, the MSTW$_n$ models have R values very close to 1 because effects of the momentum suppression factors $(1 - x_1 - x_2)^n$ in the numerator and the denominator of the expression tend to cancel.

Sum rule effects incorporated in GS09 can also be seen in the distributions of the charged leptons $l^\pm$ from $W^\pm$ decays. To understand this, note that production of same sign $W^\pm$'s along the same forward direction is suppressed compared with factorised models due to both momentum and number sum rule constraints. This is because this phase space region is significantly influenced by $D^{vv}(x_1, x_2)$, where $v = v_u, v_d$ denotes valence up or down quarks, both of which with relatively high momentum fractions x_1 and x_2. In fact, $D^{v_d v_d} = 0$ identically in GS09 due to the presence of only one valence down quark in a proton, whereas it is non-zero for other simple factorised models. The $l^\pm$ hence have more central distributions compared with the MSTW$_n$ models. The pseudorapidity (η_l) distributions for l^+ are shown in Fig. 46.

Such longitudinal correlations also imply that the SSDL pairs prefer to lie in opposite hemispheres (i.e. $\eta_{l_1} \times \eta_{l_2} < 0$). This preference can be quantified by computing pseudorapidity asymmetry, defined as

$$
a_{\eta_l} = \frac{\sigma(\eta_{l_1} \times \eta_{l_2} < 0) - \sigma(\eta_{l_1} \times \eta_{l_2} > 0)}{\sigma(\eta_{l_1} \times \eta_{l_2} < 0) + \sigma(\eta_{l_1} \times \eta_{l_2} > 0)},
\tag{72}
$$

where $|\eta_{l_1}|, |\eta_{l_2}| > \eta_l^{\min}$. The value of a_{η_l} for l^+ as a function of $\eta_l^{\min}$ is displayed in Fig. 47. It increases with $\eta_l^{\min}$ as the correlations are most important for the distributions probed at high values of x for both partons in the same proton, which is reached when the leptons are produced at high $|\eta_l|$. For GS09, this effect is even more pronounced for l^-, as only one valence down quark is present in a proton, making simultaneous extraction of two high x down quarks highly suppressed.
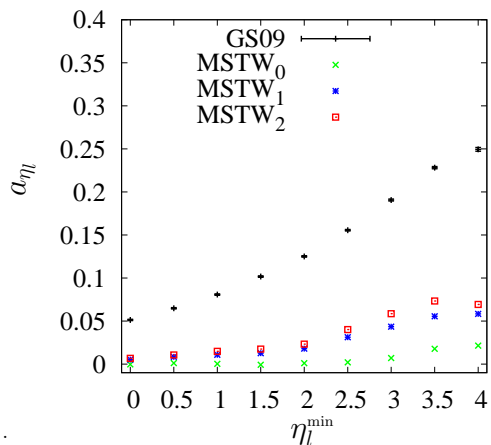
Fig. 47. Pseudorapidity asymmetry a_{η_l} for pp collisions at $\sqrt{s} = 14$ TeV evaluated using different dPDFs. No cuts are applied.
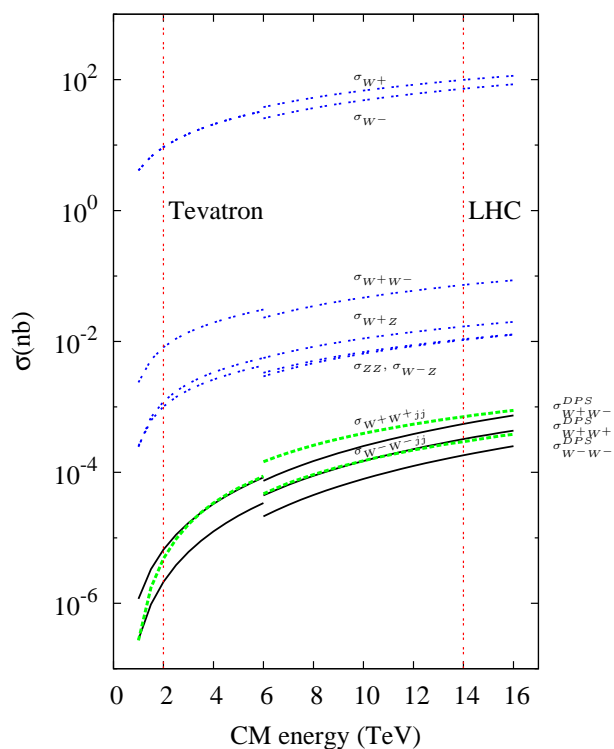

Fig. 48. Cross sections of various electroweak processes in p-$p(\bar{p})$ collisions as a function of $\sqrt{s}$. The dotted curves correspond to single scattering processes, while the solid curves correspond to double scattering processes computed using GS09 dPDFs.

5.2.2 Single scattering backgrounds

We now turn to the single scattering backgrounds. We show in Fig. 48 the total cross sections of the DPS signal, as well as electroweak single scattering backgrounds and related processes. As discussed before, due to charge conservation the lowest order 'irreducible' SPS background including a pair of same sign W's is $q\bar{q}' \rightarrow W^{\pm}W^{\pm}jj$. At the 14 TeV LHC, the DPS signal and SPS background total cross sections are of the same order of magnitude ($\mathcal{O}(0.1-1)$pb before leptonic branching ratios). However the presence of two additional hard jets means that central hard p_T jet veto can be useful in suppressing this background. The SPS cross section as a function of max jet p_T and min jet η at the parton level is displayed in Fig. 49. As we can see, this background can be suppressed easily, for instance by vetoing events with central jets with $p_T > 20$ GeV.
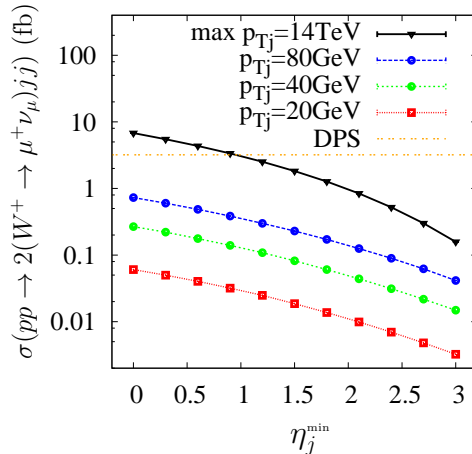
Fig. 49. $\sigma(pp \to W^+ W^+ jj) \cdot [\mathcal{BR}(W^+ \to \mu^+ \nu_\mu)]^2$ (fb) as a function of max p_{Tj} and η_j^{min}. No other cuts are applied.

Actually other electroweak processes that can lead to the same final states. In particular, both $W^\pm Z(\gamma^*)$ and $Z(\gamma^*)Z(\gamma^*)$ gauge boson production can lead to SSDL + $\not{E}_T$ when the 'wrong' sign leptons are not identified, for instance if they lie outside the central tracking region, or if they are too soft to be reconstructed. The relevant processes are

$$q\bar{q}' \to W^+ Z(\gamma^*) \to l^+ \nu l^+ (l^-),$$
$$q\bar{q} \ \to Z(\gamma^*) Z(\gamma^*) \to l^+ (l^-) l^+ (l^-), \tag{73}$$

and their charge-conjugated processes. In the above expressions, charged leptons in brackets are not identified.

As can be seen in Fig. 48, the total cross sections for $W^\pm Z$ and ZZ are about an order of magnitude above the signal, while the cross sections are significantly larger when γ^* is involved. However, for these processes the lepton p_T spectra are much harder compared with the signal, hence a max lepton p_T cut can reduce this background. A wrong sign lepton-veto in the central region will also be useful in reducing the Z contribution, while looking for presence of low invariant mass system of an isolated charged tracks and a nearby identified lepton [160] can help suppressing the γ^* contribution.

Another source of background is pair production of heavy flavour quarks. Production of $b\bar{b}$ can lead to SSDL pairs, when a neutral B-meson is present and undergos B^0-$\bar{B}^0$ mixing, followed by semi-leptonic decay for both B-mesons. The relevant processes are then:

$$gg \to b\bar{b} \to B\bar{B} + \dots ,$$
$$B \to l^+ \nu X,$$
$$\bar{B}^0 \to B^0 \to l^+ \nu \tilde{X}, \tag{74}$$

together with the charge conjugation processes.

The $b\bar{b}$ cross section is orders of magnitude larger than that of the signal. However, the p_T spectrum of the B-mesons decreases exponentially. It is thus very difficult for both charged lepton and neutrino from the semi-leptonic B decay to acquire large transverse momenta. Imposing tight lepton isolation, min lepton p_T and min $\not{E}_T$ cuts will thus help suppressing contribution from this process.

Production of $t\bar{t}$ pair can also result in SSDL pairs when a top and the bottom of the other top decay semi-leptonically. The relevant processes are

$$t \to W^+ b \to l^+ \nu b,$$
$$\bar{t} \to W^- \bar{b} \to q\bar{q}' l^+ \nu c. \tag{75}$$

These events have significant jet activities. Also, the lepton p_T spectrum is much harder compared with the signal. The leptons, particularly the ones from B-decays, are usually poorly isolated. We thus expect tight lepton isolation, central jet veto and a max lepton p_T cut will be effective in suppressing this background, and will not consider this process further in our numerical analysis.

	$\sigma_{\mu^+\mu^+}$ (fb)	$\sigma_{\mu^-\mu^-}$ (fb)
$W^\pm W^\pm$(DPS)	0.82	0.46
$W^\pm Z(\gamma^*)$	5.1	3.6
$Z(\gamma^*)Z(\gamma^*)$	0.84	0.67
$b\bar{b}$ ($p_T^b \geq 20$ GeV)	0.43	0.43

Table 4. Cross sections (in fb) of the processes simulated after cuts, including branching ratios corresponding to same-sign dimuon production.

5.2.3 Observing DPS $W^\pm W^\pm$ at the LHC

We see in the last section, that despite the backgrounds having much larger cross sections than the signal, there are handles to suppress the former processes. To see to what extent the signal can be extracted from these backgrounds, we perform a parton level signal + background simulation[3] with the following criteria:

– Both leptons in the like sign lepton pair must have pseudorapidity $|\eta| < 2.5$.
– Both leptons are required to be isolated:
$E_{\mathrm{ISO}}^l \leq E_{\mathrm{ISO}}^{\min} = 10$ GeV, where E_{ISO}^l is the hadronic transverse energy in a cone of $R = 0.4$ surrounding each of the like-sign leptons.
– The transverse momenta of both leptons, p_T^l, must satisfy $20 \leq p_T^l \leq 60$ GeV.
– An event is rejected whenever a third, opposite-signed, lepton is identified. A lepton is assumed to be identified with 100% efficiency when $p_T^l \geq p_T^{\mathrm{id}}$ and $|\eta| < \eta^{\mathrm{id}}$, where $p_T^{\mathrm{id}} = 10$ GeV and $\eta^{\mathrm{id}} = 2.5$.
– The missing transverse energy $\not{E}_T$ of an event must satisfy $\not{E}_T \geq 20$ GeV.
– Reject an event if a charged (lepton) track with $p_T^{\mathrm{id}} \geq p_T \geq 1$ GeV forms an invariant mass < 1 GeV with one of the same-sign leptons.

The cross sections after these cuts are displayed in Table 4. The largest background comes from the $W^\pm Z(\gamma^*)$ processes, which is a factor of a few larger than the signal. Unfortunately, we find that many basic kinematic distributions are fairly similar between this SPS background and the DPS signal, making further cuts unlikely to be beneficial.

On the positive side, it might be advantageous to exploit the fact that the value of a_{η_l} is relatively small, but positive, for the DPS signal. On the contrary, a_{η_l} tends to be negative for the background, which reflects the preference for the leptons to lie close in pseudorapidity space in order to reduce the CM energy of the system. This property is illustrated in the diagram on the left of Fig. 50, which shows how a_{η_l} for different processes vary as a function of a minimum η_l cut.

The ratio of positively charged ($++$) and negatively charged ($--$) SSDL events (which we call charge asymmetry ratio) may also be used, as initial state partons of various flavours and momentum fractions are involved in different processes, each leading to different charge asymmetry ratio. The charge asymmetry ratio for the DPS signal and SPS $W^\pm Z(\gamma^*)$ background using different lepton identification criteria is displayed in the right figure of Fig. 50. An important point that should be noted is that this ratio is fairly stable when varying the cuts, as can be inferred from the results in Table 4.

To summarise, same-sign $W^\pm W^\pm$ production can potentially be a benchmark process for studying double parton scattering at the LHC. We have discussed likely changes to the kinematic properties of the signal when momentum and sum rule constraints are included in the description of dPDFs. We find that, after including important physics backgrounds previously overlooked in the literature, a small excess of SSDL DPS events could be observed at the LHC, while further improvements can be made to enhance the signal. Finally, we note that there are other DPS processes with purely leptonic final states, such as double Drell-Yan and double J/psi production, that could be interesting. Recent phenomenological studies of these processes can be found in Refs [161,162,163,164,165].

5.3 Multiple Parton Interactions in $Z + jets$ production at the LHC
Contributing author: E. Maina

5.3.1 Multiple Parton Interactions in $Z + jets$ production at the LHC

In Ref. [166] the contribution of MPI to $Z + n$–jets production at the LHC, $n = 2, 3, 4$, where the Z boson is assumed to decay leptonically, has been examined. These processes have the advantage of a much larger cross section than same–sign WW production and therefore are more likely to allow detailed studies of MPI at the low luminosity, about 1 fb^{-1}, foreseen for the first two years of operation at the LHC with $\sqrt{s} = 7$ TeV.

---

[3] We refer readers to the original paper [115] for a technical account of the simulation.
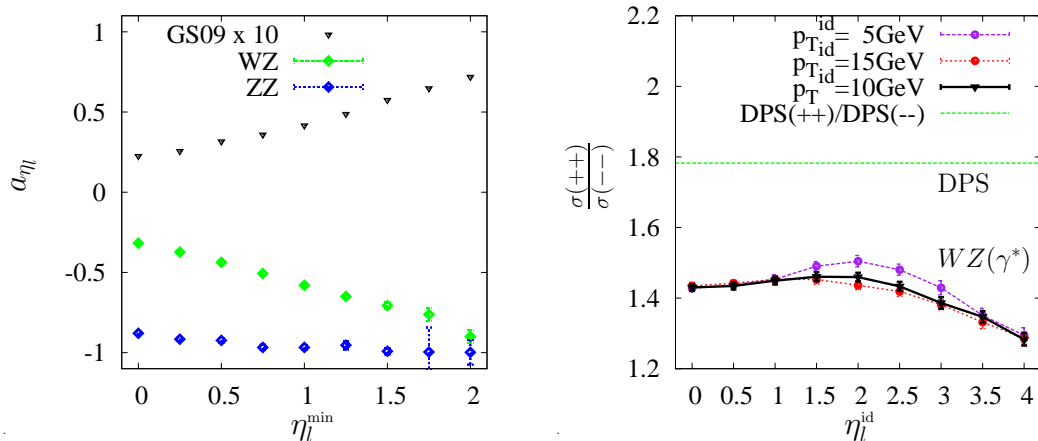
Fig. 50. Left: pseudorapidity asymmetry a_{η_l} for the positive SSDL+$\not{E}_T$ DPS signal and selected SPS background, after imposing cuts described in the text. Right: charge asymmetry ratio $(++)/(--)$ as a function of lepton identification criteria for different processes.

$Z + nj$ production probes initial state parton combinations which are different from those probed in $W^{\pm}W^{\pm}$ processes. The latter, at lowest order, are always initiated by four–fermion states, mainly $u\bar{d}u\bar{d}$. The former, on the contrary, typically have at least two gluons in the initial state since the largest component [167,168] involves a two jet process which is dominated by gluon–gluon scattering.

For comparison we also present the predictions for $\gamma + 3j$ production, the reaction from which the most recent and precise estimates of σ_{eff} have been extracted at the Tevatron. The CDF collaboration [2,3] has measured $\sigma_{eff} = 14.5 \pm 1.7^{+1.7}_{-2.3}$ mb, a value confirmed by D0 which quotes $\sigma_{eff} = 15.1 \pm 1.9$ mb [4]. In Ref. [79] it is argued, on the basis of the simplest two channel eikonal model for the proton–proton cross section, that a more appropriate value at $\sqrt{s} = 1.8$ TeV is 10 mb which translates at the LHC into $\sigma_{eff}^{LHC} = 12$ mb. Treleani then estimates the effect of the removal by CDF of triple parton interactions (TPI) events from their sample and concludes that the CDF measurement yields $\sigma_{eff} \approx 11$ mb at Tevatron energies. In the following we use $\sigma_{eff} = 12.0$ mb for all LHC center of mass energies, with the understanding that this value is affected by an experimental uncertainty of about 15% and that it agrees only within 30% with the predictions of the eikonal model. Since σ_{eff} appears as an overall factor in our results it is easy to take into account a different value.

It is worth mentioning that at present there is a discrepancy between the value of σ_{eff} extracted by CDF and D0 and the one which is effectively employed by PYTHIA whose normalization is derived mainly from comparisons with small p_T data which dominate the total cross section. The description of MPI in PYTHIA 8 [56] assumes that interactions can occur at different p_T values independently of each other inside inelastic non–diffractive events. The expression for a DPS cross section, here referred to as Double Parton Interactions (DPI) cross section, becomes therefore:

$$\sigma = <f_{impact}> \sigma_1 \cdot \sigma_2 / \sigma_{ND} / k \tag{76}$$

where σ_{ND} is the total non–diffractive cross section and f_{impact} is an enhancement/depletion factor chosen event-by-event to account for correlations introduced by the centrality of the collision. This quantity is typically averaged during an entire run to calculate $< f_{impact} >$ in Eq. 76. Typical values at the center of mass energy of 10 TeV are 1.33 for $< f_{impact} >$ and 51.6 mb for σ_{ND}. Comparing Eq. 76 with Eq. 65 tells us that PYTHIA 8 predicts an effective $\sigma_{eff} = \sigma_{ND}/< f_{impact} >$ which is about a factor three larger than the one actually measured at the Tevatron. I believe that this issue deserves careful consideration and that new measurements of high p_T MPI reactions would be quite welcome.

NLO QCD corrections are or will soon be available for all SPS, here referred to as Single Parton Interactions (SPI) processes leading to an electroweak vector boson in association with up to four jets [169,170,171,172,173,174,175,176]. The Drell-Yan cross section is known at NNLO [177]. Measurements at the Tevatron show good agreement between NLO calculations and data [178,179]. These new developments open the possibility of validating the predictions using events with large visible energy, where the MPI contribution is small, and then using them for a direct measurement of the MPI cross section at smaller total invariant masses in parallel with more data driven analysis similar to those of CDF and D0.

In the following we compare the results obtained with the GS09 dPDF with those obtained with two instances of fully factorized sPDF: MSTW2008LO [118] and CTEQ6L1 [40]. Hence we can estimate, even in the absence of a

proper dPDF set based on CTEQ6, the dependence of MPI predictions on the choice of PDF, a study that to our knowledge has not been performed before.

The MPI processes which contribute at leading order to $Z + n$–jets through Double Parton Interactions are those in which an event producing k jets is superimposed to an event producing a Z–boson and $(n - k)$ jets, $k = 2, \ldots, n$.

All samples have been generated with the following cuts:

$$
\begin{aligned}
p_{T_j} &\geq 30 \text{ GeV}, \quad |\eta_j| \leq 5.0, \\
p_{T_\ell} &\geq 20 \text{ GeV}, \quad |\eta_\ell| \leq 2.5, \\
p_{T_\gamma} &\geq 30 \text{ GeV}, \quad |\eta_\gamma| \leq 2.5, \\
\Delta R_{jj} &\geq 0.5, \quad \Delta R_{jl} \geq 0.1, \quad \Delta R_{j\gamma} \geq 0.1
\end{aligned}
\tag{77}
$$

where $j = u, \bar{u}, d, \bar{d}, s, \bar{s}, c, \bar{c}, b, \bar{b}, g$ and $l = e^+, e^-, \mu^-, \mu^+$.

The $Z+4$–jets sample has been generated with PHANTOM [180,181,182], while all other samples have been produced with MADVENT [183,184]. All samples have been generated using CTEQ6L1 [185] parton distribution functions. The QCD scale (both in α_s and in the parton distribution functions) has been taken as

$$
Q^2 = \sum_{i=1}^{n} p_{Ti}^2,
\tag{78}
$$

where n is the number of final state partons, for all reactions with the exception of $q\bar{q} \to l^+l^-$ for which the scale has been set at $Q^2 = M_Z^2$.

The results shown in the following under the CTEQ heading have been obtained combining at random one event from each of the reactions which together produce the desired final state through MPI.

The results shown under the MSTW and GS09 headings have been obtained through a reweighting procedure by the appropriate ratio of parton distribution functions and coupling constants. For instance, an event like $(q_i\bar{q}_i \to gl^+l^-) \otimes (gg \to gg)$, constructed from two events generated separately with CTEQ6 PDF, can be transformed in a weighted event with MSTW2008 PDF multiplying its original weight by

$$
R = \frac{D_i^{MSTW}(t_1)D_{\bar{i}}^{MSTW}(t_1)}{D_i^{CTEQ}(t_1)D_{\bar{i}}^{CTEQ}(t_1)} \times \frac{\alpha_s^{MSTW}(t_1)}{\alpha_s^{CTEQ}(t_1)} \times \frac{D_g^{MSTW}(t_2)D_g^{MSTW}(t_2)}{D_g^{CTEQ}(t_2)D_g^{CTEQ}(t_2)} \times \frac{\alpha_s^{MSTW}(t_2)^2}{\alpha_s^{CTEQ}(t_2)^2}
\tag{79}
$$

where t_1, t_2 are the factorization scales for $q_i\bar{q}_i \to gl^+l^-$ and $gg \to gg$ respectively. The factorization scales have been read off from the event files. The second and fourth factors in Eq.(79) take into account the different values of the strong coupling constants for the two different sets of PDF: $\alpha_{s,LO}^{CTEQ}(M_Z) = 0.130$ while $\alpha_{s,LO}^{MRST}(M_Z) = \alpha_s^{GS09}(M_Z) = 0.139$. The only difference for the GS09 case would be that the correlated dPDF $F_{ij}(t_1, t_2)$ would appear instead of the uncorrelated product $D_i(t_1)D_j(t_2)$ and so on.

All results are obtained with the following values for the electroweak input parameters: $M_Z = 91.188$ GeV, $M_W = 80.40$ GeV, $G_F = 0.116639 \times 10^{-5}$ GeV^{-2}.

The total cross sections for SPI and DPI production for $Z + 2$–jets, $Z + 3$–jets and $Z + 4$–jets are presented in Table 5. In our estimates below we have only taken into account the muon decay of the Z boson.

	14 TeV			10 TeV			7 TeV		
	CTEQ	MSTW	GS09	CTEQ	MSTW	GS09	CTEQ	MSTW	GS09
	$Z + 2j$								
SPI	52.65	60.70		30.63	35.15		16.56	18.88	
DPI	11.27	14.37	15.50	4.80	6.35	6.68	1.88	2.61	2.66
	$Z + 3j$								
SPI	15.71	19.10		8.46	10.23		4.11	4.93	
DPI	2.70	3.75	3.88	1.02	1.49	1.48	0.34	0.54	0.51
	$Z + 4j$								
SPI	4.26	5.41		2.00	2.53		0.83	1.04	
DPI	0.96	1.53	1.50	0.33	0.56	0.52	0.10	0.18	0.16

Table 5. $Z + n$–jets, $Z \to \mu^+\mu^-$ cross sections in pb. Cuts as in Eq.(77) with $\Delta R_{jj} = 0.5$.

The total cross sections for SPI and DPI production for $\gamma + 3$–jets are shown in Table 6. At the LHC trigger thresholds for single photons are foreseen to be much higher than those for double leptons [186,187,188]. While pair

of leptons are expected to be triggered on for transverse momenta of about 15 GeV, single photons will be detected only when their transverse momenta is larger than about 80 GeV at the design energy of 14 TeV. Since MPI processes are known to decrease sharply with increasing transverse momenta, we present also the predictions for $p_{T_\gamma} \geq 80$ GeV.

The Single Particle Interaction MSTW results are larger than those obtained with the CTEQ PDF by an amount which varies between 15% for $Z+2j$ to 27% for $Z+4j$, increasing as expected with the power of α_s in the amplitude. The Double Particle Interaction MSTW results are larger than those obtained with the CTEQ PDF by an amount which varies between 30% and 90%. The larger shift is due to the smaller scales for the two individual scatterings compared to a single interaction event with the same final state particles. The predictions for the GS09 correlated dPDF are larger than those with MSTW uncorrelated ones for $\sqrt{s} = 14$ TeV and $\sqrt{s} = 10$ TeV while they are smaller for $\sqrt{s} = 7$ TeV. The difference is at most of 15%. Taking into account the errors in the measurement of σ_{eff} we conclude that the uncertainties due to the choice of PDF and to correlation effects are reasonably under control.

These variations should be compared with the uncertainty due to scale variation in PDF and in the strong coupling constant. Changing the scale in Eq.(78) by a factor of two in either direction for two limiting cases, namely $Z+2j$ production at $\sqrt{s} = 7$ TeV and $Z+4j$ production at $\sqrt{s} = 14$ TeV the cross section changes by +14%/-13% in the first case and by +57%/-29% in the second.

The effects of higher order corrections are more difficult to estimate since no NLO calculation for MPI processes is available. QCD one loop calculations are available for vector boson production with up to four jets and are typically of order 10% with the exception of Drell–Yan inclusive production where they are of the order of 50%. NLO corrections for the inclusive jet cross section at the LHC have been presented in Ref. [189]. For small transverse momenta, as the ones we are interested in this paper, they are of the order of 10%.

The ratio between the MPI and SPI cross sections increases with the collider energy, that is with decreasing average momentum fractions carried by the incoming partons. It also increases with the ΔR_{jj} separation because of the absence of correlations between the final state partons originating in the independent scatterings which compose MPI events. For $Z + nj$ processes and taking $\Delta R_{jj} = 0.5$ as an example, the ratio is of the order of 10% for $\sqrt{s} = 7$ TeV and grows to about 25% at $\sqrt{s} = 14$ TeV. The results for $\gamma + 3$–jets show a similar behaviour with somewhat smaller fractions of MPI events to SPI ones which however depend drastically on the p_{T_γ} cut. For $p_{T_\gamma} \geq 30$ GeV they range between 5 and 10% while for $p_{T_\gamma} \geq 80$ GeV they are at the percent level.

	14 TeV			10 TeV			7 TeV		
$\gamma + 3j$	CTEQ	MSTW	GS09	CTEQ	MSTW	GS09	CTEQ	MSTW	GS09
$p_{T_\gamma} \geq 30$ GeV									
SPI	4516.7	5610.2		2637.2	3263.8		1415.8	1744.6	
DPI	422.2	593.7	642.2	170.3	254.1	264.9	62.0	100.0	99.4
$p_{T_\gamma} \geq 80$ GeV									
SPI	671.5	813.0		368.30	443.38		177.4	212.0	
DPI	17.7	28.1	28.1	6.59	11.49	10.85	2.09	4.09	3.58

Table 6. $\gamma + 3$–jets cross sections in pb. Cuts as in Eq.(77).

If we consider the MPI processes as our signal and the SPI ones as the corresponding background, we can estimate the prospect of measuring MPI in a given final state from the standard $S/\sqrt{B}$ significance. Using for S the result obtained with GS09 PDF and for B the result for the MSTW set and assuming a luminosity of one inverse femtobarn at 7 TeV, the significancies extracted from Table 5, in the $Z \to \mu^+\mu^-$ channel alone, are 19/7/5 for $Z+2/3/4$ jets . The corresponding number of expected MPI events are 2600/500/160. Therefore it appears quite feasible to measure the MPI contribution to $Z+2/3/4$ jets already in the first phase of the LHC.

The significance of $\gamma + 3$–jets depends on the trigger strategies. If the threshold for single photon detection can be brought in the 30 GeV range then the much larger production rate, about ten times that of $Z(\mu\mu) + 2j$, provides the best opportunity for an early measurement of MPI at the LHC. If, on the contrary, the photon trigger cannot substantially deviate from about 80 GeV, $Z+2j$ production looks more promising than the $\gamma + 3$–jets channel whose significance becomes similar to that of $Z+3j$.

The contribution to the MPI $Z+n$–jets cross section due to two jet production in association to $Z+(n-2)$–jets processes is in all instances the largest one, therefore, even with more than two jets in the final state, the majority of MPI events are expected to contain a pair of jets which are back to back in the transverse plane. This is confirmed by the left hand side of Fig. 51 which displays the distribution of the angular separation $\Delta\phi$ between the two highest p_T jets in $Z+4j$ events at $\sqrt{s} = 7$ TeV and $\Delta R_{jj} = 0.7$.

The right hand side of Fig. 51 presents the total visible mass distribution in $Z+2j$ production with the same energy and angular separation. It clearly shows that MPI events are produced with a smaller center of mass energy than SPI ones.
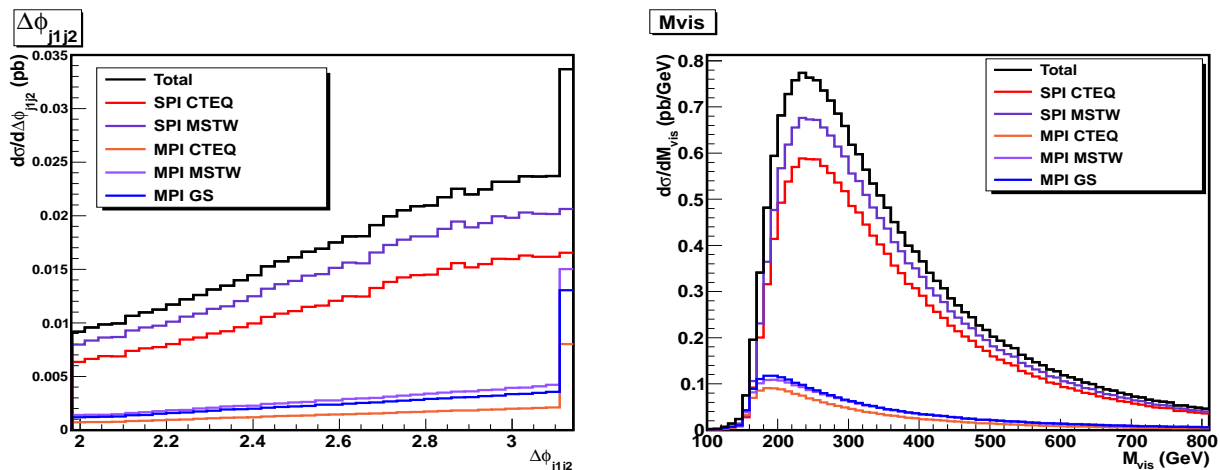
Fig. 51. On the left: distribution of the angular separation in the transverse plane between the two highest p_T jets in $Z + 4j$ events. On the right: distribution of the total visible mass, $(\sum_{i=1}^{n} p_i)^2$, in $Z + 2j$ events. For both plots $\sqrt{s} = 7$ TeV, $\Delta R_{jj} = 0.7$.

6 Summary and Outlook

The understanding multi-parton interactions (MPI) in hadronic collisions remains a challenge. Traditionally, research has concentrated on four tasks covered during this workshop: experimental measurements of underlying events and minimum bias events, models of soft physics implemented in Monte Carlo (MC) generators, development of the theoretical description of MPI, and phenomenological studies. In particular, a lot of effort, strongly driven by the experimental measurements, reported here by the ATLAS, CMS and LHCb collaborations, see Sections 2.1, 2.2, 2.3, respectively, focuses on modeling of minimum bias and underlying event physics in MC generators. This is, of course, only natural and very much needed given that the MC generators are major tools used in the experimental analyses by the LHC collaborations. In fact, one of the main tasks in LHC phenomenology is the construction and development of general purpose MC generator fully able to describe exclusive states, including contributions from MPI. This task has enormous importance for the overall success of the LHC physics programme. However, in order to improve the simulation of the MPI in the MC codes, more elaborate theoretical input, supplemented by information from high-p_T phenomenological studies, is necessary.

The standard MC algorithms are based on the factorization theorem and the factorization of the QCD amplitudes. This theorem lets us to define general algorithms and leads to good predictions for the LHC. However, the extension of the single interaction picture to encompass MPI is not a simple task. The main challenge is to understand the structure and the topology of the MPI based on perturbative QCD, as discussed by D. Treleani in Section 4.4. Two important issues can be identified: the treatment of the parton distributions and the parton dynamics.

The presence of multiple interacting partons in the initial state enforces the appearance multi parton distribution functions (mPDF). In the MC programs the mPDF functions are simple scalar functions, resulting from approximating a mPDF function with n partons by a product of single PDF functions. This is a good approximation under the assumption that the correlations in colour, spin and flavour can be neglected, as the most important information about the mPDF in the parton shower context comes from their evolution. Deficiencies in the approximation of the initial-state mPDF reached after backward evolution can be compensated through changes (tuning) in the hadronization.

In the current MC implementations the evolution of the multiple partons taking part in the same collision relies on well understood evolution equations for single PDF. Going beyond this approximation and moving to full mPDF evolution poses many challenges. The evolution equation for mPDF scalar functions has been available for some time. Recently, J. R. Gaunt and W. J. Stirling, cf. Section 4.3, provided a solution and detailed studies for the double parton case. However, the question of how double parton distributions should be defined and which evolution equation they satisfy has been reconsidered since the workshop, see [95,190,191]. Moreover, it is not clear whether the mPDF functions should be scalar functions or operators in color, spin and flavor space. As M. Diehl has pointed out in section 4.1, the non-trivial color, spin and flavor correlations occur in the dPDF case and they can be as important as the uncorrelated contributions. For example, non-trivial correlations in colour space can lead to similar effects as those caused by colour reconnection in the hadronization model. These issues would have to be resolved in order to achieve proper description of mPDF in MC generators.

The other important ingredient in the MC models is the treatment of the parton dynamics. Initial and final state radiation is well understood in the standard parton shower models, but the MPI contributions are more complex. HERWIG++ (cf. Section 3.2) follows a rather minimalistic approach and considers MPI effects only via the $2 \rightarrow 2$

parton interactions while PYTHIA studies also effects of rescattering and joint interaction in the MPI models, see Section 3.1. These contributions are considered in a classical probabilistic framework. To better understand and improve the existing models it is important to look beyond the existing approach. In perturbative parton dynamics there are usually two types of contributions. The first type is *real* radiation, when one or more partons appear in the final state, and the partons are resolvable. These contributions can be described by a rather simple splitting function (operator) that can be obtained from tree level Feynman graphs. The other contributions are the *virtual* and *unresolvable* configurations which are not considered explicitly but are included via unitary conditions. Usually, the splitting operator of virtual contributions has some imaginary part that cannot be obtained from the unitary conditions and thus is not taken into account in the current MC implementations. Such imaginary contributions, known in the literature as the Coulomb gluon terms, can lead to the appearance of the so-called super leading logarithms in perturbative calculations for certain quantities. Correspondingly, these effects cannot be reproduced by the existing parton shower MC codes. Since the imaginary part of the virtual splitting operator can change the colour structure, its effect might be similar in the colour space to the action of colour reconnection. It has been pointed out that colour reconnection, contributing to hadronization, can have a big impact on the predictions, and therefore is important for description of data. Consequently, one should systematically consider all the effects of perturbative origin, e.g. the colour-changing effects, in order to ensure the universality of the non-perturbative hadronization model.

It is often said that a good MC program has tunable parameters only in the hadronization model. This is more or less is true if we do not have to consider MPI effects, otherwise we need to deal with mPDF which have transverse momentum dependence. Unfortunately, we have very little information on the transverse momentum dependence. The standard practice is to assume the factorization of the longitudinal and transverse dependent parts of the mPDF. In the MC generators, the transverse momentum dependent part is described and parametrized by a simple function for every parton flavour. HERWIG++ makes use of only three tunable parameters while PYTHIA has more complicated parametrization with more parameters. This tunable function describes non-perturbative effects, and it can be shown that the average number of the interactions strongly depends on it. In principle we know very little about goodness of the factorization assumption. Theoretical studies, based on modeling the proton substructure by a dipole cascade model discussed by G. Gustafson in Section 4.5, show that the transverse part has a non-trivial dependence on the longitudinal momentum fraction of the incoming parton and the factorization scale. At this point, phenomenological studies of DPS processes with high p_T final states have an important role to play, as comparisons with experimental results will serve to test the predictions and uncover further information on the transverse momentum dependence of the mPDF.

The DPS measurements will also provide an important validation procedure of the MPI models built into MC generators. For this purpose, one needs to identify the processes where the DPS signal is favourable over SPS background. Promising candidate processes such as same-sign W production, Z production in association with jets, four-jet production or production of a $b\bar{b}$ pair with two jets have been discussed in previous chapters. As pointed out by E. Maina in Section 5.3, measuring DPS in different processes, for example in $Z + jets$ and $W^{\pm}W^{\pm}$ production, will deliver complementary information since different initial state parton combinations will be probed. It is also important to study if one can define quantities more sensitive to DPS than the ones measured currently. Two examples of such studies for $b\bar{b}$ pair plus two jet production and $pp \to Wb\bar{b}X \to \ell\nu b\bar{b}X$ were presented by E. Berger, see Section 5.1. Alternatively, kinematical regions where the DPS provides the dominant signal can be selected. As reported by B. Blok, cf. Section 4.2, in the case of four-jet production such region is constituted by back-to-back dijet production. For gauge boson pair production, the relevant region is where the transverse momentum of each boson is small, as shown in Section 4.1. It has to be also checked that the background to the actual final state observed experimentally can be sufficiently suppressed, cf. same-sign lepton final states discussed by C.-H. Kom in Section 5.2.

In summary, understanding MPI in hadronic collisions requires further efforts on both theoretical and experimental fronts. In particular, it would be helpful to critically reevaluate the description of MPI in MC codes and the tuning strategies. Although comparing results provided by existing MC codes supplemented with various tunes is certainly valuable on its own, there is a serious risk that it will not bring full understanding of the limitations and the systematic errors of MC generators. Apart from purely theoretical work and the work related to development of MC codes, it would be advantageous to, for example, identify and explore phase-space regions sensitive to MPI effects, other than those used so far in the experimental studies. Furthermore, one would also benefit from constructing new variables probing MPI in particular processes. As already stressed, such efforts need to be undertaken in common by the experimental and theoretical communities.

References

1. **Axial Field Spectrometer** Collaboration, T. Akesson *et. al.*, *Double parton scattering in p p collisions at $\sqrt{S} = 63$ GeV*, *Z. Phys.* **C34** (1987) 163.
2. **CDF** Collaboration, F. Abe *et. al.*, *Measurement of double parton scattering in anti-p p collisions at $\sqrt{s} = 1.8$ TeV*, *Phys. Rev. Lett.* **79** (1997) 584–589.
3. **CDF** Collaboration, F. Abe *et. al.*, *Double parton scattering in anti-p p collisions at $\sqrt{s} = 1.8$ TeV*, *Phys. Rev.* **D56** (1997) 3811–3832.
4. **D0** Collaboration, V. M. Abazov *et. al.*, *Double parton interactions in photon+3 jet events in p $\bar{p}$ collisions $\sqrt{s}$=1.96 TeV*, *Phys. Rev.* **D81** (2010) 052012, [arXiv:0912.5104].
5. **CDF** Collaboration, D. E. Acosta *et. al.*, *The Underlying event in hard interactions at the Tevatron anti-p p collider*, *Phys. Rev.* **D70** (2004) 072002, [hep-ex/0404004].
6. **CDF** Collaboration, T. Aaltonen *et. al.*, *Studying the Underlying Event in Drell-Yan and High Transverse Momentum Jet Production at the Tevatron*, *Phys. Rev.* **D82** (2010) 034001, [arXiv:1003.3146].
7. **CMS** Collaboration, V. Khachatryan *et. al.*, *Measurement of the Underlying Event Activity in Proton- Proton Collisions at 0.9 TeV*, *Eur. Phys. J.* **C70** (2010) 555–572, [arXiv:1006.2083].
8. T. Sjostrand and M. van Zijl, *A multiple-interaction model for the event structure in hadron collisions*, *Phys. Rev.* **D36** (1987) 2019.
9. T. Sjostrand and P. Z. Skands, *Multiple interactions and the structure of beam remnants*, *JHEP* **03** (2004) 053, [hep-ph/0402078].
10. T. Sjöstrand and P. Z. Skands, *Transverse-momentum-ordered showers and interleaved multiple interactions*, *Eur. Phys. J.* **C39** (2005) 129–154, [hep-ph/0408302].
11. J. M. Butterworth, J. R. Forshaw, and M. H. Seymour, *Multiparton interactions in photoproduction at HERA*, *Z. Phys.* **C72** (1996) 637–646, [hep-ph/9601371].
12. M. Bahr, S. Gieseke, and M. H. Seymour, *Simulation of multiple partonic interactions in Herwig++*, *JHEP* **07** (2008) 076, [arXiv:0803.3633].
13. P. Bartalini, ed., *Proceedings of the First International Workshop on Multiple Partonic Interactions at the LHC (MPI08)*, 2010.
14. **ATLAS** Collaboration, G. Aad *et. al.*, *Measurement of underlying event characteristics using charged particles in pp collisions at $\sqrt{s} = 900$GeV and 7 TeV with the ATLAS detector*, arXiv:1012.0791.
15. T. Sjöstrand, S. Mrenna, and P. Skands, *PYTHIA 6.4 physics and manual*, *JHEP* **05** (2006) 026, [hep-ph/0603175].
16. **ATLAS** Collaboration, *ATLAS Monte Carlo tunes for MC09*, Tech. Rep. ATL-PHYS-PUB-2010-002, CERN, Geneva, Mar, 2010.
17. R. Field, "Min-bias and the underlying event at the Tevatron and the LHC." A talk presented at the Fermilab MC Tuning Workshop, Fermilab, 2002.
18. P. Z. Skands, *The Perugia Tunes*, arXiv:0905.3418.
19. G. Corcella *et. al.*, *HERWIG 6.5 release note*, hep-ph/0210213.
20. R. Engel, *Photoproduction within the two component dual parton model. 1. Amplitudes and cross-sections*, *Z. Phys.* **C66** (1995) 203–214.
21. R. Field, "Early QCD measurements at the LHC." A talk presented at LHC@BNL: Joint Theory/Experiment Workshop on Early Physics at the LHC, BNL, 2010.
22. **ATLAS** Collaboration, *Angular correlations between charged particles from proton-proton collisions at sqrts = 900 gev and sqrts = 7 tev measured with atlas detector*, Tech. Rep. ATLAS-CONF-2010-082, CERN, Geneva, Oct, 2010.
23. **ATLAS** Collaboration, *Charged particle multiplicities in p p interactions at $\sqrt{s} = 0.9$ and 7 tev in a diffractive limited phase-space measured with the atlas detector at the lhc and new pythia6 tune*, Tech. Rep. ATLAS-CONF-2010-031, CERN, Geneva, Jul, 2010.
24. **ATLAS** Collaboration, *First tuning of HERWIG/JIMMY to ATLAS data*, Tech. Rep. ATL-PHYS-PUB-2010-014, CERN, Geneva, Oct, 2010.
25. **CMS** Collaboration, R. Adolphi *et. al.*, *The CMS experiment at the CERN LHC*, *JINST* **3** (2008) S08004.
26. G. D'Agostini, *A Multidimensional unfolding method based on Bayes' theorem*, *Nucl.Instrum.Meth.* **A362** (1995) 487–498.
27. T. Sjostrand and M. van Zijl, *Multiple parton-parton interactions in an impact parameter picture*, *Phys. Lett.* **B188** (1987) 149.
28. T. Sjostrand, *PYTHIA 8 Status Report*, arXiv:0809.0303.
29. R. Corke, *Multiple Interactions in PYTHIA 8*, arXiv:0901.2852.
30. F. W. Bopp, R. Engel, and J. Ranft, *Rapidity gaps and the PHOJET Monte Carlo*, hep-ph/9803437.
31. R. Field, *Physics at the Tevatron*, *Acta Phys. Polon.* **B39** (2008) 2611–2672.

32. P. Z. Skands, *Tuning Monte Carlo Generators: The Perugia Tunes*, Phys. Rev. **D82** (2010) 074018, [`arXiv:1005.3457`].

33. R. Field, *Early LHC Underlying Event Data - Findings and Surprises*, `arXiv:1010.3558`.

34. P. Z. Skands and D. Wicke, *Non-perturbative QCD effects and the top mass at the Tevatron*, Eur. Phys. J. **C52** (2007) 133–140, [`hep-ph/0703081`].

35. A. Buckley, H. Hoeth, H. Lacker, H. Schulz, and J. E. von Seggern, *Systematic event generator tuning for the LHC*, Eur. Phys. J. **C65** (2010) 331–357, [`arXiv:0907.2973`].

36. **ATLAS** Collaboration, G. Aad *et. al.*, *Charged-particle multiplicities in pp interactions measured with the atlas detector at the lhc*, New J. Phys. **13** (2011) 053033, [`arXiv:1012.5104`].

37. **CMS** Collaboration, *Measurement of the Underlying Event Activity at the LHC with $\sqrt{s}$=7 TeV and Comparison with $\sqrt{s}$=0.9 TeV*, Tech. Rep. CMS PAS QCD 10-010, CERN, 2010.

38. S. Navin, *Diffraction in Pythia*, `arXiv:1005.3894`.

39. **CTEQ** Collaboration, H. L. Lai *et al.*, *Global QCD analysis of parton structure of the nucleon: CTEQ5 parton distributions*, Eur. Phys. J. **C12** (2000) 375–392, [`hep-ph/9903282`].

40. J. Pumplin *et. al.*, *New generation of parton distributions with uncertainties from global QCD analysis*, JHEP **07** (2002) 012, [`hep-ph/0201195`].

41. G. P. Salam and G. Soyez, *A practical Seedless Infrared-Safe Cone jet algorithm*, JHEP **05** (2007) 086, [`arXiv:0704.0292`].

42. M. Cacciari, G. P. Salam, and G. Soyez, *The anti-k_t jet clustering algorithm*, JHEP **04** (2008) 063, [`arXiv:0802.1189`].

43. M. Cacciari, G. P. Salam, and S. Sapeta, *On the characterisation of the underlying event*, JHEP **04** (2010) 065, [`arXiv:0912.4926`].

44. **CMS** Collaboration, *Measurement of the Underlying Event Activity with the Jet Area/Median Approach at 0.9 TeV*, Tech. Rep. CMS PAS QCD 10-005, CERN, 2010.

45. **CDF** Collaboration, A. A. Affolder *et. al.*, *Charged jet evolution and the underlying event in proton - anti-proton collisions at 1.8-TeV*, Phys. Rev. **D65** (2002) 092002.

46. **CMS** Collaboration, *Measurement of the energy flow in the forward region at the LHC*, Tech. Rep. CMS PAS FWD 10-002, CERN, 2010.

47. N. Paver and D. Treleani, *Multi - quark scattering and large p(t) jet production in hadronic collisions*, Nuovo Cim. **A70** (1982) 215.

48. G. Calucci and D. Treleani, *Mini - jets and the two-body parton correlation*, Phys. Rev. **D57** (1998) 503–511, [`hep-ph/9707389`].

49. **UA2** Collaboration, J. Alitti *et. al.*, *A Study of multi - jet events at the CERN anti-p p collider and a search for double parton scattering*, Phys. Lett. **B268** (1991) 145–154.

50. **CDF** Collaboration, F. Abe *et. al.*, *Study of four jet events and evidence for double parton interactions in p anti-p collisions at $\sqrt{s}$ = 1.8 TeV*, Phys. Rev. **D47** (1993) 4857–4871.

51. G. Calucci and D. Treleani, *Inclusive and ' exclusive ' cross sections in the regime of multiple parton collisions*, Phys. Rev. **D79** (2009) 034002, [`arXiv:0809.4217`].

52. M. Bahr *et. al.*, *Herwig++ Physics and Manual*, Eur. Phys. J. **C58** (2008) 639–707, [`arXiv:0803.0883`].

53. **LHCb** Collaboration, A. A. Alves *et. al.*, *The LHCb Detector at the LHC*, JINST **3** (2008) S08005.

54. **LHCb Collaboration** Collaboration, R. Aaij *et. al.*, *Prompt K_{short} production in pp collisions at sqrt(s)=0.9 TeV*, Phys.Lett. **B693** (2010) 69–80, [`arXiv:1008.3105`].

55. T. Sjöstrand, "PYTHIA webpage." http://home.thep.lu.se/ torbjorn/Pythia.html.

56. T. Sjöstrand, S. Mrenna, and P. Skands, *A Brief Introduction to PYTHIA 8.1*, Comput. Phys. Commun. **178** (2008) 852–867, [`arXiv:0710.3820`].

57. **CDF** Collaboration, R. D. Field, *The underlying event in hard scattering processes*, `hep-ph/0201192`.

58. N. Paver and D. Treleani, *Multiple parton interactions and multi-jet events at collider and Tevatron energies*, Phys. Lett. **B146** (1984) 252.

59. R. Corke and T. Sjöstrand, *Multiparton Interactions and Rescattering*, JHEP **01** (2010) 035, [`arXiv:0911.1909`].

60. R. Corke and T. Sjostrand, *Interleaved Parton Showers and Tuning Prospects*, `arXiv:1011.1759`.

61. A. Sherstnev and R. S. Thorne, *Parton Distributions for LO Generators*, Eur. Phys. J. **C55** (2008) 553–575, [`arXiv:0711.2473`].

62. A. Buckley *et. al.*, *Rivet user manual*, `arXiv:1003.0694`.

63. **CDF** Collaboration, D. E. Acosta *et. al.*, *Soft and hard interactions in p$\bar{p}$ collisions at $\sqrt{s}$ = 1800 GeV and 630 GeV*, Phys. Rev. **D65** (2002) 072005.

64. **ATLAS** Collaboration, A. Collaboration, *Studies of diffractive enhanced minimum bias events in atlas*, . ATLAS-CONF-2010-048 (2010).

65. **ATLAS** Collaboration, G. Aad *et. al.*, *Charged-particle multiplicities in pp interactions at sqrt(s) = 900 GeV measured with the ATLAS detector at the LHC*, Phys. Lett. **B688** (2010) 21–42, [`arXiv:1003.3124`].

66. **ATLAS** Collaboration, A. Collaboration, *Charged particle multiplicities in pp interactions at $\sqrt{s}$ = 7 tev measured with the ATLAS detector at the LHC*, . ATLAS-CONF-2010-024.

67. **ATLAS** Collaboration, A. Collaboration, *Track-based underlying event measurements in pp collisions at $\sqrt{s}$ = 900 gev and 7 tev with the ATLAS Detector at the LHC*, . ATLAS-CONF-2010-029 (2010).

68. A. Donnachie and P. V. Landshoff, *Total cross-sections*, Phys. Lett. **B296** (1992) 227–232, [`hep-ph/9209205`].

69. I. Borozan and M. H. Seymour, *An Eikonal model for multiparticle production in hadron hadron interactions*, *JHEP* **09** (2002) 015, [`hep-ph/0207283`].

70. M. Bahr, J. M. Butterworth, and M. H. Seymour, *The Underlying Event and the Total Cross Section from Tevatron to the LHC*, *JHEP* **01** (2009) 065, [`arXiv:0806.2949`].

71. M. Bahr, J. M. Butterworth, S. Gieseke, and M. H. Seymour, *Soft interactions in Herwig++*, `arXiv:0905.4671`.

72. S. Gieseke *et. al.*, *Herwig++ 2.5 Release Note*, `arXiv:1102.1672`.

73. P. V. Landshoff and J. C. Polkinghorne, *Calorimeter triggers for hard collisions*, *Phys. Rev.* **D18** (1978) 3344.

74. F. Takagi, *Multiple production of quark jets off nuclei*, *Phys. Rev. Lett.* **43** (1979) 1296.

75. C. Goebel, F. Halzen, and D. M. Scott, *Double Drell-Yan annihilations in hadron collisions: novel tests of the constituent picture*, *Phys. Rev.* **D22** (1980) 2789.

76. M. Mekhfi, *Correlations in color and spin in multiparton processes*, *Phys. Rev.* **D32** (1985) 2380.

77. A. M. Snigirev, *Double parton distributions in the leading logarithm approximation of perturbative QCD*, *Phys. Rev.* **D68** (2003) 114012, [`hep-ph/0304172`].

78. V. L. Korotkikh and A. M. Snigirev, *Double parton correlations versus factorized distributions*, *Phys. Lett.* **B594** (2004) 171–176, [`hep-ph/0404155`].

79. D. Treleani, *Double parton scattering, diffraction and effective cross section*, *Phys. Rev.* **D76** (2007) 076006, [`arXiv:0708.2603`].

80. G. Calucci and D. Treleani, *Multi-parton correlations and ' exclusive ' cross sections*, *Phys. Rev.* **D79** (2009) 074013, [`arXiv:0901.3089`].

81. G. Calucci and D. Treleani, *Incoherence and Multiple Parton Interactions*, *Phys. Rev.* **D80** (2009) 054025, [`arXiv:0907.4772`].

82. J. R. Gaunt and W. J. Stirling, *Double parton distributions incorporating perturbative qcd evolution and momentum and quark number sum rules*, `arXiv:0910.4347`.

83. A. M. Snigirev, *A Possible indication to the QCD evolution of double parton distributions?*, *Phys. Rev.* **D81** (2010) 065014, [`arXiv:1001.0104`].

84. G. Calucci and D. Treleani, *Disentangling correlations in Multiple Parton Interactions*, `arXiv:1009.5881`.

85. A. M. Snigirev, *Asymptotic behavior of double parton distribution functions*, `arXiv:1010.4874`.

86. M. Diehl, these proceedings.

87. J. C. Collins and D. E. Soper, *Back-To-Back Jets in QCD*, *Nucl. Phys.* **B193** (1981) 381.

88. X.-d. Ji, J.-p. Ma, and F. Yuan, *QCD factorization for semi-inclusive deep-inelastic scattering at low transverse momentum*, *Phys. Rev.* **D71** (2005) 034005, [`hep-ph/0404183`].

89. J. C. Collins, T. C. Rogers, and A. M. Stasto, *Fully Unintegrated Parton Correlation Functions and Factorization in Lowest Order Hard Scattering*, *Phys. Rev.* **D77** (2008) 085009, [`arXiv:0708.2833`].

90. J. Collins, *The Foundations of Perturbative QCD.* Cambridge University Press, 2011.

91. M. Hillery, R. O'Connell, M. Scully, and E. P. Wigner, *Distribution functions in physics: Fundamentals*, *Phys.Rept.* **106** (1984) 121–167.

92. M. Mekhfi, *Multiparton processes: an application to double Drell-Yan*, *Phys. Rev.* **D32** (1985) 2371.

93. R. Kirschner, *Generalized Lipatov-Altarelli-Parisi equations and jet calculus rules*, *Phys. Lett.* **B84** (1979) 266.

94. V. P. Shelest, A. M. Snigirev, and G. M. Zinovev, *The multiparton distribution equations in QCD*, *Phys. Lett.* **B113** (1982) 325.

95. M. Diehl and A. Schafer, *Theoretical considerations on multiparton interactions in QCD*, *Phys. Lett.* **B698** (2011) 389–402, [`arXiv:1102.3081`].

96. A. Del Fabbro and D. Treleani, *A double parton scattering background to Higgs boson production at the LHC*, *Phys. Rev.* **D61** (2000) 077502, [`hep-ph/9911358`].

97. N. Paver and D. Treleani, *Multiple parton processes in the TeV region*, *Z. Phys.* **C28** (1985) 187.

98. T. Sjöstrand and P. Skands, *Transverse-momentum-ordered showers and interleaved multiple interactions*, `hep-ph/0408302v1`.

99. M. Bahr, S. Gieseke, M. A. Gigg, D. Grellscheid, K. Hamilton, O. Latunde-Dada, S. Platzer, P. Richardson, M. H. Seymour, A. Sherstnev, J. Tully, and B. R. Webber, *Herwig++ physics and manual*, `arXiv:0803.0883`.

100. A. Del Fabbro and D. Treleani, *Scale factor in double parton collisions and parton densities in transverse space*, *Phys. Rev.* **D63** (2001) 057901, [`hep-ph/0005273`].

101. A. Accardi and D. Treleani, *Hard parton rescatterings and minijets in nuclear collisions at LHC*, *Phys. Rev.* **D63** (2001) 116002, [`hep-ph/0009234`].

102. L. Frankfurt, M. Strikman, and C. Weiss, *Dijet production as a centrality trigger for pp collisions at CERN LHC*, `hep-ph/0311231v2`.

103. L. Frankfurt, M. Strikman, and C. Weiss, *Small-x Physics: From HERA to LHC and beyond*, `hep-ph/0507286v1`.

104. L. Frankfurt, M. Strikman, D. Treleani, and C. Weiss, *Evidence for color fluctuations in the nucleon in high-energy scattering*, `arXiv:0808.0182`.

105. T. Rogers, A. Stasto, and M. I. Strikman, *Unitarity constraints on semi-hard jet production in impact parameter space*, `arXiv:0801.0303`.

106. S. Domdey, H.-J. Pirner, and U. A. Wiedemann, *Testing the Scale Dependence of the Scale Factor in Double Dijet Production at the LHC*, `arXiv:0906.4335`.

107. M. Diehl, *Multiple interactions and generalized parton distributions*, *PoS* **DIS2010** (2010) 223, [`arXiv:1007.5477`].

108. Y. L. Dokshitzer, D. Diakonov, and S. I. Troian, *Hard Processes in Quantum Chromodynamics*, *Phys. Rept.* **58** (1980) 269–395.

109. S. Catani, E. D'Emilio, and L. Trentadue, *The gluon form-factor to higher orders: gluon-gluon annihilation at small Q-transverse*, *Phys. Lett.* **B211** (1988) 335–342.

110. A. P. Bukhvostov, G. V. Frolov, L. N. Lipatov, and E. A. Kuraev, *Evolution Equations for Quasi-Partonic Operators*, *Nucl. Phys.* **B258** (1985) 601–646.

111. L. Frankfurt and M. Strikman, *Two-gluon form factor of the nucleon and J/psi photoproduction*, *Phys. Rev.* **D66** (2002) 031502, [`hep-ph/0205223`].

112. M. Strikman and C. Weiss, *Chiral dynamics and partonic structure at large transverse distances*, *Phys. Rev.* **D80** (2009) 114029, [`arXiv:0906.3267`].

113. M. Diehl, *Generalized parton distributions in impact parameter space*, *Eur. Phys. J.* **C25** (2002) 223–232, [`hep-ph/0205208`].

114. M. Diehl, *Generalized parton distributions*, *Phys. Rept.* **388** (2003) 41–277, [`hep-ph/0307382`].

115. J. R. Gaunt, C.-H. Kom, A. Kulesza, and W. J. Stirling, *Same-sign W pair production as a probe of double parton scattering at the LHC*, `arXiv:1003.3953`.

116. B. Blok, Y. Dokshitzer, L. Frankfurt, and M. Strikman, *The Four jet production at LHC and Tevatron in QCD*, `arXiv:1009.2714`.

117. http://projects.hepforge.org/gsdpdf.

118. A. D. Martin, W. J. Stirling, R. S. Thorne, and G. Watt, *Parton distributions for the LHC*, `arXiv:0901.0002`.

119. R. K. Ellis, W. J. Stirling, and B. R. Webber, *QCD and Collider Physics.* Cambridge University Press, 1996.

120. T. Binoth, M. Ciccolini, N. Kauer, and M. Kramer, *Gluon-induced W-boson pair production at the LHC*, *JHEP* **12** (2006) 046, [`hep-ph/0611170`].

121. E. W. N. Glover and J. J. van der Bij, *Z boson pair production via gluon fusion*, *Nucl. Phys.* **B321** (1989) 561.

122. **NLO Multileg Working Group** Collaboration, Z. Bern *et. al.*, *The NLO multileg working group: Summary report*, `arXiv:0803.0494`.

123. M. Strikman and D. Treleani, *Measuring double parton distributions in nucleons at proton nucleus colliders*, *Phys.Rev.Lett.* **88** (2002) 031801, [`hep-ph/0111468`].

124. E. Cattaruzza, A. Del Fabbro, and D. Treleani, *Heavy-quark production in proton-nucleus collisions at the LHC*, *Int.J.Mod.Phys.* **A20** (2005) 4462–4468.

125. T. C. Rogers, A. M. Stasto, and M. I. Strikman, *Unitarity Constraints on Semi-hard Jet Production in Impact Parameter Space*, *Phys. Rev.* **D77** (2008) 114009, [`arXiv:0801.0303`].

126. T. C. Rogers and M. Strikman, *Multiple Hard Partonic Collisions with Correlations in Proton-Proton Scattering*, *Phys. Rev.* **D81** (2010) 016013, [`arXiv:0908.0251`].

127. A. Bialas, M. Bleszynski, and W. Czyz, *Multiplicity Distributions in Nucleus-Nucleus Collisions at High-Energies*, *Nucl. Phys.* **B111** (1976) 461.

128. M. L. Good and W. D. Walker, *Diffraction disssociation of beam particles*, *Phys. Rev.* **120** (1960) 1857–1860.

129. A. H. Mueller, *O(2,1) analysis of single particle spectra at high-energy*, *Phys. Rev.* **D2** (1970) 2963–2968.

130. C. E. DeTar *et. al.*, *Helicity poles, triple-regge behavior, and single-particle spectra in high-energy collisions*, *Phys. Rev. Lett.* **26** (1971) 675–676.

131. M. G. Ryskin, A. D. Martin, and V. A. Khoze, *Soft processes at the LHC, I: Multi-component model*, *Eur. Phys. J.* **C60** (2009) 249–264, [`arXiv:0812.2407`].

132. A. B. Kaidalov and M. G. Poghosyan, *Description of soft diffraction in the framework of reggeon calculus. Predictions for LHC*, `arXiv:0909.5156`.

133. E. Gotsman, E. Levin, U. Maor, and J. S. Miller, *A QCD motivated model for soft interactions at high energies*, *Eur. Phys. J.* **C57** (2008) 689–709, [`arXiv:0805.2799`].

134. A. H. Mueller and G. P. Salam, *Large multiplicity fluctuations and saturation effects in onium collisions*, *Nucl. Phys.* **B475** (1996) 293–320, [`hep-ph/9605302`].

135. E. Avsar, G. Gustafson, and L. Lonnblad, *Diffractive excitation in DIS and pp collisions*, *JHEP* **12** (2007) 012, [`arXiv:0709.1368`].

136. C. Flensburg and G. Gustafson, *Fluctuations, Saturation, and Diffractive Excitation in High Energy Collisions*, *JHEP* **10** (2010) 014, [`arXiv:1004.5502`].

137. A. H. Mueller, *Soft gluons in the infinite momentum wave function and the BFKL pomeron*, *Nucl. Phys.* **B415** (1994) 373–385.

138. A. H. Mueller and B. Patel, *Single and double BFKL pomeron exchange and a dipole picture of high-energy hard processes*, *Nucl. Phys.* **B425** (1994) 471–488, [`hep-ph/9403256`].

139. A. H. Mueller, *Unitarity and the BFKL pomeron*, *Nucl. Phys.* **B437** (1995) 107–126, [`hep-ph/9408245`].

140. E. Avsar, G. Gustafson, and L. Lonnblad, *Energy conservation and saturation in small-x evolution*, *JHEP* **07** (2005) 062, [`hep-ph/0503181`].

141. E. Avsar, G. Gustafson, and L. Lonnblad, *Small-x dipole evolution beyond the large-N(c) limit*, *JHEP* **01** (2007) 012, [`hep-ph/0610157`].

142. C. Flensburg, G. Gustafson, and L. Lonnblad, *Elastic and quasi-elastic pp and gamma* p scattering in the Dipole Model*, *Eur. Phys. J.* **C60** (2009) 233–247, [`arXiv:0807.0325`].

143. H. I. Miettinen and J. Pumplin, *Diffraction Scattering and the Parton Structure of Hadrons*, *Phys. Rev.* **D18** (1978) 1696.

144. L. N. Lipatov, *The Bare Pomeron in Quantum Chromodynamics*, *Sov. Phys. JETP* **63** (1986) 904–912.

145. J. Bartels, M. G. Ryskin, and G. P. Vacca, *On the triple pomeron vertex in perturbative QCD*, *Eur. Phys. J.* **C27** (2003) 101–113, [hep-ph/0207173].

146. A. Del Fabbro and D. Treleani, *Double parton scatterings in b-quark pairs production at the LHC*, *Phys. Rev.* **D66** (2002) 074012, [hep-ph/0207311].

147. B. Humpert, *Are there multi - quark interactions?*, *Phys. Lett.* **B131** (1983) 461.

148. B. Humpert and R. Odorico, *Multiparton scattering and QCD radiation as sources of four jet events*, *Phys. Lett.* **B154** (1985) 211.

149. L. Ametller, N. Paver, and D. Treleani, *Possible signature of multiple parton interactions in collider four jet events*, *Phys. Lett.* **B169** (1986) 289.

150. F. Halzen, P. Hoyer, and W. J. Stirling, *Evidence for multiple parton interactions from the observation of multi-muon events in Drell-Yan experiments*, *Phys. Lett.* **B188** (1987) 375–378.

151. M. L. Mangano, *Four Jet Production at the Tevatron Collider*, *Z. Phys.* **C42** (1989) 331.

152. R. M. Godbole, S. Gupta, and J. Lindfors, *Double parton scattering contribution to W + jets*, *Z. Phys.* **C47** (1990) 69–74.

153. M. Drees and T. Han, *Signals for double parton scattering at the Fermilab Tevatron*, *Phys. Rev. Lett.* **77** (1996) 4142–4145, [hep-ph/9605430].

154. M. Y. Hussein, *A double parton scattering background to associate WH and ZH production at the LHC*, *Nucl. Phys. Proc. Suppl.* **174** (2007) 55–58, [hep-ph/0610207].

155. M. Y. Hussein, *Double parton scattering in associate Higgs boson production with bottom quarks at hadron colliders*, arXiv:0710.0203.

156. S. Domdey, H.-J. Pirner, and U. A. Wiedemann, *Testing the Scale Dependence of the Scale Factor in Double Dijet Production at the LHC*, *Eur. Phys. J.* **C65** (2010) 153–162, [arXiv:0906.4335].

157. E. L. Berger, C. B. Jackson, and G. Shaughnessy, *Characteristics and Estimates of Double Parton Scattering at the Large Hadron Collider*, *Phys. Rev.* **D81** (2010) 014014, [arXiv:0911.5348].

158. E. L. Berger, C. Jackson, S. Quackenbush, and G. Shaughnessy, *Calculation of W b bbar Production via Double Parton Scattering at the LHC*, *Phys. Rev. D* **84** (2011) , 074021, [arXiv:1107.3150]. * Temporary entry *.

159. A. Kulesza and W. J. Stirling, *Like sign W boson production at the LHC as a probe of double parton scattering*, *Phys. Lett.* **B475** (2000) 168–175, [hep-ph/9912232].

160. M. S. Chanowitz and W. B. Kilgore, *W+ Z and W+ gamma* backgrounds to strong W+ W+ scattering at the LHC*, *Phys. Lett.* **B347** (1995) 387–393, [hep-ph/9412275].

161. C. Kom, A. Kulesza, and W. Stirling, *Pair production of J/psi as a probe of double parton scattering at LHCb*, *Phys.Rev.Lett.* **107** (2011) 082002, [arXiv:1105.4186].

162. C. Kom, A. Kulesza, and W. Stirling, *Prospects for observation of double parton scattering with four-muon final states at LHCb*, arXiv:1109.0309.

163. J. R. Gaunt, C. Kom, A. Kulesza, and W. Stirling, *Probing double parton scattering with leptonic final states at the LHC*, arXiv:1110.1174.

164. S. Baranov, A. Snigirev, and N. Zotov, *Double heavy meson production through double parton scattering in hadronic collisions*, arXiv:1105.6276.

165. A. Novoselov, *Double parton scattering as a source of quarkonia pairs in LHCb*, arXiv:1106.2184.

166. E. Maina, *Multiple Parton Interactions in Z+jets production at the LHC. A comparison of factorized and non–factorized double parton distribution functions*, arXiv:1010.5674.

167. E. Maina, *Multiple Parton Interactions, top–antitop and W+4j production at the LHC*, *JHEP* **04** (2009) 098, [arXiv:0904.2682].

168. E. Maina, *Multiple Parton Interactions in Z+4j, W± W± +0/2j and W+ W- +2j production at the LHC*, *JHEP* **09** (2009) 081, [arXiv:0909.1586].

169. J. M. Campbell, R. K. Ellis, and G. Zanderighi, *Next-to-leading order predictions for WW + jet distributions at the LHC*, *JHEP* **12** (2007) 056, [arXiv:0710.1832].

170. J. M. Campbell and R. K. Ellis, *Next-to-leading order corrections to W+2 jet and Z+2 jet production at hadron colliders*, *Phys. Rev.* **D65** (2002) 113007, [hep-ph/0202176].

171. J. M. Campbell, R. K. Ellis, and D. L. Rainwater, *Next-to-leading order QCD predictions for W + 2jet and Z + 2jet production at the CERN LHC*, *Phys. Rev.* **D68** (2003) 094021, [hep-ph/0308195].

172. R. K. Ellis, K. Melnikov, and G. Zanderighi, *Generalized unitarity at work: first NLO QCD results for hadronic W+ 3jet production*, *JHEP* **04** (2009) 077, [arXiv:0901.4101].

173. R. K. Ellis, K. Melnikov, and G. Zanderighi, *W+3 jet production at the Tevatron*, *Phys. Rev.* **D80** (2009) 094002, [arXiv:0906.1445].

174. C. F. Berger *et. al.*, *One-Loop Multi-Parton Amplitudes with a Vector Boson for the LHC*, arXiv:0808.0941.

175. C. F. Berger *et. al.*, *Next-to-Leading Order QCD Predictions for W+3-Jet Distributions at Hadron Colliders*, *Phys. Rev.* **D80** (2009) 074036, [arXiv:0907.1984].

176. C. F. Berger *et. al.*, *Next-to-Leading Order QCD Predictions for Z,gamma* +3-Jet Distributions at the Tevatron*, *Phys. Rev.* **D82** (2010) 074002, [arXiv:1004.1659].

177. R. Hamberg, W. L. van Neerven, and T. Matsuura, *A Complete calculation of the order alpha-s**2 correction to the Drell-Yan K factor*, *Nucl. Phys.* **B359** (1991) 343–405.

178. **CDF** Collaboration, T. Aaltonen *et. al.*, *Measurement of the cross section for W-boson production in association with jets in ppbar collisions at s**(1/2) = 1.96-TeV*, *Phys. Rev.* **D77** (2008) 011108, [`arXiv:0711.4044`].

179. **CDF - Run II** Collaboration, T. Aaltonen *et. al.*, *Measurement of inclusive jet cross-sections in Z/gamma** ($\to e^+ e^-$) *+ jets production in $p\bar{p}$ collisions at $\sqrt{s}$ = 1.96-TeV*, *Phys. Rev. Lett.* **100** (2008) 102001, [`arXiv:0711.3717`].

180. A. Ballestrero, A. Belhouari, G. Bevilacqua, V. Kashkan, and E. Maina, *PHANTOM: a Monte Carlo event generator for six parton final states at high energy colliders*, *Comput. Phys. Commun.* **180** (2009) 401–417, [`arXiv:0801.3359`].

181. A. Ballestrero and E. Maina, *A New method for helicity calculations*, *Phys. Lett.* **B350** (1995) 225–233, [`hep-ph/9403244`].

182. A. Ballestrero, *PHACT: Helicity amplitudes for present and future colliders*, `hep-ph/9911318`.

183. F. Maltoni and T. Stelzer, *MadEvent: Automatic event generation with MadGraph*, *JHEP* **02** (2003) 027, [`hep-ph/0208156`].

184. J. Alwall *et. al.*, *MadGraph/MadEvent v4: The New Web Generation*, *JHEP* **09** (2007) 028, [`arXiv:0706.2334`].

185. J. Pumplin, A. Belyaev, J. Huston, D. Stump, and W. K. Tung, *Parton distributions and the strong coupling: CTEQ6AB PDFs*, *JHEP* **02** (2006) 032, [`hep-ph/0512167`].

186. **CMS** Collaboration, G. L. Bayatian *et. al.*, *CMS physics: Technical design report*, . CERN-LHCC-2006-001.

187. **CMS** Collaboration, G. L. Bayatian *et. al.*, *CMS technical design report, volume II: Physics performance*, *J. Phys.* **G34** (2007) 995–1579.

188. **ATLAS** Collaboration, G. Aad *et. al.*, *Expected Performance of the ATLAS Experiment - Detector, Trigger and Physics*, `arXiv:0901.0512`.

189. J. M. Campbell, J. W. Huston, and W. J. Stirling, *Hard Interactions of Quarks and Gluons: A Primer for LHC Physics*, *Rept. Prog. Phys.* **70** (2007) 89, [`hep-ph/0611148`].

190. J. R. Gaunt and W. Stirling, *Double Parton Scattering Singularity in One-Loop Integrals*, *JHEP* **1106** (2011) 048, [`arXiv:1103.1888`].

191. J. R. Gaunt, *Double Parton Splitting Diagrams and Interference and Correlation Effects in Double Parton Scattering*, `arXiv:1110.1536`.